COMPUTATIONAL MODELING OF UNSTEADY AERODYNAMICS IN HUMMINGBIRD FLIGHT

By

Jialei Song

Dissertation

Submitted to the Faculty of the

Graduate School of Vanderbilt University

in partial fulfillment of the requirements

for the degree of

DOCTOR OF PHILOSOPHY

in

Mechanical Engineering

May, 2016

Nashville, Tennessee

Approved:

Haoxiang Luo, Ph.D.

Caglar Oskay, Ph.D.

Robert Pitz, Ph.D.

Deyu Li, Ph.D.

Acknowledgments

Pursuing the doctorate degree is like running a marathon. It is a long and tough journey, and it can't be successfully accomplished without the help and support of many people. Here I sincerely thank all these people.

First, I would like to owe the biggest thank you to my advisor, Dr. Haoxiang Luo, who continuously gave me the insightful advice on the research and warmhearted care on the life during the past five years. His great efforts and tremendous patience helped me become well trained on scientific research methods and work productively. Aside the research, Dr. Luo also offered me plenty of opportunities on the career development and network-building. Overall, I have greatly improved in the last five years under the supervision of Dr. Luo.

Second, I would like to give my great thanks to Dr. Tyson Hedrick at the University of North Carolina at Chapel Hill and Dr. Bret Tobalske at University of Montana. My research is computational modeling of aerodynamics of hummingbird flight, and the accurate description of the bird kinematics is of great importance. Dr. Hedrick kindly provided us the data of the hummingbird hovering flight, and Dr. Tobalske provided us the data of the fast forward flight. In addition, the discussions with them were really a pleasant experience since they offered many insightful suggestions and provided numerous helpful inputs from the biology aspect.

I also want to thank my Ph.D. committee members, Profs. Robert Pitz and Deyu Li in the Department of Mechanical Engineering and Prof. Caglar Oskay in the Department of Civil and Environmental Engineering, for their time and effort of serving on my committee. They gave me not only the advice for the refinement of my research and

dissertation, but also helpful advice on the academic career.

Finally, thanks must be given to my family, friends and lab mates, Dr. Fangbao Tian, Dr. Bo Yin, Dr. Hu Dai, Siyuan Chang, Chi Zhu, Casey Brock, Joshwa Webb, Ye Chen and Yang Zhang for their love, their support and their help. Especially, Dr. Fangbao Tian has selflessly given me advice and support from my undergraduate time to the present.

I appreciate that I have all these people in this long journey and they have made this marathon joyful, meaningful and unforgettable.

CONTENTS

LIST OF TABLES

LIST OF FIGURES

CHAPTER I

INTRODUCTION

1.1 MAVs and aerodynamics of flapping wings

Micro air vehicles (MAVs) are defined by the Defense Advanced Research Projects Agency (DARPA) as robotic flyers that have wingspan under 15 cm and weight less than 20 grams. As compared with larger aerial vehicles, MAVs have advantage of great agility and promise to fly in a complex environment (e.g., indoor settings or cluttered zones). With micro electronic and wireless communication devices on board, MAVs have numerous applications such as military intelligence, surveillance and reconnaissance, searching and rescuing, environment monitoring, and urban policing.

Depending on the mechanism for lift and propulsion, MAVs can be generally divided into three categories: fixed wings, rotary wings, and flapping wings. In contrast with fixed-wing and rotary-wing MAVs, flapping-wing MAVs are inspired by nature and they mimic the flight strategy of animals such as insects, birds, and bats. The wings of these animals serve as both lifting surfaces and thrusters, and they allow the animals to make extremely fast maneuvers (e.g., during chase and escape), fly effortlessly in gusty environment, attack precisely and stealthily, and sustain flight for a long time. Therefore, even though the other types of MAVs (e.g., quad-rotor MAVs) have grown rapidly in recent years, the natural flyers with superior performance will continue to

inspire engineers to seek flapping wings as an alternative strategy for future MAVs.

The most remarkable characteristic of flow around the flapping wing is that the flow is typically separated from the wing surface and is unsteady. These features distinguish aerodynamics of flapping wings from that of traditional wings. In the early twentieth century, it was found that the traditional aerodynamic theory based on the steady, attached flow assumption failed to predict enough lift production of insect wings (Weis-Fogh and Jensen, 1956). This dilemma has led to later discovery of unsteady mechanisms associated with flapping wings. In particular, a leading-edge vortex (LEV) is generated during a wing transition and stably attaches to the wing surface during most of wingbeat (Ellington et al., 1996). This stable LEV leads to low pressure on the wing upper surface and thus overall augments lift. Besides, there are many other issues involving in flapping-wing aerodynamics. For example, when a wing flaps back and forth, it also rotates around its own longitudinal axis, a motion called pitching. Such pitching motion dynamically changes the angle of attack and introduces a nonlinear rotational effect that is analogous to the Magus effect (Dickinson et al., 1999; Sane, 2003). Another effect is wing-wake interaction, which takes place when the wing reverses its translational direction. The wing encounters the wake induced by the proceeding half stroke thus increases the relative velocity of the wing with respect to the flow (Dickinson et al., 1999). Clap and cling is another effect for small insects such as greenhouse whitefly. That is, in a nearly horizontal stroke plane, the two wings close up at the end of upstroke to push air downward; then the wings start to separate from the leading edge, creating a low pressure zone between the two wings and thus generating additional lift (Weis-

Fogh, 1973; Spedding and Maxworthy, 1986; Ellington, 1984). Structural mechanics is also heavily involved in the aerodynamics of flapping wings as the wings are typically passively flexible and have time-dependent deformations during wingbeat (Dai et al., 2012b). This aeroelasticity necessarily requires a fluid-structure interaction approach to study the effect of the wing flexibility.

There has been significant progress made in recent years in terms of understanding aerodynamics of flapping wings. Both experimental and computational approaches have been used to study this problem. On the experimental side, both force measurement and flow visualization, e.g., bubble/smoke visualization and also particle imaging velocimetry (PIV), have been applied to study the flow pattern (Ellington et al., 1996; Lentink and Dickinson, 2009; Elimelech and Ellington, 2013). Direct force measurement has mainly been utilized for the model wings or the exercised wings flapped by robotic apparatuses. Both idealized wing kinematics (Fry et al., 2003; Birch and Dickinson, 2001; Lentink and Dickinson, 2009; Kruyt et al., 2014) and more realistic kinematics (Dickinson et al., 1999) have been adopted for those model wings to study effect of the different kinematic aspects. In particular, Dickinson et al. (1999) designed an apparatus to flap a model fly wing with three degrees of freedom, and with approximated wing kinematics, they measured the time-dependent lift and drag forces of the wing. In terms of flow measurement, only limited information can be obtained from flow visualization, and there is not much detail about the three-dimensional flow field. For live animals, PIV measurements have been done in some cases to measure the fluid velocity (Warrick et al., 2009, 2005; Wolf et al., 2013a; Kim et al., 2014; Rosén et al.,

2007; Henningsson et al., 2008; Spedding et al., 2003).

Computational fluid dynamics offers a great alternative approach to understand the complex flow physics of the flapping-wing problem. Two-dimensional, and more recently, three-dimensional, models have been developed to simulate the unsteady flow, mostly for hovering flight (Sun and Tang, 2002a; Wang et al., 2004a; Aono et al., 2008; Dai et al., 2012a; Jardin et al., 2012; Harbig et al., 2013). In most of these work, the wing motions are idealized (e.g., using sinusoidal functions), so that the studies could focus on some fundamental flow physics. In some other cases (Young et al., 2009; Zheng et al., 2013a), real animals (e.g., locusts and hawk moths) were simulated and information about the flow and forces can be obtain directly. In contrast with idealized wing models that are devoted to understanding of isolated fundamental flow physics, more realistic three-dimensional models like those for real animals allow us to study the animal flight directly. For example, we can get the overall lift and thrust production of the entire wing and also detailed data on pressure distribution. In addition, the three-dimensional flow can be visualized, and the whole field data could be used for detailed analysis.

1.2 Aerodynamics of hummingbird flight

Hummingbirds are distinguished and extremely agile flyers among birds. They are capable of not only sustained hovering flight but also fast forward flight and various rapid maneuvers. Their superb performance has inspired development of miniaturized aerial vehicles, e.g., the robot dubbed “Nano Hummingbird” that was recently invented

by AeroVironment Co., (Monrovia, CA) (Keennon et al., 2010).

As the only bird that is capable of performing sustained hovering flight (Kruyt et al., 2014), hummingbirds' the morphological kinematics, aerodynamics and power consumption at hovering flight have been extensively studied (Hedrick et al., 2012; Tobalske et al., 2007; Warrick et al., 2005, 2009; Chai and Dudley, 1999; Altshuler et al., 2004a). Tobalske et al. (2007) performed comprehensive measurement of the flight kinematics of the rufous hummingbirds in the wind tunnel at speed from zero (hovering) to 12 m/s. The data they obtained include the body orientation angle, wingbeat frequency, wingbeat amplitude, stroke plane angle, wingtip trajectory, and time-dependent variables such as the wing chord angle and wing area, at different flight speeds. Hedrick et al. (2012) used high-speed three-dimensional X-ray videography and found hummingbirds enable the high-degree supination by allowing rotation at the wrist and possibly even at other skeletal elements on the wings, which provide the morphological knowledge to explain why the hummingbird can reverse the wing during stroke transition.

Altshuler et al. (2004a) used a dissected hummingbird wing and tested lift production of the wing revolving in one direction. By comparing with wing models of increasing realism, i.e., those with sharpened leading edges and with substantial camber, they found that the real hummingbird wing generates more lift, and their result suggests that some geometric details such as the presence of camber tend to increase lift. Using particle image velocimetry (PIV), Warrick et al. (2005, 2009) studied the flight of rufous hummingbirds. They were able to measure the flow in the two-dimensional planes that

are perpendicular to the wing axis during the entire stroke cycle. Based on the PIV data, they visualized the leading-edge vortex (LEV) and calculated the circulation at different spanwise locations. Interestingly, their result shows that the average bound circulation during the downstroke is 2.1 times of the that during the upstroke (Warrick et al., 2009). Assuming that the conventional airfoil theory holds, that is, lift is linearly proportional to the bound circulation, the authors suggest that the lift production possesses the same amount of asymmetry. They further proposed the possible mechanisms that may have contributed to such lift characteristics. For example, the wing velocity and the angle of attack during the downstroke are greater than those during the upstroke. Other variables they suggested include longer wing span and formation of a positive camber during the downstroke.

In another PIV study, Altshuler et al. (2009) measured the wake flow of the wings and tail of hovering Anna's hummingbirds, and they proposed a vortex-ring model for the wake generated by the wings. Later, Wolf et al. (2013a) conducted further PIV study of the same hummingbird species, and from the strength of the shed vortices, they also concluded that lift production is highly asymmetric between the two half strokes. Most recently, Kruyt et al. (2014) compared the quasi-steady hover performance of 26 wings from 12 hummingbird taxa, the aspect ratio (AR) of which ranges from about 3.0 to 4.5. Their comparative analysis shows that AR has a modest influence on the lift and drag force, but interspecific differences in power factor are large. During the downstroke,the power required to hover decreases for large AR wings at the angles of attack at which hummingbird flap their wings. The aerodynamic performance comparison of hum-

mingbird wings and an advanced micro helicopter rotor shows that they are remarkably close.

Despite these previous efforts, there exists no direct study on the detailed force characteristics and the three-dimensional flow pattern of the hummingbird wing in hovering flight, and even less study on the aerodynamics of forward flight and other maneuvers.

1.3 The specific objectives of this study

As an efficient and economical way to study such the fluid dynamics phenomena, Computational Fluid Dynamics (CFD) has been applied in many previous works to study aerodynamics of flapping wings, including both rigid and flexible wing models (Liu and Kawachi, 1998; Sun and Tang, 2002b; Young et al., 2009; Shyy et al., 2010). Since our lab at Vanderbilt university has the specialty of performing accurate CFD studies of problems involving complex and moving boundaries such as flapping wings, here we are motivated to investigate the force production mechanisms utilized by hummingbirds during different flight modes. Our specific objectives include:

1) Simulate the three-dimensional flow of hovering hummingbirds and study the characteristics of lift, drag, and power within wingbeat cycles; study the relationship among the wing kinematics, forces, and flow.

2) Develop a reduced-order model of the wing aerodynamics to quickly calculate force production of the hummingbird wings; assess accuracy of this model using results from the full CFD model.

3) Develop a biomechanic model for rotational dynamics of the hummingbird wings by including both inertial and aerodynamics effects; determine active and passive mechanism responsible for wing pitching.

4) Simulate the three-dimensional cruise flight at fast speeds and study the mechanisms that hummingbirds utilize to generate sufficient lift and thrust.

CHAPTER II

NUMERICAL APPROACH AND MODEL RECONSTRUCTION

2.1 Numerical approach

In the present study, the airflow around the hummingbird is governed by the viscous incompressible Navier-Stokes equation since the Mach number of hummingbird flight (wing speed around 10 m/s) is less than 0.03. The buoyancy is also ignored. Thus, the momentum equation and the continuity equation are written as

$$\begin{aligned} \frac{\partial u_i}{\partial t} + \frac{\partial u_j u_i}{\partial x_j} &= -\frac{1}{\rho}\frac{\partial p}{\partial x_i} + \nu \frac{\partial^2 u_i}{\partial x_j^2}, \\ \frac{\partial u_i}{\partial x_i} &= 0, \end{aligned} \tag{2.1}$$

where u_i is the velocity, ρ and ν are the constant density and viscosity, and p is the pressure.

The following description is a summary of the numerical method described in detail in Luo et al. (2012) and Yin and Luo (2010). The governing equations are discretized on a nonuniform Cartesian grid using a cell-centered, non-staggering arrangement of the primitive variables, u_i and p. The incompressible momentum equation is integrated in time using a variation of Chorin's projection method which consists of three sub-steps (Chorin, 1968). In the first sub-step, an advection–diffusion equation is solved in the absence of the pressure, and an intermediate velocity field, u_i^*, is obtained. In this

step, both the nonlinear advection terms and the viscous terms are discretized using the Crank–Nicolson scheme to improve the numerical stability. The discrete equation is written as

$$\frac{u_i^* - u_i^n}{\Delta t} + \frac{1}{2}\left[\frac{\delta(U_j u_i)^*}{\delta x_j} + \frac{\delta(U_j u_i)^n}{\delta x_j}\right] = \frac{\nu}{2}\left[\frac{\delta}{\delta x_j}\left(\frac{\delta u_i^*}{\delta x_j}\right) + \frac{\delta}{\delta x_j}\left(\frac{\delta u_i^n}{\delta x_j}\right)\right], \tag{2.2}$$

where U_j is the velocity discretized at the face center of a computational cell, and $\frac{\delta}{\delta x_j}$ represents a finite-difference approximation of the spatial derivative using a second-order central scheme. The nonlinear algebraic system is solved by a successive substitution approach.

In the second sub-step, a projection function is solved as an approximation of the pressure,

$$\frac{\delta}{\delta x_j}\left(\frac{\delta p^{n+1}}{\delta x_j}\right) = \frac{\rho}{\Delta t}\frac{\delta U_j^*}{\delta x_j}, \tag{2.3}$$

and an inhomogeneous Neumann boundary condition is imposed at all boundaries. The Poisson equation (2.3) is solved with an efficient geometric multigrid method, as discussed in Mittal et al. (2008). Once the pressure is obtained, the cell-centered velocity is updated as

$$u_i^{n+1} = u_i^* - \frac{\Delta t}{\rho}\frac{\delta p^{n+1}}{\delta x_i}, \tag{2.4}$$

and the final face-centered velocity, U_i^{n+1}, is updated by averaging u_i^{n+1} along the i-direction.

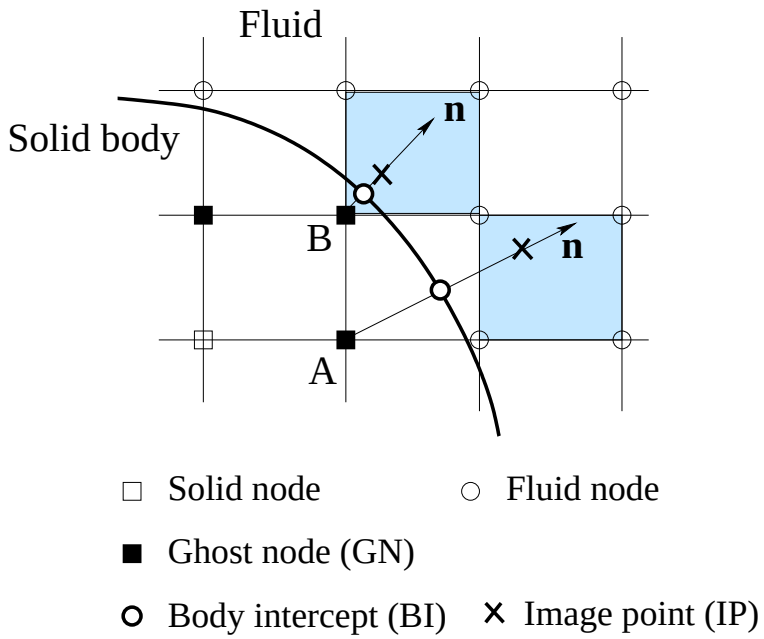

Figure 2.1: A 2D illustration of the sharp-interface immersed-boundary method for the fluid–solid boundary. Flow field extrapolation is applied at the ghost nodes.

In this work, a previously developed second-order sharp-interface immersed-boundary method (Mittal et al., 2008; Luo et al., 2012) is used to handle the complex geometry of the fluid–solid interface. In this method, the irregular solid interface is triangulated by an unstructured surface mesh consisting of a set of Lagrangian marker points. The nodal points on the Cartesian grid that discretizes the computational domain are labeled either as “solid nodes” or “fluid nodes” depending on which side of the interface the node is located on. Away from the solid surface, the Navier–Stokes equation is discretized using a standard second-order central difference scheme. Such a scheme is also applied at the fluid–fluid interface after the diffuse-interface treatment, as will be discussed in next section.

Near the solid surface, the standard central difference scheme cannot be applied for those nodes at which the stencil involves solid nodes. These fluid nodes are immediately

next to the solid surface and are termed “hybrid” nodes, and the corresponding solid nodes involved in the stencil are termed “ghost” nodes (GN). We emphasize that as shown by Luo et al. (2012), the special treatments at these nodes do not compromise the overall second-order accuracy of the method.

Flow field reconstruction is applied at the ghost nodes with the boundary condition incorporated Mittal et al. (2008). To accomplish this, the image point (IP) on the fluid side is found by projecting the ghost node along the surface normal, and the body intercept (BI) on the solid surface is thus located midway between the ghost node and image point. Assume that $\phi(x_1, x_2, x_3)$ is a generic variable. To interpolate the value of ϕ at the image point, a trilinear interpolation is used in the local area with eight nodes enclosing the image point,

$$\phi(x_1, x_2, x_3) = C_1 x_1 x_2 x_3 + C_2 x_1 x_2 + C_3 x_2 x_3 + C_4 x_3 x_1 + C_5 x_1 + C_6 x_2 + C_7 x_3 + C_8, \quad (2.5)$$

where the polynomial coefficients $C_i, i = 1, 2, ..., 8$, are determined by the values of ϕ at the eight nodes, ϕ_i,

$$\{C\} = [V]^{-1}\{\phi\}. \quad (2.6)$$

with $\{C\}^T = \{C_1, C_2, ..., C_8\}$ and $\{\phi\}^T = \{\phi_1, \phi_2, ..., \phi_8\}$. The matrix $[V]$ is the Vander-

monde matrix constructed from the coordinates of the eight nodes,

$$[V] = \begin{bmatrix} x_1x_2x_3|_1 & x_1x_2|_1 & x_2x_3|_1 & x_3x_1|_1 & x_1|_1 & x_2|_1 & x_3|_1 & 1 \\ x_1x_2x_3|_2 & x_1x_2|_2 & x_2x_3|_2 & x_3x_1|_2 & x_1|_2 & x_2|_2 & x_3|_2 & 1 \\ \vdots & \vdots & \vdots & & & & & \vdots \\ x_1x_2x_3|_8 & x_1x_2|_8 & x_2x_3|_8 & x_3x_1|_8 & x_1|_8 & x_2|_8 & x_3|_8 & 1 \end{bmatrix} \tag{2.7}$$

where the subscript in $(\cdot)|_i$ means the ith node. With the solved coefficients, the interpolated value at the image point becomes

$$\phi_{\text{IP}}(x_1, x_2, x_3) = \{X\}^T\{C\} = \{X\}^T[V]^{-1}\{\phi\} = \sum_{i=1}^{8} \beta_i\phi_i \tag{2.8}$$

where $\{X\}^T = \{x_1x_2x_3, x_1x_2, x_2x_3, x_3x_1, x_1, x_2, x_3, 1\}|_{IP}$ denotes the vector based on the coordinates of the image point and β_i is the interpolation weight calculated from $\{X\}^T[V]^{-1}$. From Eq. (2.8), the interpolation weight β_i depends on the position of the image point and the eight data points only. Thus, it can be determined once the geometrical information is available and is then ready for use during the iterative solution of the flow variables.

The eight data points used for interpolation could be the eight vertices on the computational cell surrounding the image point. However, the ghost node itself could be one of the eight nodes, as shown by one of the two situations depicted in Fig. 2.1. Under such circumstance, the ghost node is replaced by the body intercept in the interpolation process. At the body intercept, either Dirichlet (for the velocity) or Neumann (for the pressure) condition is specified. For the Dirichlet condition, using the body intercept in

the interpolation is straightforward: the interpolation formula in Eq. (2.8) remains the same and the variables in $\{\phi\}$ and $[V]$ should be replaced by those at the body intercept. For the Neumann condition, $\partial\phi/\partial n$, needs to be incorporated into the interpolation formula. This is done by modifying the last row of the Vandermonde matrix in Eq. (2.7) into

$$\begin{bmatrix} n_1x_2x_3 + n_2x_1x_3 + n_3x_1x_2 & n_1x_2 + n_2x_1 & n_2x_3 + n_3x_2 & n_1x_3 + n_3x_1 & n_1 & n_2 & n_3 & 0 \end{bmatrix} \quad (2.9)$$

where (n_1, n_2, n_3) represents the surface normal at the body intercept. Correspondingly, the last element in ϕ is replaced by $\partial\phi/\partial n$ at the body intercept, and Eq. (2.8) becomes

$$\phi_{\mathrm{IP}}(x_1, x_2, x_3) = \sum_{i=1}^{7} \beta_i\phi_i + \beta_8\frac{\partial\phi}{\partial n}. \quad (2.10)$$

For the velocity boundary condition, a linear distribution is simply assumed along the line segment connecting the ghost node, body intercept, and the image point. That is,

$$\mathbf{u}_{GN} + \mathbf{u}_{IP} = 2\mathbf{u}_{BI}. \quad (2.11)$$

Given the boundary velocity, $\mathbf{u}_{BI}$, where $\mathbf{u}_{BI} = 0$ for a stationary boundary, $\mathbf{u}_{GN}$ can be calculated from Eq. (2.11). For the pressure, $\frac{\partial p}{\partial n}$ is given as the boundary condition. Using a central difference approximation, the condition can be written as

$$\left.\frac{\partial p}{\partial n}\right|_{BI} = \frac{p_{IP} - p_{GN}}{\Delta l} = -\rho\frac{\mathrm{D}u}{\mathrm{D}t}\cdot\mathbf{n}\Big|_{BI} \quad (2.12)$$

where the Δl is the distance between the IP and GN. Inhomogeneous pressure condition $\partial p/\partial \mathbf{n} = -\rho(\mathrm{D}\mathbf{u}/\mathrm{D}t) \cdot \mathbf{n}$ has been assumed here. The value of $\mathrm{D}\mathbf{u}/\mathrm{D}t$ at the body intercept is interpolated from the acceleration of the Lagrangian marker points on the solid surface in the case of a moving boundary.

With the above numerical descriptions of the flow variables at the ghost nodes and the finite-difference discretization at all the fluid nodes, a complete algebraic system could be formed for all the discrete variables. More details of implementation and validation of this sharp-interface treatment are provided in Mittal et al. (2008). In case that the solid surface is a moving boundary, such method may be subject to numerical oscillations as the solid surface moves across the stationary grid and the ghost nodes have to be re-identified at each time step. To suppress the oscillation, Luo et al. (2012) improved the method by applying a hybrid numerical description at the fluid nodes immediately next to the solid surface. In the hybrid description, a local interpolation and the standard finite-difference discretization are weighted based on the distance of the fluid node to the solid surface. Thus, as the boundary moves, the interpolation and finite-difference formulas transition to one another gradually rather than abruptly. Since the primary focus of the current work is on stationary solid boundaries, further details of the moving-boundary treatment is not discussed here. Readers are referred to Luo et al. (2012) for more information.

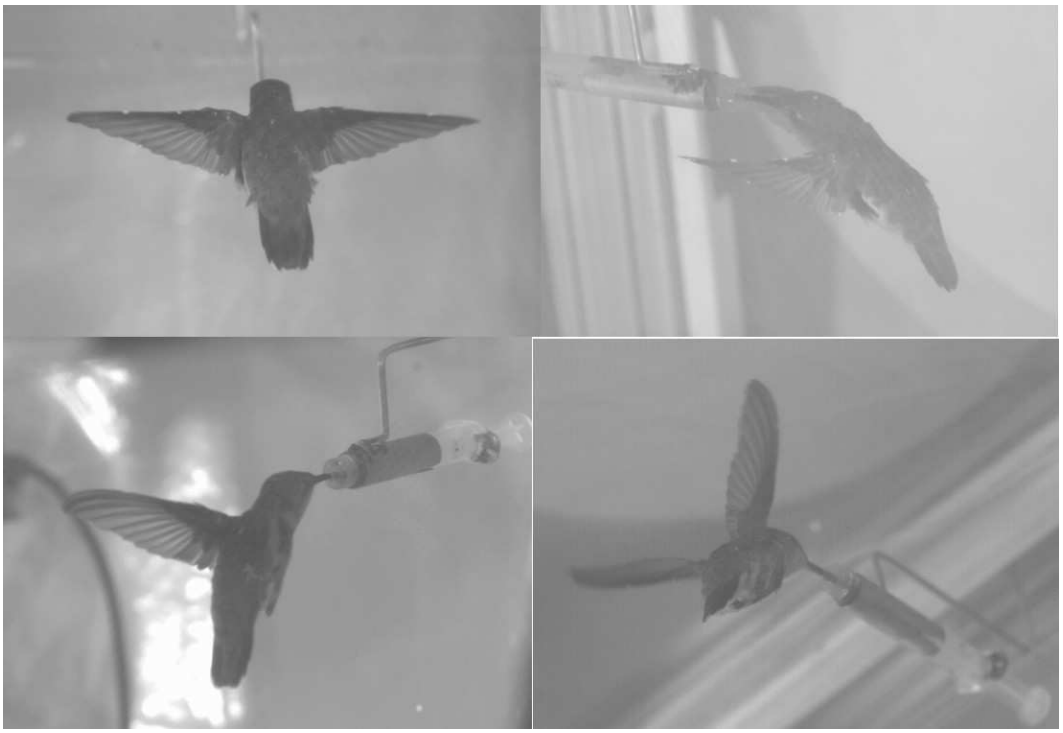

Figure 2.2: Four camera views of a hummingbird hovering in a transparent chamber.

2.2 Model Reconstruction

In the experiment study that was carried out by our collaborators either at the University of North Carolina at Chapel Hill or at the University of Montana, the hummingbirds were trained to fly in the lab. The bird wings were labeled with dots prior to the experiment using white paint. Several synchronized high-speed cameras were positioned to record the bird flight from different view angles to obtain the 3D information and to avoid temporary blockage of the target, as seen in Fig. 2.2.

A custom MATLAB program developed by our collaborators at the University of North Carolina at Chapel Hill was used to digitize the points labeled on the wings frame by frame. In the software, the synchronized videos are loaded at the same time, and a

point of interest is selected in any of the videos which best shows this point. Once the point is selected (simply by a mouse click) in one window, a line in the 3D space that is perpendicular to this view plane is generated and is shown as a blue line in the other view windows (see Fig. 2.3(a)). This reference line guides the point selection. A second mouse click on the line in any of the other views would determine the point, and the numeric values of the 3D coordinates are automatically obtained by the program. Each view window can be independently zoomed to facilitate the process. Even though the program allows automatic tracing of the point from the frame to frame, sometimes we need to manually locate the point for better accuracy.

(a)

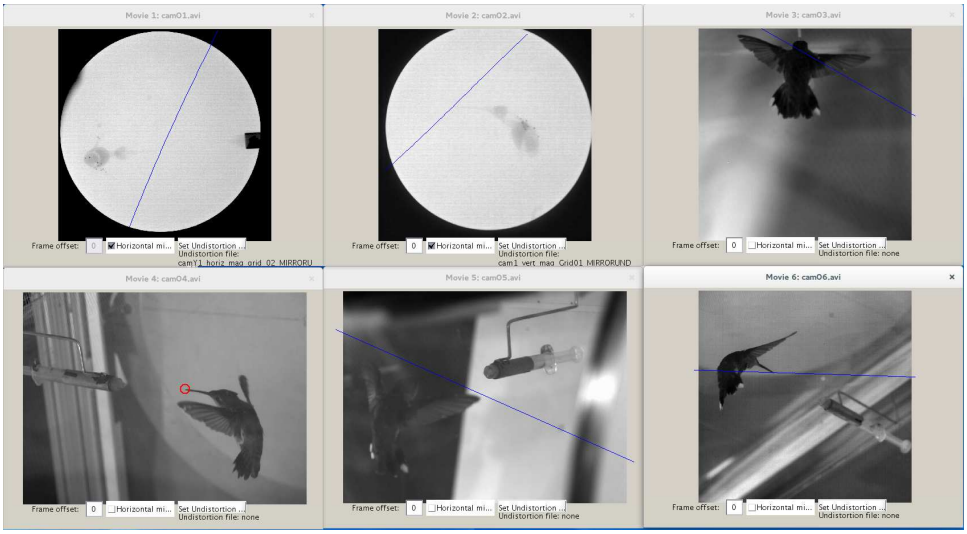

(b)

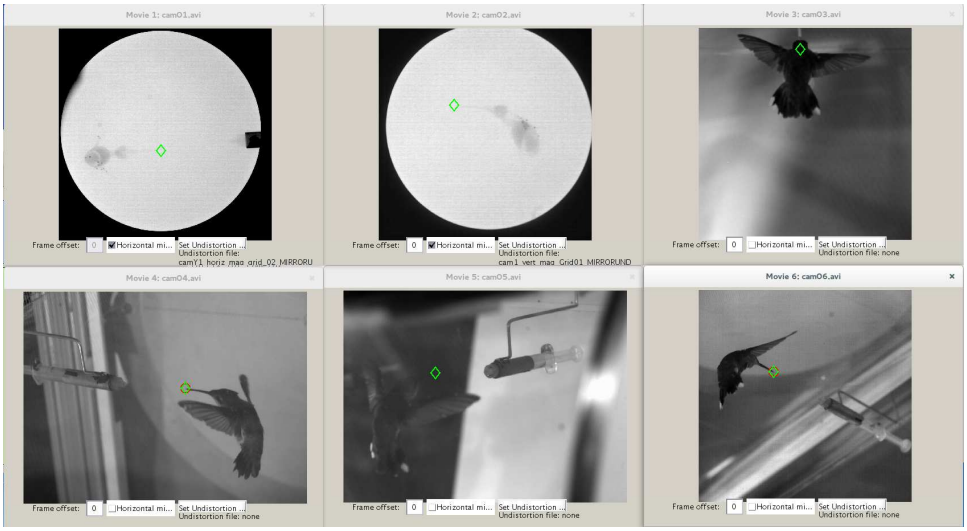

Figure 2.3: Data collection from high-speed videos. (a) The first mouse click in one view generates a line in the 3D space shown in the other views. (b) A second click in another view determines the 3D coordinates of the point. Note that in this figure, two simultaeous X-ray views are also included, which show the musculoskeletal structure of the bird (Hedrick et al., 2012) .

CHAPTER III

THREE-DIMENSIONAL FLOW AND LIFT CHARACTERISTICS OF A HOVERING RUBY-THROATED HUMMINGBIRD

3.1 Introduction

Unlike birds of larger size, hummingbirds can perform sustained hovering in addition to regular cruise flight and maneuvers. Many studies have been done to characterize the kinematics, physiology, and aerodynamics of the hummingbird wing (Weis-Fogh, 1972; Chai and Dudley, 1999; Altshuler et al., 2004a; Warrick et al., 2005), and they were summarized in the work of Tobalske et al. (2007). In general, hummingbirds utilize similar aerodynamics to those of insects, e.g., presence of a leading-edge vortex over the wing surface (Ellington et al., 1996; Sane, 2003), for lift production. However, differences between hummingbird and insect aerodynamics are conceivable since the anatomy and physiology of the hummingbird wing are distinct from those of the insect wing. For example, recent evidence shows that hummingbirds can achieve the inversion of the angle of attack through active wing rotation at the wrist (Hedrick et al., 2012). This actuation mechanism is different from that of insects whose wing inversion can be realized through combined muscle activation at the wing root and the passive deformation of the wing surface (Ennos, 1988a). The implication of this difference on the lift and power efficiency of hummingbirds is still unclear. In order to better understand aerodynamics of hummingbirds, their lift and flow characteristics are needed. Unfor-

tunately, such data are so far very limited. To set the context for the current work, we briefly summarize several recent studies on the force production and flow behavior in the hummingbird flight.

Altshuler et al. (2004a) used a dissected hummingbird wing and tested lift production of the wing revolving in one direction. By comparing with wing models of increasing realism, i.e., those with sharpened leading edges and with substantial camber, they found that the real hummingbird wing generates more lift, and their result suggests that some geometric details such as the presence of camber tend to increase lift. Using particle image velocimetry (PIV), Warrick *et al.* (Warrick et al., 2005, 2009) studied the flight of rufous hummingbirds. They were able to measure the flow in the two-dimensional planes that are perpendicular to the wing axis during the entire stroke cycle. Based on the PIV data, they visualized the leading-edge vortex (LEV) and calculated the circulation at different spanwise locations. Interestingly, their result shows that the average bound circulation during the downstroke is 2.1 times of the that during the upstroke (Warrick et al., 2009). Assuming that the conventional airfoil theory holds, that is, lift is linearly proportional to the bound circulation, the authors suggest that the lift production possesses the same amount of asymmetry. They further proposed the possible mechanisms that may have contributed to such lift characteristics. For example, the wing velocity and the angle of attack during the downstroke are greater than those during the upstroke. Other variables they suggested include longer wing span and formation of a positive camber during the downstroke. In another PIV study, Altshuler et al. (2009) measured the wake flow of the wings and tail of hovering Anna's

hummingbirds, and they proposed a vortex-ring model for the wake generated by the wings. Later, Wolf et al. (2013a) conducted further PIV study of the same hummingbird species, and from the strength of the shed vortices, they also concluded that lift production is highly asymmetric between the two half strokes.

Despite these previous efforts, there exists no direct study on the detailed force characteristics and the three-dimensional flow pattern of the hummingbird wing in hovering flight. As a useful tool, CFD has been applied in many previous works to study aerodynamics of flapping wings, including both rigid and flexible wing models (Liu and Kawachi, 1998; Sun and Tang, 2002b; Young et al., 2009; Shyy et al., 2010). Here we are motivated to perform a CFD study to quantify the force histories in a stroke cycle and to investigate any particular force production mechanisms utilized by the hummingbird. The main questions we would like to answer through the current work include: 1) What are the characteristics of the force history, and what are the underlying mechanisms for the possible downstroke-upstroke asymmetry? 2) What is the three-dimensional wake pattern like, and how may it be associated with the force characteristics? 3) How much aerodynamic power does the hummingbird have to spend on hovering and what is the efficiency? 4) Does the hummingbird utilize some the mechanisms that insects use for lift enhancement, such as wake capture and wing-wing interaction?

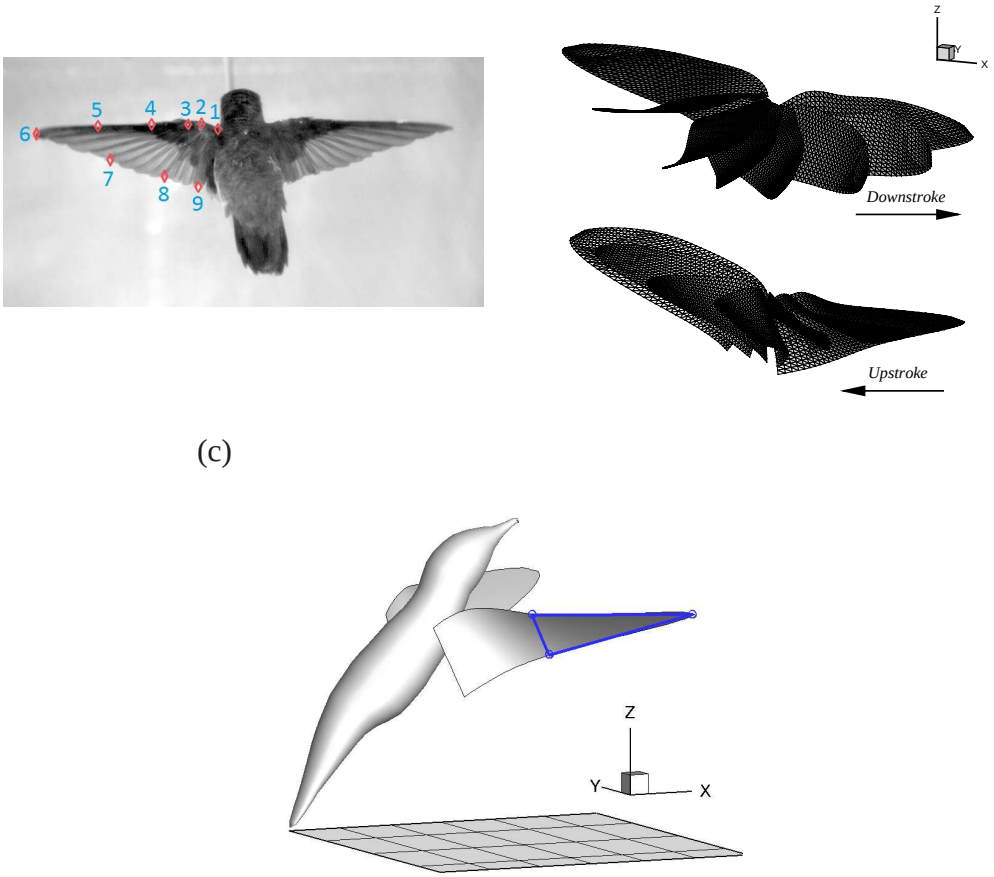

Figure 3.1: (a) Marker points on the outline of the wing. (b) Reconstructed wing kinematics (shown for the right wing). (c) The triangle represents the distal half of the wing surface, based on which the chord angle, α_c, and the angle of attack, α, are defined in the text.

3.2 Method

3.2.1 Experiment and reconstruction of the wing kinematics

The hummingbird, a female ruby-throated (*Archilochus colubris*) with a body mass of 3.41 grams, is used as the subject in the current study. High-speed filming experiment was conducted to record the wing motion of the bird. In the experiment, the bird was trained to fly in a 0.4×0.4×0.5 m^3 netted chamber and was recorded 1000 frames per

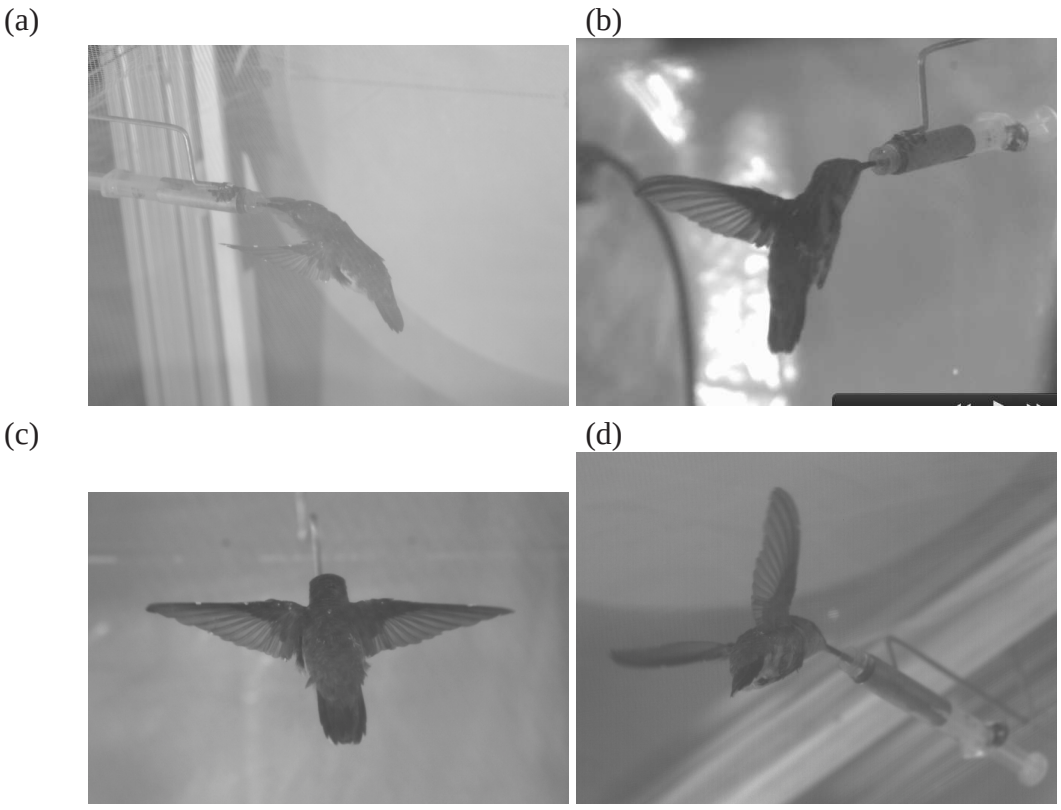

Figure 3.2: Four camera views of the bird. A syringe of nectar is served for the hummingbird hovering.

second with a 1/5000th shutter by four high-speed cameras: two Phantom v7.1 (Vision Research Inc., Wayne, NJ, USA), one Photron SA-3 and one Photron 1024 PCI (Photron USA Inc., San Diego, CA, USA). Each flapping cycle contains about 25 frames. The bird was labeled prior to the experiment using 1-mm diameter dots of non-toxic white paint, as shown in Fig. 3.1(a). The experimental setup is described in detail in Hedrick et al. (2012). The nine markers numbered in Fig. 3.1(a) and located on the outline of the left wing are used in the current study. These markers include five points on the leading edge, one at the wingtip, and three on the trailing edge. To avoid blind spots, the cameras were positioned with one directly behind the bird in the same horizontal plane, two with an elevated oblique and slightly rear view, and one with a ventral view of the

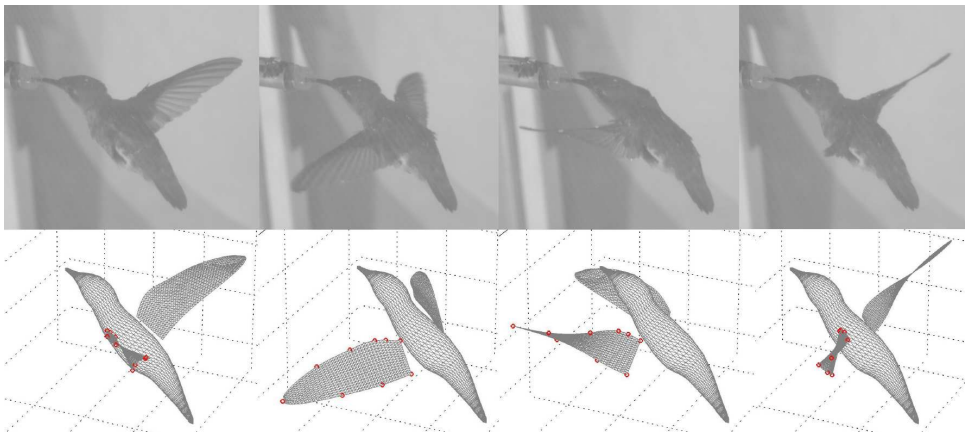

Figure 3.3: Comparison of the reconstructed wing and the video image during early downstroke, around mid-downstroke, early upstroke, and around mid-upstroke

bird (see Fig. 3.2). After the videos are taken, a custom MATLAB program (Hedrick, 2008) was used to automatically track the markers frame by frame and to extract their 3D coordinates. A principal components analysis (PCA) has been done to verify that these nine points are sufficient to characterize the wing motion.

To reconstruct the wing geometry and motion, spline interpolation is used to connect the outline of the wing at each instantaneous time frame. Then, both the leading edge and the trailing edge are evenly discretized by 41 nodes each. The wing chord is approximated with straight segments which have rounded ends and an effective thickness 7% of the average chord length.

A triangular mesh is then generated to discretize the wing surface, which is assumed to be smooth. The comparison with reconstructed wing position with the video images are shown in Fig. 3.3.Corrugations caused by the feathers are ignored since their effect on the laminar boundary layer is expected to be small at the current Reynolds number. Discussions on the effect of feathers at higher Reynolds numbers can be found in

a recent experimental study (Elimelech and Ellington, 2013). A single wing consists of 1129 elements and 615 Lagrangian nodes. To increase the time resolution for the small-step solution of the simulation, the trajectory of each mesh node is also refined by spline interpolation in time. Eight cycles of wing kinematics are reconstructed from the imaging data and are used for the simulation. Note that dynamic deformations of the wing such as spanwise bending and twisting have been included in the reconstructed kinematics (see Fig. S2 in supplementary materials) and thus their aerodynamic consequences will be incorporated in the simulation results.

As seen in Fig. 3.1(b), the entire wing surface exhibits a twist along the wing axis, and the twist angle changes dynamically in a stroke cycle due to the pitching motion of the wing. To define the wing posture and the time-varying angle of attack, we select three points on the wing: the wing tip, the leading edge point and the trailing edge point of the mid-chord. These three points form a triangle approximating posturing of the distal half of the wing surface, as indicated in Fig. 3.1(c). The chord angle, α_c, is defined as the instantaneous acute angle between the plane spanned by this triangle and the horizontal plane. This angle will be used to measure orientation and pitch rotation of the distal wing surface. The angle of attack, α, is defined as the instantaneous angle between the tip velocity vector and the triangle.

3.2.2 Simulation setup and model validation

The numerical method to solve the Navier-stokes equation has been discussed in Chapter II. For the simulation setup, a fixed, nonuniform, single-block Cartesian grid is

	Present	Tobalske et al. (2007)
Body mass, M (g)	3.41	3.4 ± 0.1
Flapping frequency, f (Hz)	42	43 ± 2
Wing length, R (mm)	44.7	47 ± 1
Wing span, b (mm)	110.8	109 ± 2
Average wing chord, c (mm)	11.7	12 ± 1
Single wing area, S (mm^2)	568	558 ± 18
Stroke plane angle (average)	12°	$15^\circ \pm 4^\circ$
Wingbeat amplitude, Φ	114.3°	$111^\circ \pm 2^\circ$

Table 3.1: Comparison between the ruby-throated hummingbird model and the experimental data for the rufous hummingbird.

employed to discretize the domain. The rectangular domain is $20 \times 20 \times 18$ cm^3 (see Fig. 6.7(a)). For the single-wing simulation, 330×250×210 (17 million) points are used for the baseline simulation. A coarser mesh with 232×180×140 (6 million) points and a finer mesh with 420×310×240 (31 million) points are also used in the single-wing case to verify grid convergence. All three meshes have maximum resolution around the wing, which is 0.05 cm, 0.033 cm, and 0.025 cm in all three directions, for the coarser, baseline, and finer mesh, respectively. The two extra simulations are run for two cycles, and they produce a maximum 3% difference from the baseline mesh in the mean and root-mean-square values of the vertical force. The full-body simulation employs 336×408×216 (30 million) points, and the resolution around the body and wings is the same as in the baseline case for the single wing.

The numerical method has been previously validated for flapping-wing simulations against both experimental and simulation data in Dai et al. (2012a), where a fruit-fly model and an impulsively started plate were studied. To further validate the model in the present work, we compare the flow field with that obtained from the PIV experiment by Warrick et al. (2009). Note that the rufous hummingbird (*Selasphorus rufus*) was

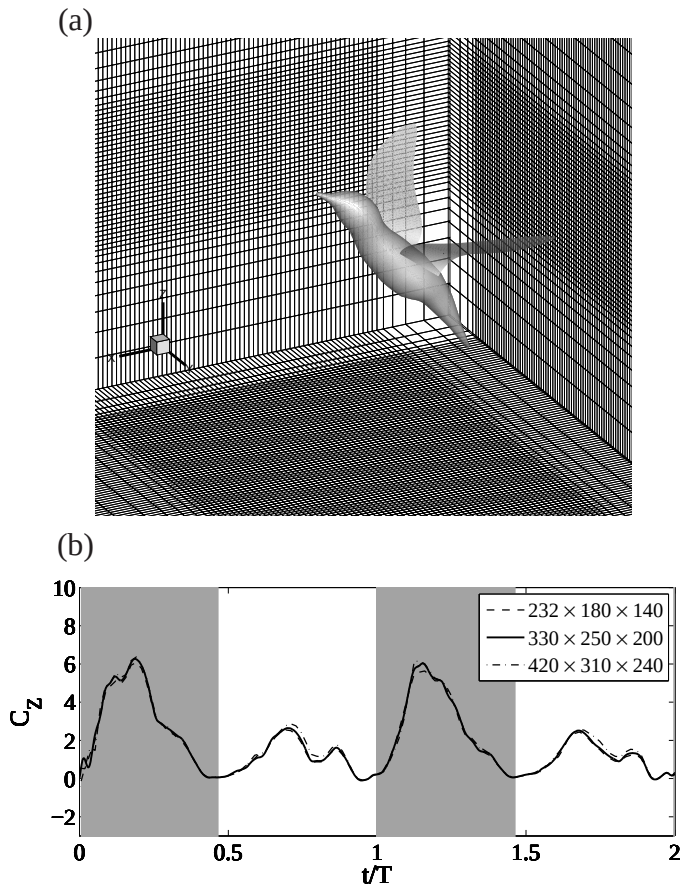

Figure 3.4: The baseline mesh around the bird (only one out of every 4 points in each direction is shown). (b) Grid convergence study where the normalized vertical force of a single wing, C_Z, is plotted.

used in the experiment, while the ruby-throated hummingbird (*Archilochus colubris*) is used in the current study. However, these two species are very similar to each other in terms of the morphological data and wing kinematics. Table 3.1 lists some of the key parameters of the current hummingbird along with those from Warrick et al. (2009), including the body mass, M, the flapping frequency, f, the wing length, R, the wing span, b, average chord length, c, the wing area, S, and the wingbeat amplitude, Φ. It can be seen that all the parameters in the current study fall well within the ranges in the experiment. We also converted the angle of attack and the chord angle of the

present hummingbird using the definitions in the experimental study, and the result of comparison is generally consistent Tobalske et al. (2007), the chord angle is 14° ± 7° for downstroke and 31° ± 4° for upstroke; in Warrick et al. (2005), the angle of attack is 36° ± 12° and 26° ± 13°. In the present study, the chord angle is 16° for downstroke and 48° for upstroke; and the angle of attack is 33° and 24°. All angles are measured according to their definitions). The Reynolds number of the flow is set to be $Re = \frac{2f R\Phi c}{\nu} = 3000$. This nondimensional number represents the ratio between the fluid inertia and the viscous effect.

Fig. 3.5(b) shows a typical spanwise slice of the instantaneous flow during mid-downstroke at 70% wingspan from the wing root. Note that the experimental data is shown for the slice at approximately 80% wingspan, or 4 cm from the wing root. A discussion on the choice of the spanwise location is deferred to the end of this section. It can be seen that in both cases, a strong shear layer exists on the dorsal surface of the wing and is generally attached to the wing surface. In the experiment, the shear layer on the ventral side of the wing is not visible due to the shadow effect. Both figures show that a large clockwise vortex is located in the wake of the wing and is about one chord length away from the trailing edge, though the strength of vortex is weaker in the simulation. Overall downwash is created in both cases, which corresponds to lift production. There are also other visible differences between the two plots. In particular, the vortices in the experiment appear to be multiple blobs above the wing surface, while in the simulation a continuous vortex sheet is formed and is slightly separated from the wing near the leading edge. We point out that variations in the wing kinematics of bird

individuals may have led to discrepancies in the flow field observed here. In addition, some of these differences are likely caused by low resolution in the experiment where around 17 points per cm were used for the velocity field. In the simulation, 30 points per cm in the baseline grid and 40 points per cm in the finest grid are employed around the wing. Furthermore, the two grids displayed a consistent form of shear layers.

We further compare the bound circulation around the wing chord with the data from the experiment. Fig. 3.6 shows the phase-averaged circulation, Γ, defined as $\Gamma = \oint$, along a circular path that encloses the wing chord. The diameter of the circle is 10% greater than the chord length. Increasing this diameter by 20% only changes the maximum circulation by 5%. In Warrick et al. (2009), the phase averaged circulation is shown at 80% wingspan for the entire stroke cycle. However, their results also show that the spanwise location of the maximum circulation varies largely among the bird individuals, although in general the maximum happens between 40% to 80% of wingspan. In the current study, we found that the maximum bound circulation takes place between 50% to 70% of wingspan. Therefore, we plot Γ for 50%, 70%, and 80% wingspan locations and compare them with the experiment data. For the same reason, in the validation of the flow field we chose to use the slice at 70% of wingspan.

Fig. 3.6 shows that the present circulation at 50% wingspan matches the best with the experimental data. At both 70% and 80% wingspan, the circulation has a significant drop after the mid-downstroke. In the experimental result, the ratio of the downstroke and upstroke circulations is 2.1 ± 0.1 in magnitude. In the simulation, this ratio is 2.2, 2.3, and 2.0 for 50%, 70%, and 80% wingspan, respectively.

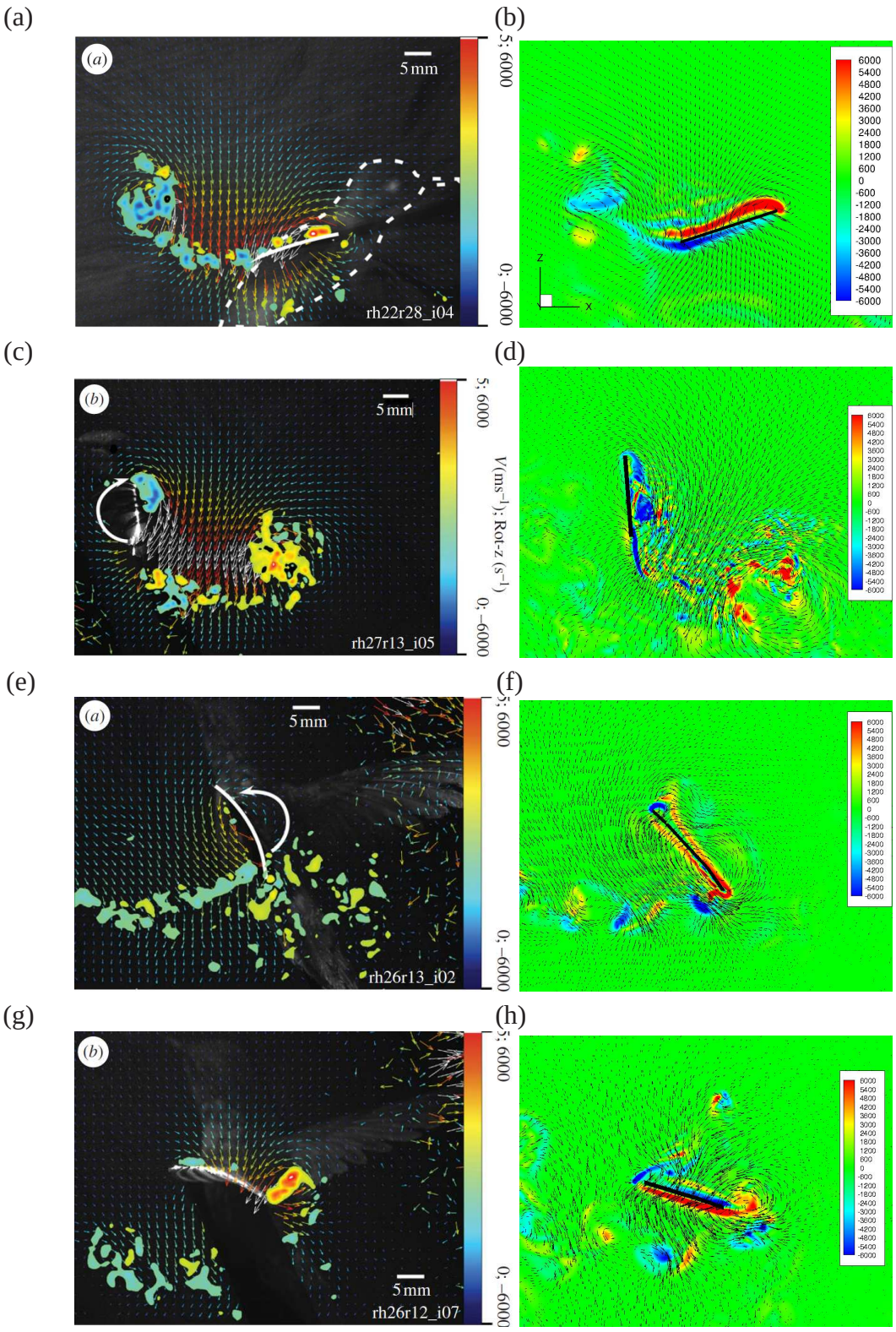

Figure 3.5: Comparison of the spanwise vorticity, ω_z, during middle downstroke (the unit is 1/s). (a,c,e,g) PIV image adapted from Warrick et al. (2009) (image usage authorized); (b,d,f,h) current simulation. (a,b) middle downstroke, (c,d) supination, (e,f) pronation, (g,h) begining of downstroke.

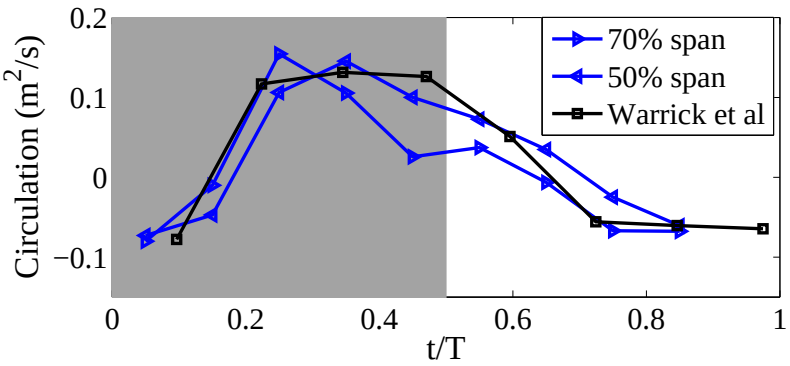

Figure 3.6: Comparison of the phase averaged bound circulation Γ between current simulation and the experimental measurement of Warrick et al. (2009) (re-plotted to include the sign of Γ), where time t is normalized by the period T.

3.3 Results and discussion

We first report the forces, power, and efficiency of the single-wing simulation and then discuss the characteristics of the forces and flow field. In the end, we will also discuss the full-body simulation.

3.3.1 Force, power, and efficiency

The global coordinate system is shown in Fig. 6.7(a), where X, Y, and Z denote the forward, spanwise, and vertical direction, respectively. The resultant force components, F_X, F_Y, and F_Z, are normalized by the fluid density, ρ, the average wing area, S, and the average tip velocity, $\bar{U}$, according to

$$C_X = \frac{F_X}{\frac{1}{2}\hat{r}_2^2 \rho \bar{U}^2 S}, \qquad C_Y = \frac{F_Y}{\frac{1}{2}\hat{r}_2^2 \rho \bar{U}^2 S}, \qquad C_Z = \frac{F_Z}{\frac{1}{2}\hat{r}_2^2 \rho \bar{U}^2 S}, \tag{3.1}$$

where C_X, C_Y, and C_Z are the force coefficients and $\hat{r}_2^2 = \int r^2 \mathrm{d}S/(R^2 S) = 0.27$ is the coefficient of the second moment of area of the wing surface about the axis passing through the wing base point and parallel to the wing. In the current study, $S = 5.68$ cm^2 and $\bar{U} = 9.51$ m/s are averaged from the reconstructed wing motion. The air density is chosen to be 1.23 kg/m^3. From these data, the reduced frequency of the wing as defined by $\pi f c/\bar{U}$ is 0.16.

Fig. 3.7 shows the time courses of the force coefficients and power coefficient. Note that the cycle-to-cycle variations seen in this figure are due to the non-periodic features in the wing kinematics. The aerodynamic power here is calculated by directly integrating the dot product between the wing velocity and the aerodynamic loading over the entire wing surface. The power coefficient is defined by normalizing the power by $\frac{1}{2}\hat{r}_3^3 \rho \bar{U}^3 S$, where $\hat{r}_3^3 = 0.185$ is the dimensionless third moment of the area of the wing. From the result the average vertical force coefficient is $\bar{C}_Z$=1.80, which corresponds to 3.12 g of total weight support provided by two wings. The total lift is about 91% of the weight of the bird. The remaining lift could be provided by the wing camber (Altshuler et al., 2004a; Warrick et al., 2005), which is not incorporated into the current model.

The most striking feature of the vertical force is that the downstroke produces clearly much higher lift than the upstroke. The data shows that C_Z averaged during the downstroke is 2.5 times of that during the upstroke, which is generally consistent with the lift estimated based on the circulation in the experiments (Warrick et al., 2005, 2009). Note that the ratio of the bound circulation between the downstroke and upstroke is 2.1±0.1 in Warrick et al. (2009). Another observation in Fig. 3.7 is that the forces and power

(a)

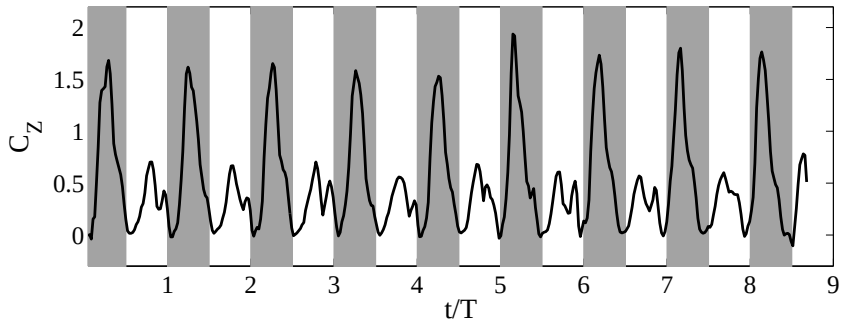

(b)

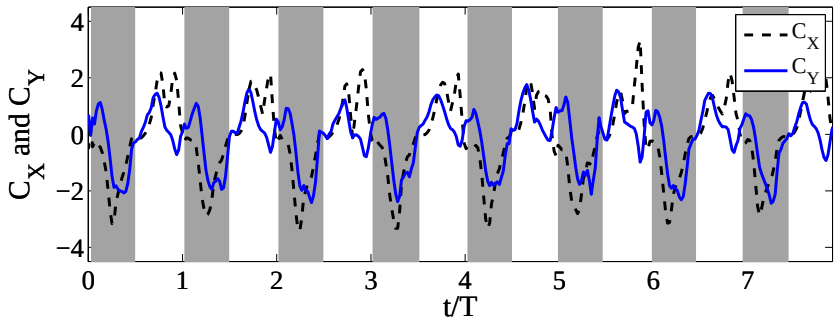

(c)

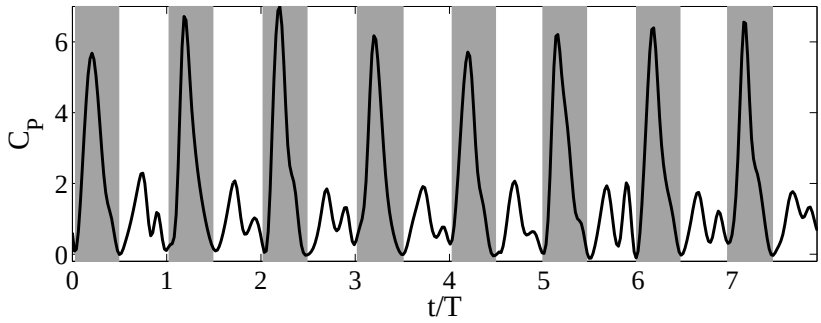

Figure 3.7: The three normalized force components C_Z (a), C_X and C_Y (b) in the single-wing simulation. (c) The power coefficient normalized by $\frac{1}{2}\hat{r}_3^3\rho\bar{U}^3S$, and positive power means work done to the flow.

contain a significant dip during the upstroke. This dip corresponds to the LEV shedding from the wing, which will be discussed in Section 3.4.

The averaged forward force coefficient is $\bar{C_X} = 0.15$, which is much smaller than $\bar{C_Z}$. The average spanwise force coefficient is $\bar{C_Y} = 0.13$. These forces can be canceled out for the real bird when taking into consideration of two-wing symmetry (for

the Y-direction), tail motion, and possibly the bird-feeder interaction in the imaging experiment (the latter two for the X-direction).

The power coefficient in Fig. 3.7 also exhibits similar asymmetry as the vertical force coefficient. Further calculation shows that the downstroke requires 2.8 times as much power as the upstroke. The averaged power coefficient throughout the cycles is $\bar{C_P} = 1.68$. Defined as the ratio between the lift coefficient and the power coefficient, the aerodynamic efficiency of the wing is thus $\bar{C_Z}/\bar{C_P} = 1.07$. Using the dimensional values of ρ, $\bar{U}$, and S, and the body mass, we obtain the mass-specific power of the bird, which is 55 W/kg. Altshuler et al. (2004b) estimated the power consumption of the hummingbirds using the empirically derived drag coefficient measured from a revolving hummingbird wing. For the hummingbirds flying at elevation below 1000 m (body mass ranging from 2.5 to 9 g), the mass-specific power for hovering was estimated to be between 23 and 33 W/kg in their work, which is about half of the current result.

Chai and Dudley (1996) reported the oxygen consumption and therefore metabolic power input of ruby-throated hummingbirds to be around 260 W/kg. Thus, our aerodynamic power output implies a muscle efficiency of 21%. Vertebrate muscle efficiency can reach slightly less than 30%, but hummingbirds are expected to be slightly less efficient because of adaptations for maintaining continuous high mass-specific power output and due to the unmeasured cost of accelerating the wing mass during each half stroke.

The overall muscle efficiency of 21% found here is substantially greater than that re-

ported in earlier studies (e.g. Ellington (1985)) that use simpler models to predict aerodynamic power requirements and report efficiencies of around 10%. However, other recent Navier–Stokes simulations of hovering animal flight have also reported higher power requirements than predicted (e.g. Zheng et al. (2013a)) and that revolving wing experiments do not necessarily reproduce the same flow conditions and thus force coefficients as flapping wings (Zheng et al., 2013b).

3.3.2 Circulation and wing rotation

As shown in Fig. 3.6, the bound circulation around the wing chord is consistent with the measurement of Warrick et al. (2009). Furthermore, the circulation is sustained through the wing reversal. For example, during the downstroke, circulation around the translating wing is developed, and toward the end of downstroke and throughout supination, the circulation does not vanish but remains the same sign, e.g., positive or counterclockwise from the right side view. Similarly, the circulation developed during the upstroke translation remains negative throughout pronation, as shown in Fig. 3.6. The lingering circulation is caused by the pitching rotation of the wing around its own axis (Dickinson et al., 1999). Unlike a spinning cylinder in a uniform flow, this circulation cannot always be utilized for lift production (e.g., when the translational speed is zero or the wing surface is vertical and thus has zero projected area on the horizontal). Therefore, the vertical force as shown in Fig. 3.7(a) is still nearly zero at wing reversals.

To better see the phase relationship between the lift production and the wing motion, we plot in Fig. 3.8 the vertical force coefficient, the translational velocity of the wing as

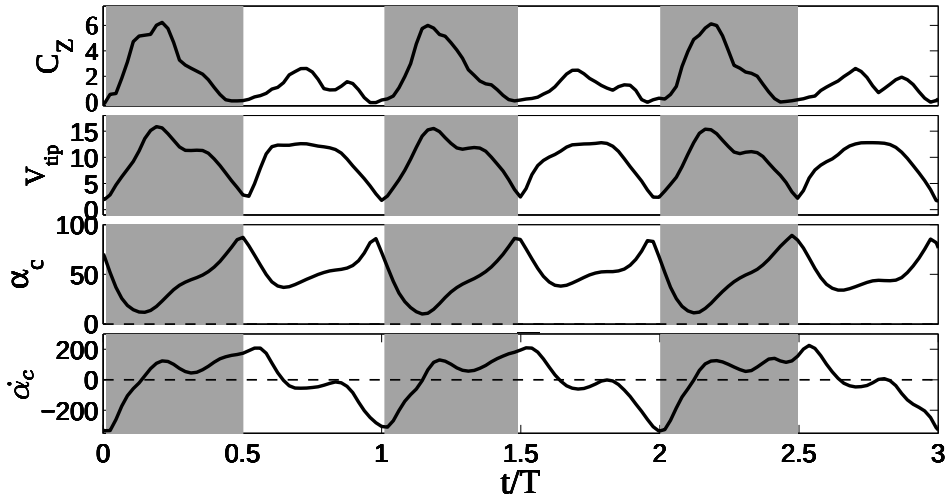

Figure 3.8: The lift coefficient, the tip velocity in m/s, the chord angle in deg., and the pitching velocity in deg./s in typical cycles (average data still taken from all eight cycles).

represented by the tip velocity, V_{tip}, the chord angle α_c, and also the pitching velocity represented by $\dot{\alpha}_c$. Fewer cycles are plotted henceforth to show details within a cycle, although statistics are taken from all cycles available. From this figure, we may see additional pitching effect other than pronation and supination: during mid-downstroke, there is a positive peak in $\dot{\alpha}_c$ and this peak also roughly corresponds to the maximum translational speed of the wing. Such backward pitching rotation would increase the circulation and, along with the wing translation, help to enhance lift production during the downstroke. On the other hand, during mid-upstroke the magnitude of the negative peak in $\dot{\alpha}_c$ is much lower. This difference could have increased the force asymmetry between the downstroke and upstroke, as will be discussed in detail next.

	$\bar{U}$ (m/s)	$\bar{U^2}$ (m^2/s^2)	S (cm^2)	α_{mid} (deg.)	$\bar{C_Z}$	$\bar{C_P}$	$\bar{C_Z}/\bar{C_P}$	$\bar{C'_Z}/\bar{C'_P}$
Downstroke	10.12	114.1	5.94	41.5	2.63	2.54	1.02	1.05
Upstroke	8.98	94.5	5.46	33.5	1.04	0.92	1.14	1.08
Ratio	1.13	1.21	1.09	1.23	2.49	2.76	0.89	0.97

Table 3.2: Comparison of the downstroke and upstroke, where $\bar{C'_Z}$ and $\bar{C'_P}$ are the lift and power coefficients rescaled by the respective $\bar{U}$ and S of either downstroke or upstroke.

3.3.3 Asymmetric lift production

(3).1 Force asymmetry

Fig. 3.7(a) shows that lift production is highly asymmetric, with the downstroke generating much greater weight support than the upstroke. The average vertical force provided by the downstroke is 0.022 N, and by the upstroke is 0.0090 N. Thus, the ratio of asymmetry is 2.5. Table 3.2 further lists the lift coefficient, the power coefficient, and the lift-to-power ratio separately for the downstroke and upstroke. It can be seen that the downstroke produces more lift, but it is also more power-consuming. By rescaling the lift and power using the respective wing velocity and surface area of each half stroke to obtain $\bar{C'_Z}$ and $\bar{C'_P}$, we see that the lift-to-power coefficient is similar for the downstroke and upstroke. Thus, despite that their aerodynamics are quite different, the two half strokes still have similar efficiency.

In Warrick et al. (2009), the force asymmetry between the upstroke and downstroke was attributed to several mechanisms, including the wing velocity, angle of attack, wing area, and camber. Except that the camber effect is not included in the current study, all the other mechanisms have been observed in the simulation, as will be discussed next.

In addition, we found that other mechanisms also have contributed to the asymmetry, which include the drag-based vertical force, wing-wake interaction, and pitching rotation. The effect of pitching rotation has been discussed in Section 3.2. So we will focus on the other effects.

First, Table 3.2 provides the comparison of a few key kinematic parameters between the downstroke and upstroke, including the average tip speed, angle of attack, wing area. It can be seen that the ratio of the average wing area between the downstroke and upstroke is only 1.09, and the ratio of the average tip speed is only 1.13. The ratio between the velocity squares is 1.21 only. That is, the combination of the wing area and velocity is much less than the ratio of 2.5 in the force asymmetry. Therefore, some other mechanisms must be significant in leading to the large imbalance of two half strokes.

3.3.4 Drag-based vertical force

First, we consider the effect of deviation, i.e., the non-reciprocal path of the wing in a stroke cycle. Observing the wing motion from the side view, we notice that the wing tip traces a roughly elliptical path whose long axis has a small angle with respect to the horizontal plane. This deviation from the mean stroke plane is shown in Fig. 3.9(a) by plotting the cycle-averaged trajectory of the right wing tip in the XZ-plane. In the figure, the mean stroke plane is tilted forward by approximately 12° with respect to the horizontal. This observation motivates us to decompose the forces generated by the wing into the aerodynamic lift, i.e., the force perpendicular to the wing translation, and the aerodynamic drag, i.e., the force opposite to the wing translation, as illustrated in

(a) (b)

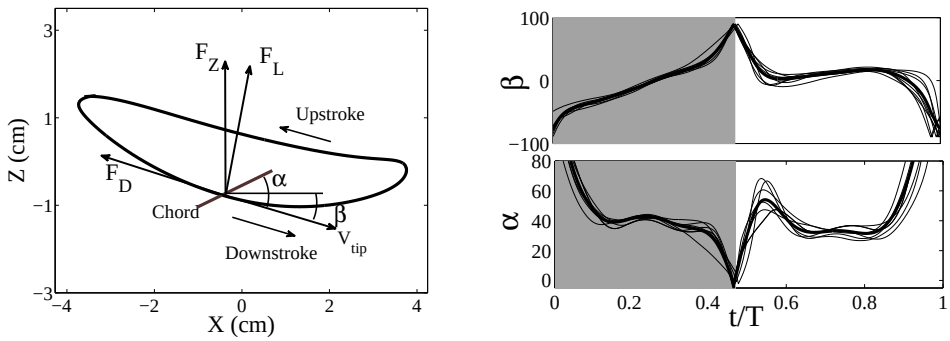

Figure 3.9: (a) The averaged trajectory of the right wing tip in the *XZ*-plane. Force decomposition in terms of the aerodynamic lift and drag is illustrated. Note that the actual decomposition depends on the orientations of the wing axis and tip velocity vector in the 3D space. (b) The instantaneous (thin line) and cycle-averaged (thick line) stroke plane angle β and angle of attack α in deg.

Fig. 3.9(a).

To do this analysis, we define the instantaneous stroke plane as the plane spanned by the instantaneous tip velocity vector and the wing axis. The instantaneous stroke plane angle, β, is the angle between this plane and the horizontal plane. Both the instantaneous and cycle-averaged values of β are plotted in Fig. 3.9(b), along with the instantaneous and cycle-averaged angle of attack α. Note that these two angles are defined in the 3D space and are shown in the 2D plot in Fig. 3.9(a) for illustration purpose only. It can be seen that after the pronation, β is around -50° and then drops in magnitude during more than half of the downstroke. During early downstroke, the angle of attack is large and drops from 80° to 39°. The two angle histories indicate that during early downstroke the wing is pressing downward while sweeping forward. Toward the end of downstroke, β becomes positive, but its magnitude is less than 25° before supination. In comparison, during the upstroke β is around 10° and only varies slightly.

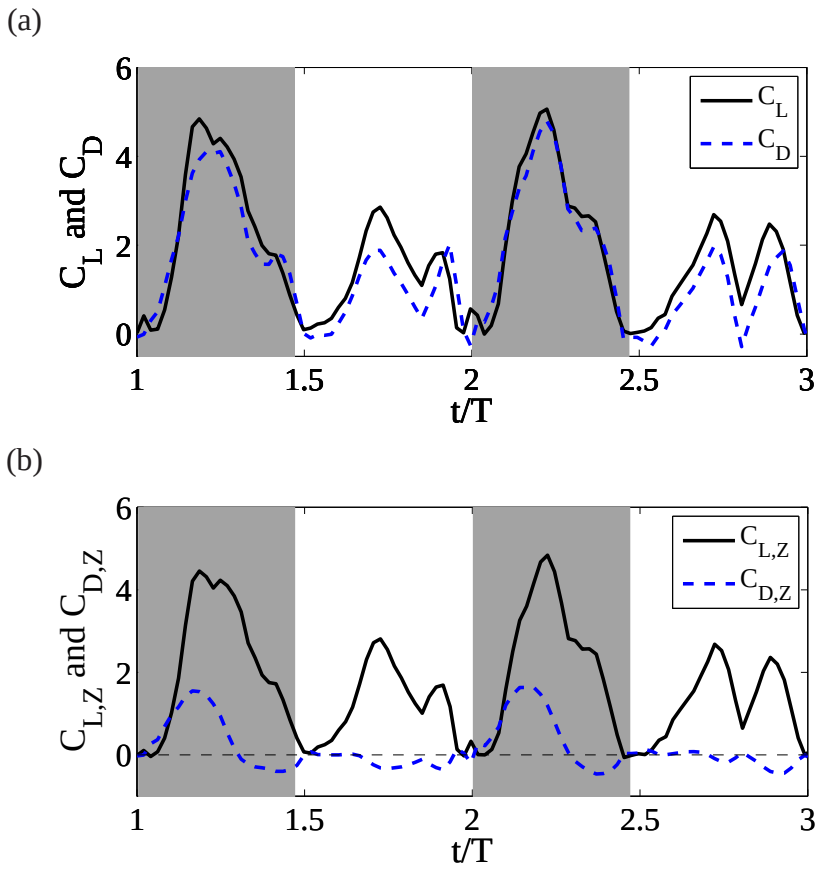

Figure 3.10: (a) Normalized aerodynamic lift and drag for two typical cycles. (b) Vertical components of C_L and C_D. Average data are calculated from all eight cycles.

	$\bar{C}_L$	$\bar{C}_D$	$\bar{C}_L/\bar{C}_D$	$\bar{C}_{L,Z}$	$\bar{C}_{D,Z}$
Downstroke	2.22	2.30	0.98	2.00	0.63
Upstroke	1.26	0.81	1.54	1.19	-0.12
Ratio	1.80	2.85	0.63	1.72	–

Table 3.3: The aerodynamic lift, drag, and their vertical component for both downstroke and upstroke. All forces are normalized in the same way as described earlier.

We define the resultant force normal to the instantaneous stroke plane as lift, F_L, and the force opposite to the direction of the instantaneous tip velocity as drag, F_D. Fig. 3.10 shows the normalized lift and drag by $\frac{1}{2}\hat{r}_2^2\rho\bar{U}^2S$, C_L and C_D, and also their projections in the vertical direction, $C_{L,Z}$ and $C_{D,Z}$, for two cycles. In Fig. 3.10(a), C_L and C_D correlate with each other and have similar magnitude. The average data are listed in

Table 3.3 separately for the downstroke and upstroke. Fig. 3.10(b) shows that during the downstroke, drag has a significant positive contribution to the vertical force during the first half of the downstroke and has only a small negative contribution during the second half of the downstroke. During the upstroke, drag has mostly negative contribution, and the magnitude is small. On average, the drag-based vertical force, $C_{D,Z}$, is 0.63 or 24% of the total vertical force C_Z during the downstroke, and it is -0.12 or 12% of C_Z during the upstroke. Since $C_{D,Z}$ of the downstroke is 61% of C_Z of the upstroke and $C_{D,Z}$ of the upstroke is small, we can conclude that drag contributes 0.61 out of the asymmetry ratio 2.5 in the vertical force.

Fig. 3.10(a) and (b) also show that after excluding the drag-based vertical force, the lift coefficient, C_L, is still asymmetric between the downstroke and upstroke, and so is its vertical component, $C_{L,Z}$. On average, the downstroke-to-upstroke ratio in C_L is 1.80.

3.3.5 Wing speed and angle of attack

As pointed out by Warrick et al. (2005), the differences in the translational speed and angle of attack between the downstroke and upstroke may have been a major effect for the lift asymmetry. To test this hypothesis, we designed a revolving-wing model for the current hummingbird. In this model, a rigid wing with a flat surface is created by projecting the actual wing during a mid-downstroke onto a plane (so the spanwise twist is eliminated), and the modified wing accelerates from the stationary position to a maximum velocity and then continues to revolve at that velocity (see Fig. 3.11). The

stroke plane is horizontal, and the angle of attack is kept constant throughout the entire process. Two cases are simulated in this test. In the first case, the wing tip follows the translation history of the wing tip in an actual downstroke chosen from one typical cycle, from 0 to the maximum velocity 15 m/s within the time period $0.2T$, and the angle of attack is $\alpha = 41°$. In the second case, the wing tip follows the translation history of an actual upstroke of the same cycle, from 0 to the maximum velocity 12 m/s within the time period $0.15T$, and the angle of attack is $\alpha = 28°$. The air properties (density and viscosity) remain the same in this setup.

The results show that the ratio of the lift during steady translation is 1.57 between the downstroke revolving wing and the upstroke revolving wing. Thus, the combined effect of translation and angle of attack is confirmed. However, it should be noted that comparing the revolving wing and flapping wing, the transient histories of lift display considerable differences, as seen in Fig. 3.12. This result suggests that the rotational motion of the flapping wing during the acceleration phase is still important.

3.3.6 Wing-wake interaction

Wing-wake interaction is a unique feature of flapping wings. In the previous study of the aerodynamics of the fruit fly, Dickinson et al. (1999) suggest that the wing-wake interaction enhances lift production and is able to generate a peak force at the beginning of a half stroke if the angle of attack is reversed timely (which is the case for advanced pitching and symmetric pitching). It would be interesting to see to what extent a similar effect exists in the hummingbird flight, and also whether this effect influences

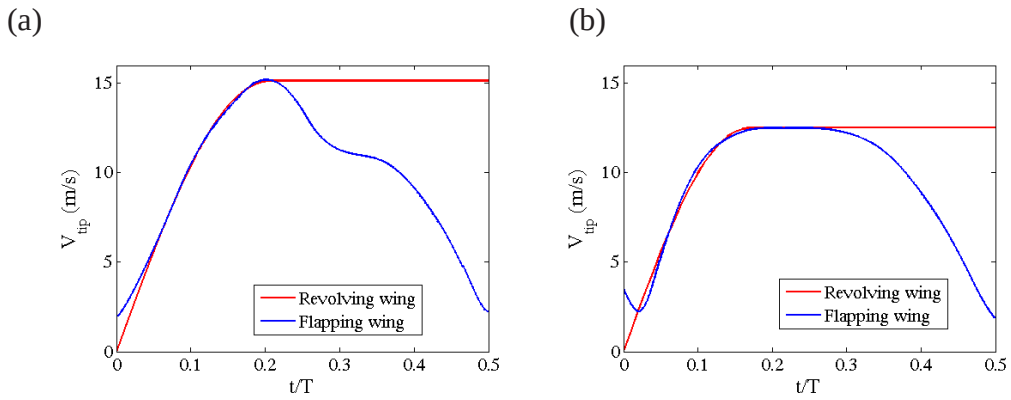

Figure 3.11: Comparison of the wing tip velocity between the flapping wing of the revolving wing. (a) downstroke; (b) upstroke. Note that for the flapping wing, the wing tip never has a moment of 'zero' velocity since the velocity vector always has a non-zero component. The acceleration period of the revolving wing is approximated with a sinusoidal function.

the downstroke and upstroke differently.

First, the lift graph in Fig. 3.7 shows that there is no clear peak in C_Z in the beginning of either downstroke or upstroke. To investigate the presence of the wing-wake interaction, in Fig. 3.13 we visualize the flow in a XZ-plane shortly after the wing reversal by plotting the velocity vectors tangent to the plane. In Fig. 3.13(a) where a typical downstroke is shown, the wing moves somewhat downward and translates at a lower elevation, and this allows the wing to capture the opposite flow produced by the preceding upstroke. Note that the opposite flow also travels downward due to the overall downwash. On the other hand, in Fig. 3.13(b) where a typical upstroke is shown, the wing moves somewhat upward and translates at a higher elevation, and thus it misses the opposite flow produced by the preceding downstroke. Therefore, qualitatively speaking, the downstroke benefits more from the wing-wake interaction than the upstroke, although the interaction does not generate a separate lift peak because of its timing.

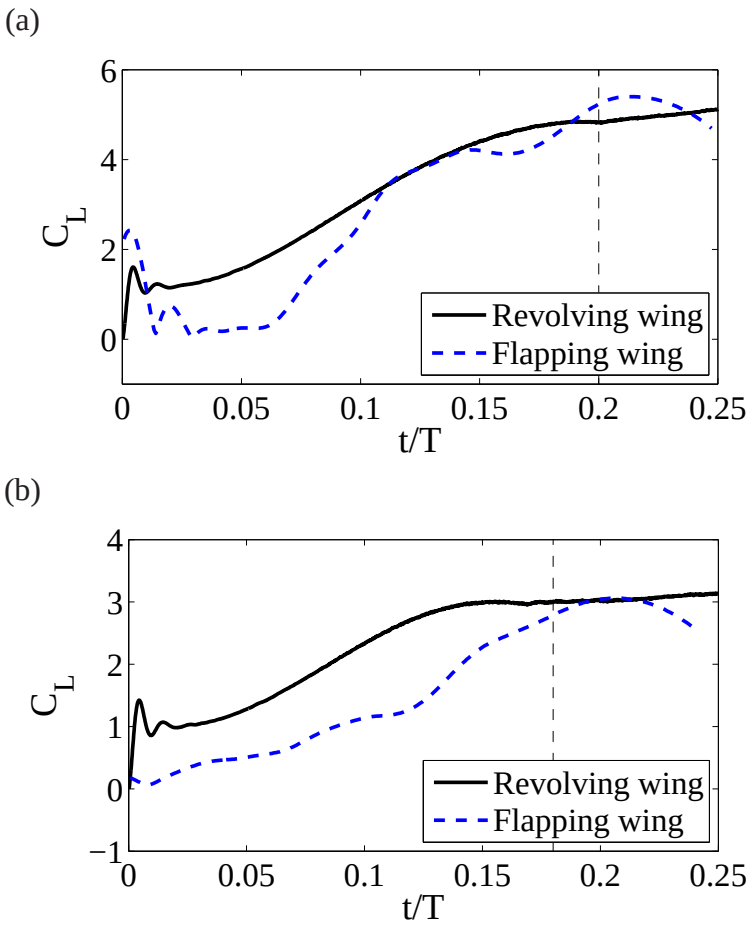

Figure 3.12: The revolving wing versus the flapping wing in the production of lift. (a) Downstroke and (b) upstroke. Only one typical stroke cycle is used in this test. The vertical dashed line represents the time period of wing acceleration. All forces are normalized by the same factor.

To further the investigation, we simulate each half stroke in separate runs with otherwise identical wing kinematics. The start and end of the simulation are based on the observation of the wing positions at pronation and supination. Thus, the effect of wing-wake interaction is excluded in such isolated wing strokes. One issue to bear in mind is that in the isolated strokes, the wing does not encounter a mean downwash as it does in the continuous strokes. The downwash reduces the effective angle of attack and thus weakens lift production.

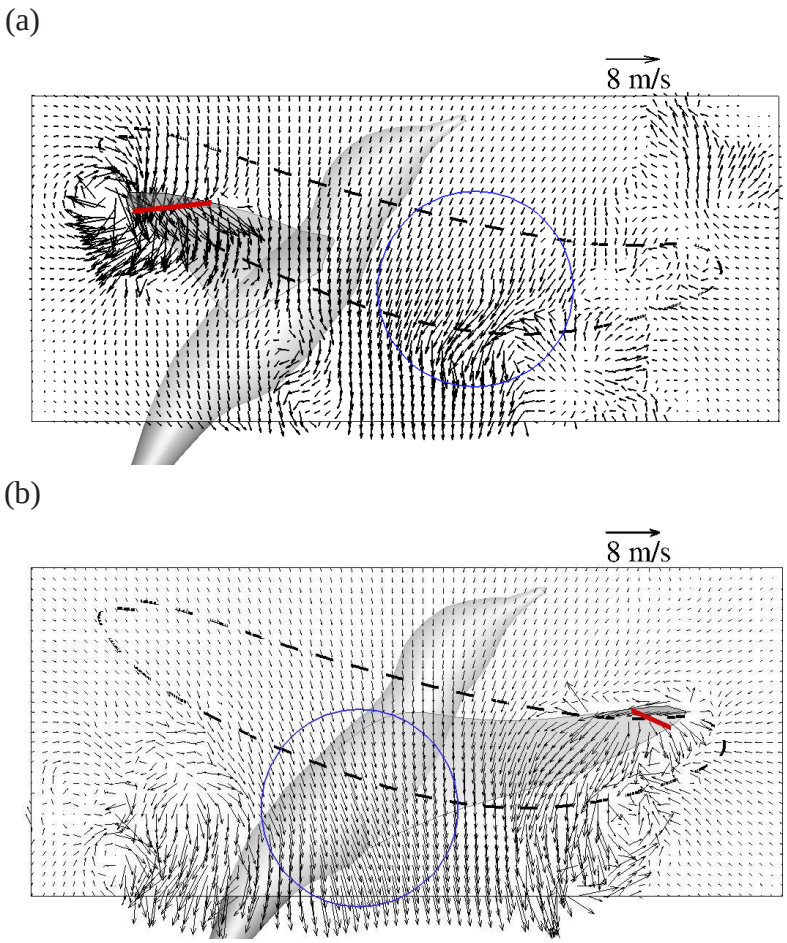

Figure 3.13: Typical asymmetric wing-wake interaction shown in a spanwise slice for (a) an early downstroke at $Y = 70\%$ wingspan and $t/T = 0.1$, and (b) an early upstroke at $Y = 50\%$ wingspan and $t/T = 0.6$. The dashed line indicates the tip trajectory of this cycle, and the circle indicates the opposite flow caused by the preceding half stroke. The chord is shown as a thick line. The bird body was not included in the actual single-wing simulation.

Fig. 3.14 shows the lift coefficient, C_Z, of the isolated strokes along with the data for the continuous strokes. In the first downstroke, the two simulations produce identical results and thus are not shown. For the other strokes, notable differences can be seen between the two simulations. For downstrokes, lift produced by the isolated strokes is close to that produced by the corresponding continuous strokes, while for the upstrokes, the isolated strokes produce greater lift than the continuous strokes. On average, the

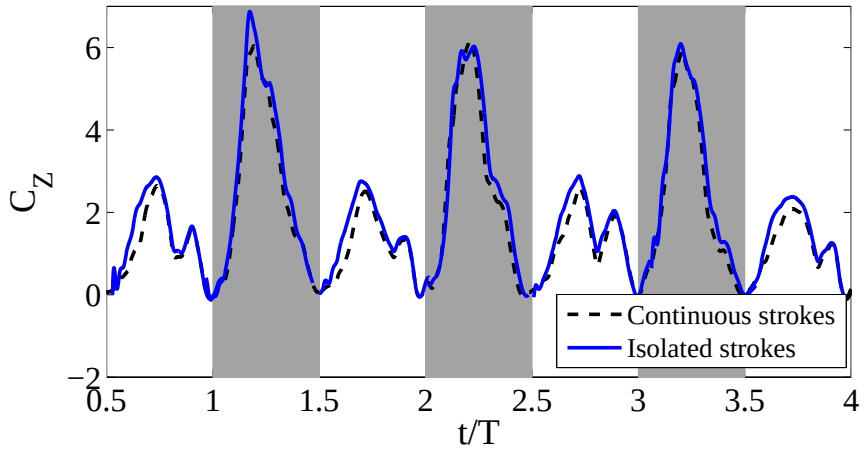

Figure 3.14: Lift production of isolated wing strokes and continuous strokes. Average data are calculated from all eight cycles.

ratio of lift between the continuous and the isolated strokes is 93.2% for downstroke and 83.1% for upstroke. This result suggests that for the present hummingbird, the lift-enhancing effect of the wing-wake interaction does not exceed the mitigating effects of other possible mechanisms present, e.g., the downwash. On the other hand, the wing-wake interaction does affect the lift asymmetry, as the downstroke-to-upstroke ratio in the vertical force is reduced to 2.2 for the isolated strokes.

Finally, it should be noted that the upstroke-downstroke force asymmetry was also observed in the hovering flight of some insects such as the hawkmoth (Zheng et al., 2013a) and fruit fly (Fry et al., 2003), though for the fruit fly the upstroke produces greater vertical force. It may be possible some of the effects discussed in the present study have led to the observed asymmetry. For example, from the tip trajectory of those insect wings and the force history provided in the references (Zheng et al., 2013a; Fry et al., 2003), one can see a similar correspondence between the downward wing translation and the large lift production, i.e., a phenomenon that could have to with the

drag-based effect.

3.3.7 Three-dimensional vortex structures

Fig. 3.15 shows a few selected snapshots of the three-dimensional flow field in a stroke cycle, which is identified by plotting an isosurface of the imaginary part of the complex eigenvalue of the instantaneous velocity gradient tensor (Mittal and Balachandar, 1995a). This technique allows one to identify regions where rotation dominates over strain.

A leading-edge vortex (LEV) is developed in the beginning of the downstroke, and this LEV grows stronger and remains stably attached to the wing during most of the downstroke. During wing translation, the LEV, the tip vortex (TV), and the shed trailing-edge vortex (TEV) are connected end to end, forming a vortex loop, within which the air moves downward (Fig. 3.15(a)). Toward the end of downstroke, the wing rotates rapidly along its own axis, and the LEV is divided into two branches, known as dual LEV (Harbig et al., 2013), as seen in Fig. 3.15(a). Corresponding to the stable LEV, there is no clear lift drop throughout the downstroke translation. At the end of downstroke, the LEV starts to shed from the wing as seen in Fig. 3.15(b). Another feature of the downstroke is that the wing catches the vortex loop produced by the preceding upstroke and disrupts this loop through the wing-wake interaction.

During the upstroke, an LEV is also formed in the beginning (Fig. 3.15(c)), but the distal portion of this LEV is pinched off during mid-upstroke, as shown in Fig. 3.15(d).

Correspondingly, there is a visible dip in the vertical force around the same time of the upstroke shown in Fig. 3.7(a). Later, the LEV will be formed again and will also form branches like dual LEVs. As discussed earlier, during the upstroke the wing misses the wake produced by the preceding downstroke. As a result, the vortices generated by the downstroke are better preserved in the wake.

Fig. 3.15 also shows that the wake contains many slender-shaped vortices. These vortices are formed mainly due to breakup of the TV and TEV at the current high Reynolds number. This flow behavior is consistent with the result of a recent work (Harbig et al., 2013) that demonstrated a similar phenomenon of vortex breakup at Re = 1500. To further confirm the accuracy of these vortices, we have compared the simulations from the baseline and the finest meshes as described in Section 2.2, and the results show that the general characteristics of the vortices are consistent. In the regions far away from the wing, the isolated vortices likely contain artificial effect due to reduced resolution there.

3.3.8 Full-body simulation

A full-body model of the hovering hummingbird is also created by using symmetric kinematics for the left and right wings. The body of the bird is approximated by a sequence of ellipses with different sizes and aspect ratios. The bird model is run in an extended domain in the Y-direction. The typical flow field is shown in Fig. 3.16 for mid-downstroke and shortly after supination. From the vortex structures in the flow, we notice that LEV and the tip vortex during the downstroke are similar to those in the

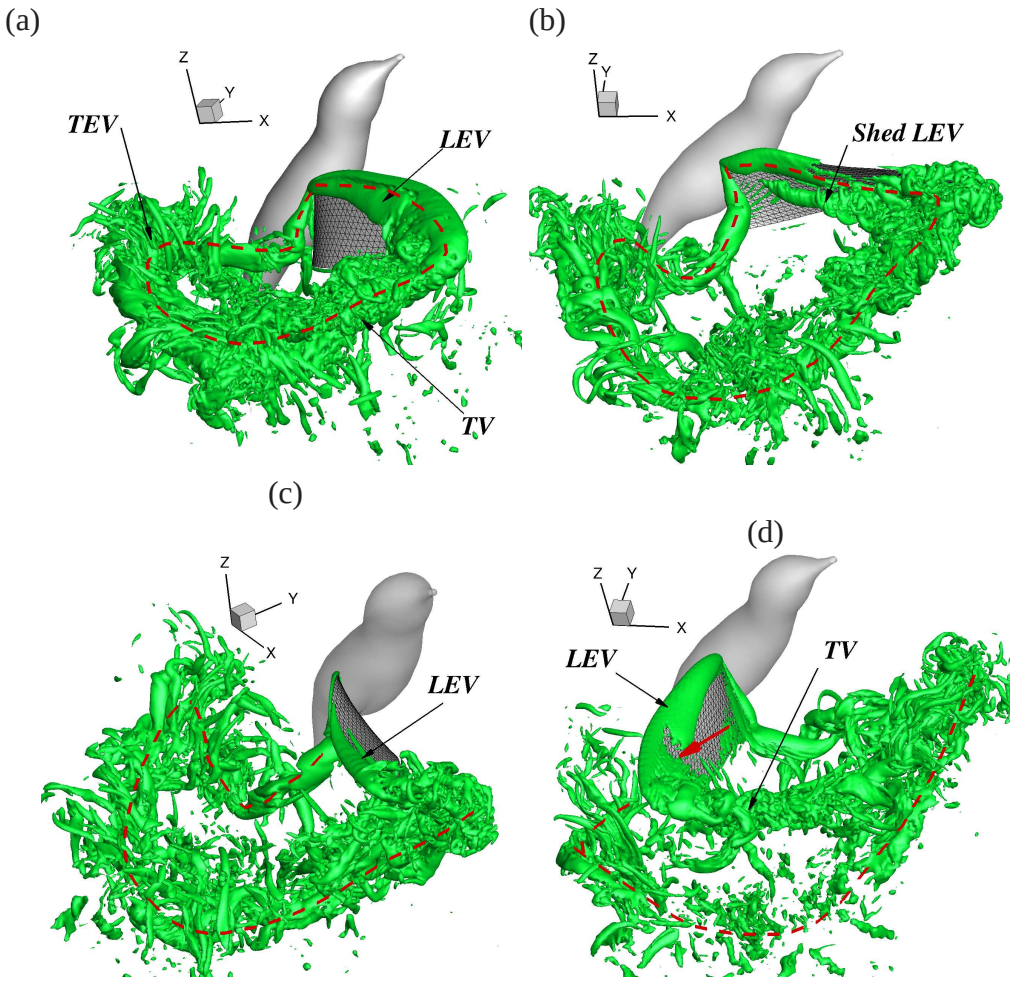

Figure 3.15: Three-dimensional vortex structures in the flow during a stroke cycle, where the time stamp from (a) to (d) is $0.37T$, $0.51T$, $0.58T$, and $0.78T$. The vortex loop from the downstroke is marked by a dashed line. The thick arrow in (d) indicates the location where the LEV is pinched off.

single-wing simulation. However, during supination the two wings are near each other (the included angle is about 30°). The flows around the two wings are close enough to interact. In particular, when the wings move away from each other, the vortices generated from each wing during grow and collide with one another. The interaction is complex and leads to further breakup of the vortices. Other than that, the major vortex structures, such as the LEV and TV, are similar to those seen in the single-wing simulation.

Despite the effect of the wing-wing interaction on the three-dimensional vortex structures, the lift production is not significantly affected. Fig. 3.17 provides a comparison of the lift coefficient between the full-body and the single-wing simulations. It can be seen that the forces from the two simulations are very close to each other. This result suggests that the wing-wing interaction and the wing-body interaction do not play an important role in lift production of the hummingbird.

3.4 Conclusion

A three-dimensional simulation was performed for a hovering hummingbird with the realistic wing motion reconstructed from imaging data. The simulation captures the lift and power characteristics in a stroke cycle and also details of the flow field. Our result confirms and provides specific data for the lift asymmetry that was previously suggested based on the measurement of the circulation around the wing. Furthermore, we quantitatively analyzed the sources of the lift asymmetry and pointed out the mechanisms that lead to the asymmetry. Summarizing the results, the downstroke produces 150% higher vertical force than the upstroke. Among the factors, the wing area contributes 10% greater force, the drag-based effect contributes 60%, the wing-wake interaction contributes 30%, and the rest 50% can be attributed to the combined wing speed, angle of attack, and wing rotation.

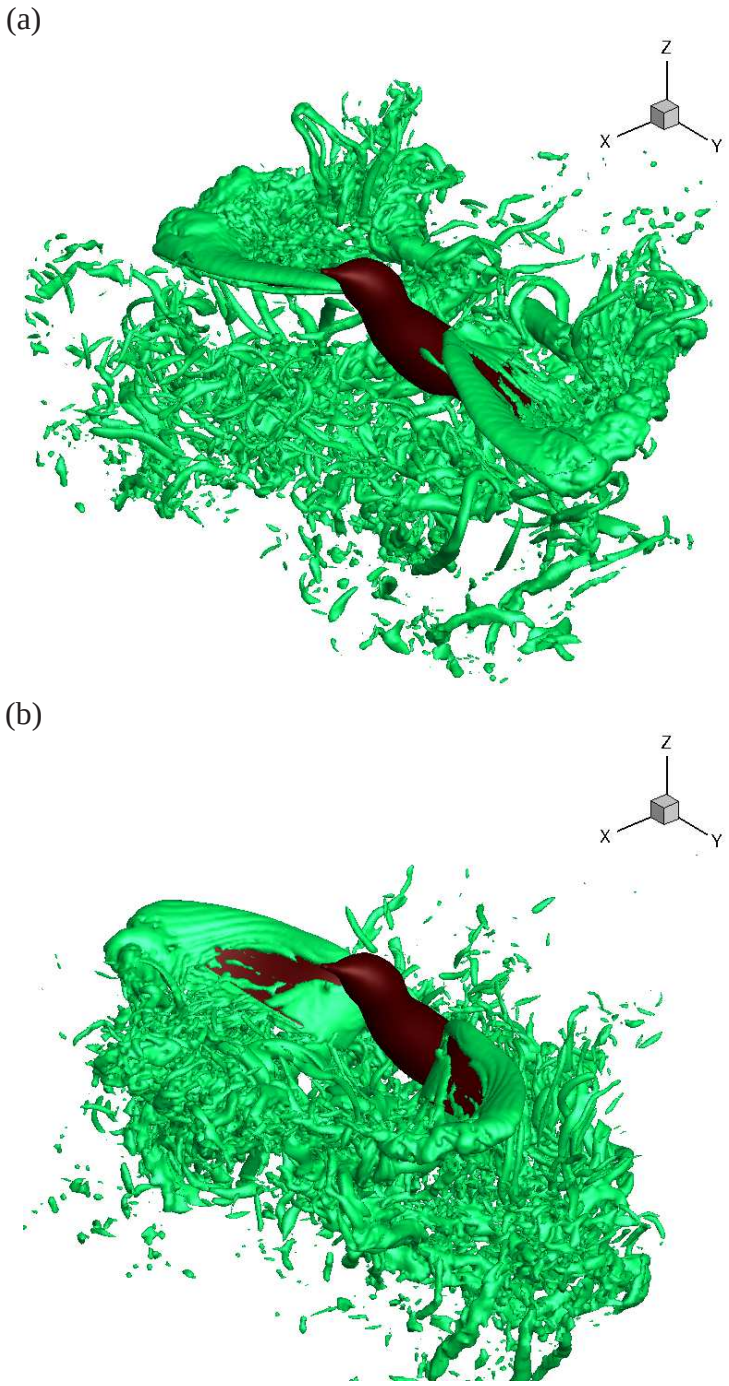

Figure 3.16: Three-dimensional vortex structures in the full-body simulation shown for a downstroke (a) and upstroke (b).

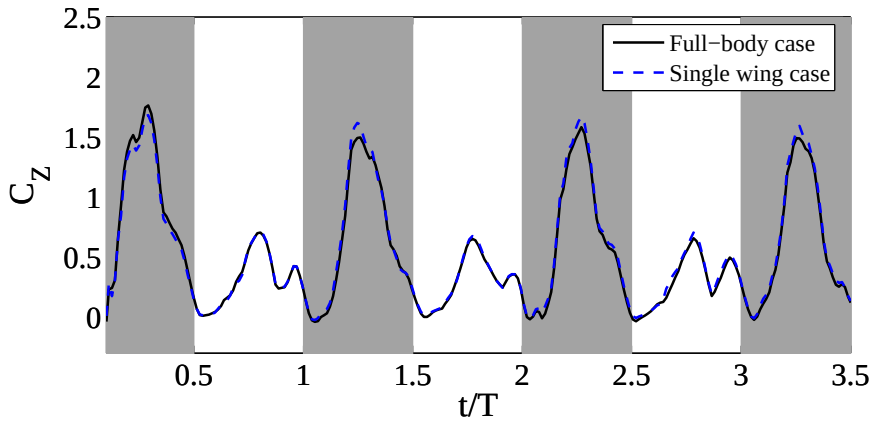

Figure 3.17: Comparison of the vertical force coefficient in typical cycles between the full-body simulation and single-wing simulation.

CHAPTER IV

PERFORMANCE OF A QUASI-STEADY MODEL FOR HOVERING HUMMINGBIRDS

4.1 Introduction

The aerodynamics of hovering hummingbirds have been investigated in several recent studies (Chai and Dudley, 1999; Altshuler et al., 2004a; Warrick et al., 2005; Tobalske et al., 2007; Warrick et al., 2009; Hedrick et al., 2012; Song et al., 2014). Previous studies have mostly focused on measurement of the flow around the bird using techniques such as particle image velocimetry (PIV) (Warrick et al., 2009; Altshuler et al., 2009; Wolf et al., 2013b), morphorlogical kinematics (Tobalske et al., 2007; Hedrick et al., 2012) and mechanical power consumption (Chai and Dudley, 1999; Altshuler et al., 2004a). The lift production was directly studied more recently by Song et al. (2014), who performed a three-dimensional simulation of a ruby-throated hummingbird (*Archilochus colubris*) based on reconstructed wing kinematics from high-speed imaging data. Aside from full CFD models, the quasi-steady method, which assumes that the state of the system at a particular time is not affected by its history, has long been used for the analysis of flapping wings (Osborne, 1951). This method later has been revised to include the translational force, rotational force, and acceleration effect to address the unique features of flapping wings (Dickinson et al., 1999; Sane and Dickinson, 2002). Compared with full CFD models, the quasi-steady method cannot provide

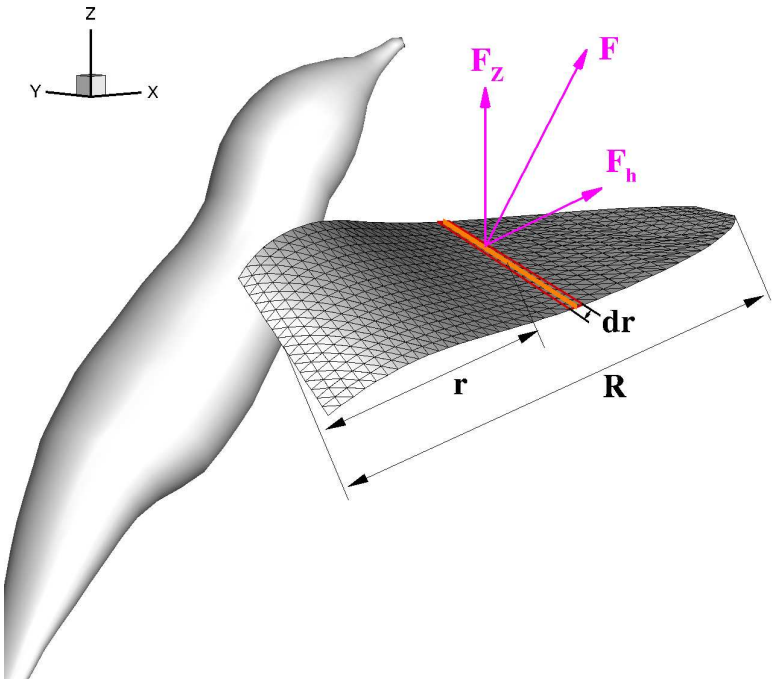

Figure 4.1: Illustration of a wing chord in the blade-element model.

information about the three-dimensional flow pattern and its prediction of force characteristics has limited accuracy. However, this method is extremely efficient in contrast with 3D simulations, and it can be used as a convenient tool for fast analysis, e.g., in optimization design (Zheng et al., 2013a) or study of maneuver flight.

In this study, we will compare force prediction of a calibrated quasi-steady model of the hovering hummingbird with that of the CFD model in Song et al. (2014), and we will use this simple model to further quantify the translational effect, the rotational effect, and the acceleration effect that can not be easily decoupled in a full CFD simulation.

4.2 Modeling approach

In the quasi-steady or blade-element model (BEM), the total force on the wing is summation of the forces on a set of infinitesimal chordwise strips, or blade elements, as shown in Fig. 4.1(b). For each chord strip, the translation velocity, rotation velocity, and angle of attack are obtained from the reconstructed wing kinematics. The total force on each strip is composed of three components: the translational force $d\mathbf{F}_{trans}$, the rotational force $d\mathbf{F}_{rot}$, and the added-mass effect (or the acceleration effect) $d\mathbf{F}_{acc}$, based on the formula in Sane and Dickinson (2002) if we ignore other effects such as wake capture and vortex shedding. Thus, the total force on the entire wing is

$$\mathbf{F} = \mathbf{F}_{trans} + \mathbf{F}_{rot} + \mathbf{F}_{acc} = \int (d\mathbf{F}_{trans} + d\mathbf{F}_{rot} + d\mathbf{F}_{acc}) \tag{4.1}$$

Next, we describe each component in this equation.

First, the translation force of a blade element consists of steady lift and drag that are functions of the angle of attack, α, defined as the angle between the element and the average stroke plane,

$$\mathbf{F}_{trans} = \frac{\rho \dot{\Phi}^2 R^3 \bar{c}}{2} \int_0^1 \hat{r}^2 \hat{c} \begin{bmatrix} C'_D(\alpha) \\ C'_L(\alpha) \end{bmatrix} d\hat{r}, \tag{4.2}$$

where ρ is the air density, $\dot{\Phi}$ is the instantaneous angular velocity of wing stroke, $\hat{r}$ and $\hat{c}$ are respectively the dimensionless spanwise location and dimensionless length of the chord normalized by $\bar{c}$, $C'_L(\alpha)$ and $C'_D(\alpha)$ are the lift and drag coefficients. The

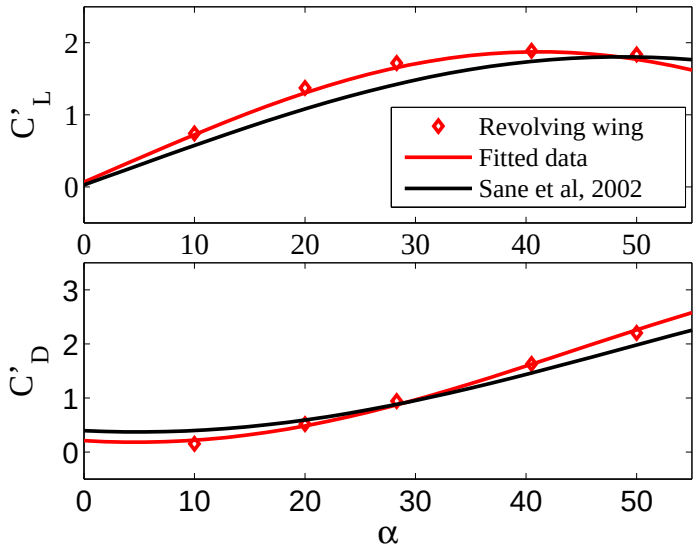

Figure 4.2: Translational force coefficient fitting from the revovlving wing simulations.

lift and drag in Eq. (4.2) are perpendicular and opposite to the translational velocity of the chord, respectively. The function forms of C'_L and C'_D are from Sane and Dickinson (2002). To obtain the constant parameters in the expressions, however, we run a series of CFD simulations of a revolving-wing model in which the wing revolves in one direction at a constant angle of attack. The wing has a rigid, flat surface from projection the hummingbird wing on a plane. The simulation setup is described in another work (Song et al., 2014). With such calibration, the fitted lift and drag functions are (also shown in Fig. 4.2)

$$\begin{aligned} C'_L &= 0.245 + 1.63\sin(2.34\alpha - 6.3) \\ C'_D &= 1.88 - 1.70\cos(2.27\alpha - 10.66). \end{aligned} \tag{4.3}$$

The rotational motion, or pitching, around the long axis of the wing can enhance

magnitude of the bound circulation, thus increasing lift force if it is combined with proper wing translation and posture. We adopt the following formula for the rotational force (Sane and Dickinson, 2002)

$$\mathbf{F}_{\text{rot}} = C_{\text{rot}}\rho\dot{\Phi}\bar{c}^2R^2\int_0^1 \hat{r}\hat{c}^2\dot{\alpha}\mathbf{n}\mathrm{d}\hat{r}. \tag{4.4}$$

where $\dot{\alpha}$ is the instantaneous pitching velocity, $\mathbf{n}$ is the surface normal of the chord, and C_{rot} is the rotational force coefficient.

To obtain the location of the rotational axis, in the current work we choose several chords along the wing to find an average value. The sample chords are chosen as shown in Fig.4.3(a). These are chosen because they represent most of the wing and are not as sensitive as the root and tip regions to the exact location of the wing root. The exact locations of the five chords are at $\hat{r} = 0.237, 0.333, 0.462, 0.604, 0.758$. The translational velocity of each chord is calculated according to $U_c = U_t\hat{r}$. Then by comparing the velocities relative to U_c at the leading edge and trailing edge, we can obtain the wing pitching axis location $\hat{x_0}$ based on Fig. 4.3(b). Finally, we take a weighted average of $\hat{x_0}$,

$$\hat{x_0} = \frac{\Sigma\hat{r}_i\hat{c}_i^{\,2}\hat{x}_{0,i}}{\Sigma\hat{r}_i\hat{c}_i^{\,2}}, \tag{4.5}$$

where i goes from 1 to 5. Fig. 4.4 shows the distribution of $x_{0,i}$ and corresponding local rotational coefficient $C_{\text{rot},i}$ for these chords. The figure shows that as the chord location moves toward the wing tip, the pitching axis moves closer to the trailing edge,

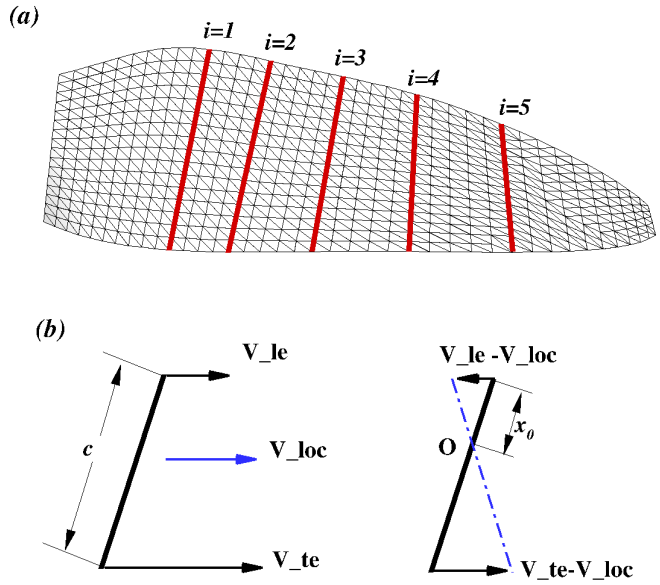

Figure 4.3: (a) Sample chords used to determine the location of the wing axis. (b) Illustration of calculation of the wing axis. V_{le}, V_{te} and V_{loc} are the leading-edge velocity, trailing-edge velocity, and translational velocity of the chord.

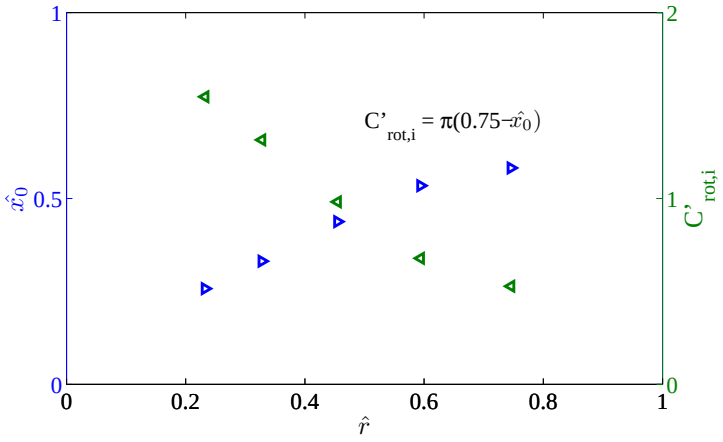

Figure 4.4: Pitching axis and the corresponding rotational force coefficient of selected chords.

leading to a smaller rotational force coefficient. Using Eq. (4.5), we have $\hat{x}_0 = 0.453$ and $C_{\text{rot}} = 0.933$.

The force model due to the acceleration effect is based on that in Sane (2001). Since the location of the pitching axis in the current model is determined specifically for the hummingbird, we rescaled the pitching acceleration term and obtain the following formula for the acceleration force,

$$\mathbf{F}_{\text{acc}} = \frac{\rho\pi\bar{c}^2R^2}{4}\int_0^1 \hat{r}\hat{c}^2[\ddot{\Phi}\sin\alpha + \dot{\Phi}\dot{\alpha}\cos\alpha]\mathbf{n}\mathrm{d}\hat{r} + \frac{\rho\pi R\bar{c}^3\ddot{\alpha}}{53}\int_0^1 \hat{c}^3\mathbf{n}\mathrm{d}\hat{r} \tag{4.6}$$

where $\ddot{\Phi}$ and $\ddot{\alpha}$ are the instantaneous angular stroke velocity and pitching acceleration, respectively.

4.3 Results

The comparison of the vertical and horizontal forces between the BEM and CFD simulation is shown in Fig. 4.3 for four typical flapping cycles. These forces have been normalized by $0.5\rho U_t^2 S\hat{r}_2^2$, where $\hat{r}_2^2 = 0.27$ is the coefficient of the second moment of area of the wing. The figure shows that the BEM is able to capture the general trend of the forces for both downstroke and upstroke. However, the horizontal force is not matched so well as the vertical force. In addition, more discrepancy could be seen for upstroke than for downstroke. For example, the double-peak feature during upstroke is completely missed by the BEM prediction. The difference corroborates that the double peaks during upstroke are related to the leading-edge vortex shedding (Song et al., 2014), a typical unsteady phenomena, and thus are not present in the current quasi-steady analysis.

	C_v	C_h	$C_{v,down}$	$C_{v,up}$	$C_{v,down}/C_{v,up}$	$C_{h,down}$	$C_{h,up}$
CFD	1.84	1.41	2.71	1.08	2.51	1.78	1.12
BEM	1.90	1.51	2.88	1.23	2.34	1.83	1.40
Mean error	3.1%	6.9%	6.3%	13.9%	6.8%	2.9%	25.1%
RMS error	26.2%	42.7%	17.1%	43.6%	–	26.7%	60.2%

Table 4.1: Quantitative comparison of the force coefficients between the BEM and CFD results, where "down" means downstroke and "up" means upstroke.

The quantitative comparison of the forces is shown in Table 4.1, where the mean and root-mean-square (RMS) differences are listed for downstroke, upstroke, and the whole cycle. It can be seen that the mean errors within an entire stroke cycle is less than 7% and thus reasonably small. The mean errors for upstroke are greater and are within 15% for downstroke and 25.1% for upstroke. More significant is the RMS error, which reaches nearly 26% for the vertical force and nearly 43% for the horizontal force. For upstroke, the RMS errors are even greater because the base numbers are relatively small.

Since the average forces predicted by the BEM are reasonably close to those given by the CFD, we move on to study the translational, rotational, and acceleration forces as predicted by the BEM. Fig. 4.3 shows breakdown of these force components. The quantitative information is provided in Table 4.2. It can be seen that the translational force dominates the force production by contributing to 82.4% of the vertical force and to 80.8% of the horizontal force. The rotational and acceleration effects have much small contributions to the force production. The rotational effect explains only 11.8% and 13.8% for the vertical and horizontal forces, respectively, while the acceleration effect explains 5.8% and 5.4% for the vertical and horizontal forces, respectively.

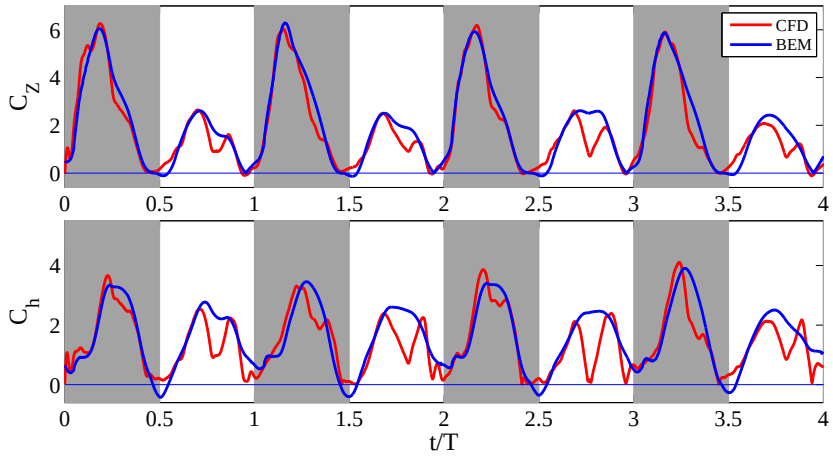

Figure 4.5: Normalized vertical and horizontal forces, C_v and C_h, given by the BEM prediction and the CFD simulation.

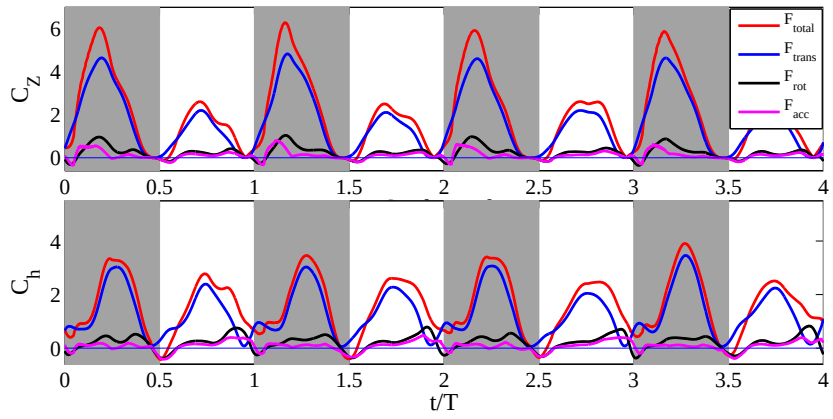

Figure 4.6: Breakdown of forces predicted by the BEM. Use "Total, Translation, Rotation, and Acceleration" in the legend.

	$C_{v,\text{trans}}$	$C_{v,\text{rot}}$	$C_{v,\text{acc}}$	$C_{h,\text{trans}}$	$C_{h,\text{rot}}$	$C_{h,\text{acc}}$
Whole cycle	1.55	0.23	0.12	1.22	0.21	0.081
	(82.4%)	(11.8%)	(5.8%)	(80.8%)	(13.8%)	(5.4%)
Downstroke	2.22	0.33	0.16	1.43	0.22	0.067
Upstroke	0.95	0.15	0.076	1.03	0.20	0.093
Downs/Upstroke ratio	2.34	2.20	2.11	1.39	1.1	0.72

Table 4.2: Coefficients of forces due to the wing translation, rotation and acceleration effects. The numbers in the parentheses represent the percentage of the force within the total force that includes the translation, rotation, and acceleration effects.

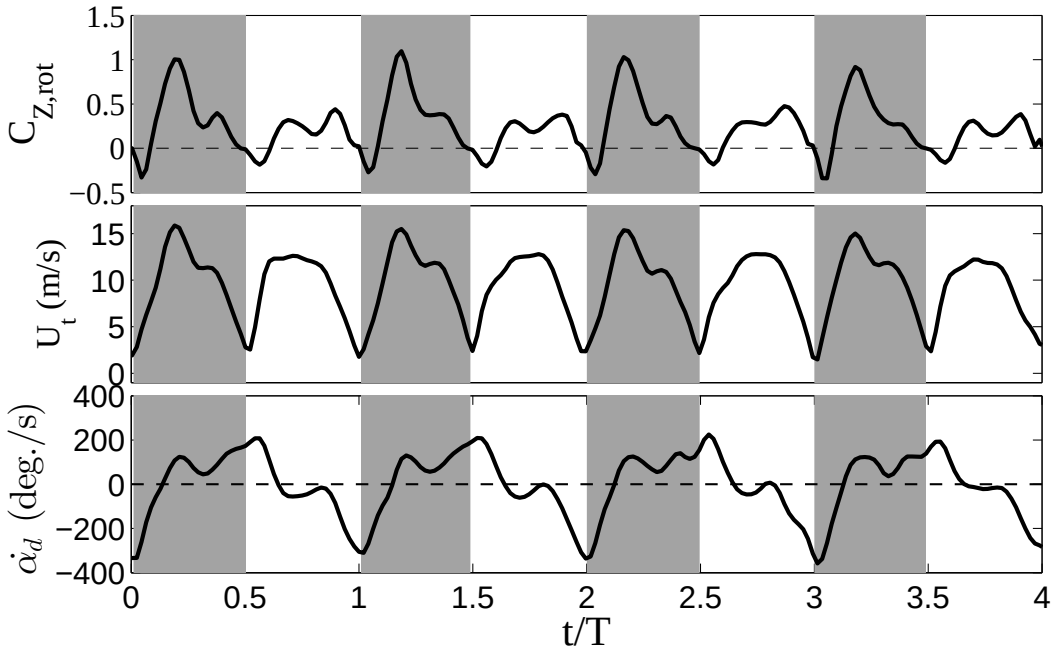

Figure 4.7: Histories of the normalized rotational force, wing tip velocity and pitching velocity of the distal wing. Use $\dot{\alpha}_d$.

The rotational effect is further shown in Fig. 4.7 where the contribution of rotation to the vertical force is plotted along with the wing translation and pitching velocity as measured for the distal half of the wing (the distal half is approximated as a flat surface for this measurement), $\dot{\alpha}_d$. It can be seen that right after pronation and supination where the wing has the greatest pitching velocity, the rotational force is negative and the magnitude is small. The peak rotational force actually happens near mid-stroke for downstroke when the wing has the greatest translation velocity and also a local peak in backward pitching, i.e., a phenomenon pointed out previously in our CFD study Song et al. (2014). During mid-upstroke, the rotation produces a similar peak but the magnitude is much lower. Toward the end of downstroke and upstroke, rotation produces a second peak.

The downstroke-upstroke ratio of the vertical force was reported to be 2.5 in the CFD simulation (Song et al., 2014). This asymmetry is also captured by the BEM result as shown in Fig. 4.3, and the ratio is 2.34 from Table 4.1. The table further shows that the translational, rotational, and acceleration effects all contribute to the asymmetry in the vertical force, and their own asymmetry ratios are all above 2. In comparison, the asymmetry in the horizontal force is much smaller. By projecting the forces in the directions perpendicular and parallel to the wing translation, we obtain aerodynamic lift and drag. The BEM result shows that during downstroke, the drag contributes to nearly 20% to the vertical force and has a significant effect on the downstroke-upstroke asymmetry. This result is consistent with the report of the previous CFD study (Song et al., 2014).

4.4 Conclusion

The quasi-steady model calibrated against the CFD result can predict the general force characteristics within a stroke cycle and the mean forces reasonably well. This model may be used in the future for analysis of unsteady flight dynamics of the hummingbird.

CHAPTER V

WING-PITCHING MECHANISM OF A HOVERING RUBY-THROATED HUMMINGBIRD

5.1 Introduction

Hummingbirds are one of the few vertebrate groups that can perform sustained hovering flight. Their superb agility has inspired development of small aerial vehicles, e.g., the robot dubbed "Nano Hummingbird" that was recently invented by AeroVironment Co., (Monrovia, CA) (Keennon et al., 2010). A key strategy that hummingbirds utilize to produce enough weight support during hovering is to invert the angle of attack of their wings during upstroke so that an extra amount of lift can be added in addition to the lift generated during downstroke (Warrick et al., 2005). A similar wing-flipping strategy is also adopted by many hovering insects, although insects have a completely different musculoskeletal system than hummingbirds. In insects, any active wing flipping must originate at the wing base because the wings have no muscles or joints. However, hummingbird wings have muscles and skeletal joints and thus may actively flex or rotate different segments. Given such a large physiological difference in their wings, it is thus natural to ask whether the mechanism of pitching actuation for hummingbird wings is the same as that for insect wings. For hummingbirds, it has been hypothesized that the source of wing inversion occurs at the wrist Stolpe and Zimmer (1939) or shoulder joint Karhu (1999). In a more recent study using high-speed three-dimensional X-ray

videography, Hedrick et al. (2012) found that hummingbirds indeed enable the high-degree supination by allowing rotation at the wrist and possibly even at other skeletal elements on the wings. However, even though they are physiologically capable of doing so, it is not yet clear whether hummingbirds need to flip wings actively since the inertial effect of the wings during translational acceleration and deceleration may be able to drive pitch reversal. In insects, there has been evidence that pitch reversal is mainly driven by the wing inertia. For example, Ennos (1988b, 1989a) calculated the inertial torque of diptera wings and concluded that the inertia is sufficient to cause the wings to flip on their own. Bergou et al. (2007) used a computational model to analyze the pitching dynamics for several insect species. Their analysis shows that a negative pitching power flows from the wing root, which means that pitch reversal originates from the wings themselves.

In the light of the work of Bergou et al. (2007), a similar study for hummingbird wings would be instrumental in understanding the mechanism of their pitch reversal. Different from previous studies, in the current work the computational model of the pitching dynamics is based on a high-fidelity reconstruction of the wing kinematics of a hummingbird, and the force/torque analysis, which includes the aerodynamic force and torque, are based on results of three-dimensional simulations. Therefore, the model provides an accurate account of the pitching dynamics not only for the wing reversal but also for an entire stroke cycle. Since pitching motion is in general important for force production of flapping wings (Dickinson et al., 1999; Sun and Tang, 2002b; Wang et al., 2004b; Dai et al., 2012b), the detailed pitching dynamics we describe through the

current work would be useful for the future study of aerodynamics of hummingbirds and other small flapping vehicles or animals.

5.2 Modeling approach

5.2.1 The wing model

The dynamic deformation of the wing such as spanwise bending and twisting have been included in the reconstructed kinematics. The two wings are assumed to have symmetric motions. A distinct feature from the wing deformation is that the wing experiences significant twist along its long axis during upstroke while the surface is relatively flat during downstroke. Such pronounced twist leads to an aerodynamically favorable angle of attack for the distal portion during upstroke. Since the greatest wing twist takes places in the middle section, we split the wing into two regions, the distal part and the proximal part, as seen in Fig. 5.1, and approximate each part as a rigid body as we consider its dynamics of rotation. The division point, denoted as F, is at 42% of wingspan from the root and roughly corresponds to the location of the finger tip of the wing (Hedrick et al., 2012). The surface area is 2.49 cm^2 (or 44% of the whole wing) for the proximal part and 3.19 cm^2 (or 56%) for the distal part.

The two sections share the same pitching axis, and the spanwise twist is represented by different values of the pitch angle for each section. To quantitatively describe the complete rotation of the wing, one wing-fixed coordinate system, 1-2-3 or *xyz*, is defined and attached to each section as shown in Fig. 5.1. The 1-axis is along the overall

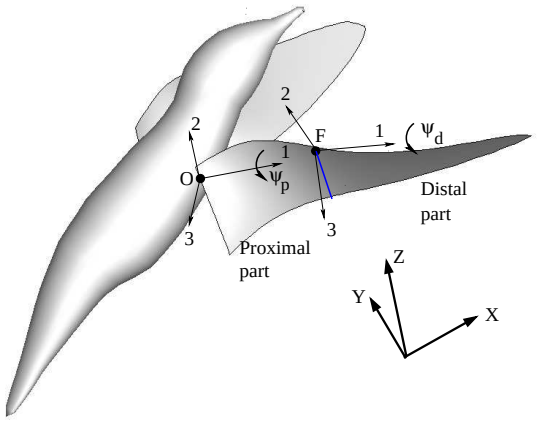

Figure 5.1: Illustration of the hummingbird wing model and the wing-fixed coordinate systems for the distal and proximal sections. The wing root and the finger tip are denoted by O and F, respectively.

wing axis, and the 2-axis is parallel to the individual wing section, and the 3-axis is perpendicular to the section and points to the dorsal side. The stroke angle ϕ, deviation angle θ, and pitch angle ψ, of the wing are described along with a definition of the coordinate transformation in Appendix A.1. The distal and proximal sections have the same values of ϕ and θ but different ψ. The time courses of these angles and the angular velocities are obtained from the reconstructed wing kinematics.

5.2.2 Description of the rotational velocity of the wing

Several coordinate systems need to be defined in order to describe the rotation of the wing in a three-dimensional space. First, the coordinate system fixed with the average stroke plane is denoted by $X'Y'Z'$, where Z' is perpendicular to the average stroke plane and X' points forward and is located in the symmetry plane of the bird body. Note that Z' is not necessary parallel to the Z-axis in the global coordinate system. The wing-fixed

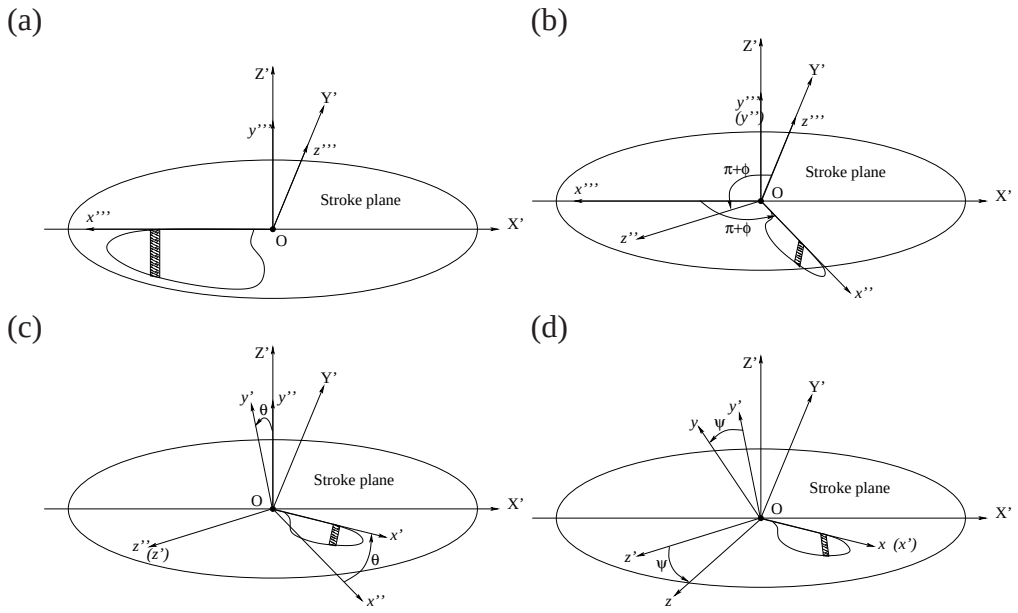

Figure 5.2: Coordinate transformation and definition of the rotation angles.

local coordinate system for the right wing is denoted by *xyz*, or 1-2-3. This system will be used to represent the entire wing if the surface is assumed to be rigid, or an individual section if the surface is divided. All coordinate systems follow the right-hand rule.

Three additional intermediate systems are defined to describe the Euler angles and the sequence of coordinate transformation. The first one is $x'''y'''z'''$ as shown in Fig. 5.2(a), which denotes the hypothetical initial position of the wing. The wing axis, x''', points toward negative X', and the dorsal axis, z''', points toward Y'. The $x'''y'''z'''$ system is then rotated around the Z'-axis by angle ϕ, i.e., the stroke angle with an initial value -π, to obtain the $x''y''z''$ system (Fig. 5.2b). The $x''y''z''$ system is then rotated around the z''-axis by angle θ, i.e., the elevation angle, to obtain the $x'y'z'$ system (Fig. 5.2c). Finally, the $x'y'z'$ system is rotated around the x'-axis by angle ψ, i.e., the pitch angle, to obtain the *xyz* system (Fig. 5.2d). From this transformation procedure,

the angular velocity vector of the wing can be written as

$$\boldsymbol{\omega} = \dot{\phi}\mathbf{e}_{Z'} + \dot{\theta}\mathbf{e}_{z''} + \dot{\psi}\mathbf{e}_{x'}, \tag{5.1}$$

where **e** is the basis vector in the coordinate system indicated by the subscript.

The basis vectors in Eq. (5.1) can be expressed in terms of the basis vectors of the *xyz* system. That is,

$$\begin{aligned}
\mathbf{e}_{x'} &= \mathbf{e}_x, \\
\mathbf{e}_{y'} &= \mathbf{e}_y \cos\psi - \mathbf{e}_z \sin\psi, \\
\mathbf{e}_{z''} &= \mathbf{e}_{z'} = \mathbf{e}_z \cos\psi + \mathbf{e}_y \sin\psi, \\
\mathbf{e}_{Z'} &= \mathbf{e}_{y''} = \mathbf{e}_{y'} \cos\theta - \mathbf{e}_{x'} \sin\theta.
\end{aligned}$$

Thus, the angular velocity becomes

$$\begin{aligned}
\boldsymbol{\omega} &= (\dot{\phi}\sin\theta + \dot{\psi})\mathbf{e}_x \\
&+ (\dot{\phi}\cos\theta\cos\psi + \dot{\theta}\sin\psi)\mathbf{e}_y \\
&+ (-\dot{\phi}\cos\theta\sin\psi + \dot{\theta}\cos\psi)\mathbf{e}_z.
\end{aligned} \tag{5.3}$$

The components of the angular velocity are

$$\begin{aligned} \omega_1 &= (\dot{\phi}\sin\theta + \dot{\psi}) \\ \omega_2 &= (\dot{\phi}\cos\theta\cos\psi + \dot{\theta}\sin\psi) \\ \omega_3 &= (-\dot{\phi}\cos\theta\sin\psi + \dot{\theta}\cos\psi). \end{aligned} \tag{5.4}$$

5.2.3 Dynamics of rotation

To describe dynamics of wing rotation, we use the angular momentum equation for each wing section projected onto the wing-fixed coordinate system associated with the section. Thus, the equation is expressed in the rotating frame of reference. For the distal section, the equation is

$$\mathbf{I}\cdot\dot{\boldsymbol{\omega}} + \boldsymbol{\omega}\times(\mathbf{I}\cdot\boldsymbol{\omega}) = \mathbf{T}_{aero} + \mathbf{T}_F, \tag{5.5}$$

and for the proximal section, the equation is

$$\mathbf{I}\cdot\dot{\boldsymbol{\omega}} + \boldsymbol{\omega}\times(\mathbf{I}\cdot\boldsymbol{\omega}) = \mathbf{T}_{aero} - \mathbf{T}_F + \mathbf{T}_O. \tag{5.6}$$

In these equations, $\mathbf{I}$ is the moment of inertial matrix of the section, and $\mathbf{T}_F$ is the torque that the proximal section exerts on the distal section, $\mathbf{T}_O$ is the actuation torque at the wing base, O, $\mathbf{T}_{aero}$ is the aerodynamic torque, and $\boldsymbol{\omega}$ and $\dot{\boldsymbol{\omega}}$ are rotational velocity and acceleration vectors, respectively, both in *the rotating frame of reference*. When calculating the moment of inertia of each wing section, the pivot point is assumed to be

at point O regardless where the origin of the local coordinate system is. Since each wing section is approximated as a flat thin surface, the symmetric inertial matrix becomes

$$\mathbf{I} = \begin{bmatrix} I_{11} & I_{12} & 0 \\ I_{21} & I_{22} & 0 \\ 0 & 0 & I_{33} \end{bmatrix} \tag{5.7}$$

where I_{13}, I_{23}, I_{31}, and I_{32} vanish. Since $I_{33} = I_{11} + I_{22}$ for a flat thin plate, the pitching component, i.e., the 1-component, of the equation for the distal section becomes

$$\begin{aligned} T_F &= I_{11}\dot{\omega}_1 + I_{12}\dot{\omega}_2 - I_{21}\omega_1\omega_3 + (I_{33} - I_{22})\omega_2\omega_3 - T_{aero} \\ &= I_{11}\dot{\omega}_1 + I_{12}\dot{\omega}_2 - I_{12}\omega_1\omega_3 + I_{11}\omega_2\omega_3 - T_{aero}. \end{aligned} \tag{5.8}$$

Here T_F and T_{aero} are the pitching component of $\mathbf{T}_F$ and $\mathbf{T}_{aero}$, respectively. We term T_F the twist torque at point F. Similarly, the pitching torque at the base, T_O, is

$$T_O = I_{11}\dot{\omega}_1 + I_{12}\dot{\omega}_2 - I_{12}\omega_1\omega_3 + I_{11}\omega_2\omega_3 - T_{aero} + T_F. \tag{5.9}$$

The aerodynamic pitching torque, T_{aero}, in Eqns. (5.8) and (5.9) is calculated using the result from our previous CFD study of the same wing kinematics, and the expression is

$$\mathbf{T}_{aero} = \int \mathbf{l} \times \mathbf{f} dS \tag{5.10}$$

Where **f** is the distributed aerodynamic force on the wing surface given by the CFD simulation, and **l** is the vector from point *O* to the point of evaluation. Both the pressure and the shear stress have been included in **f**, even though the pressure is dominant. We show in Fig. 5.3 the pressure differential of the two sides of the wing for a typical stroke cycle. From this figure, we see that the pressure load is mostly distributed over the distal section and is generally higher near the leading edge than near the trailing edge. That is, the results are overall consistent with basic aerodynamic theory of a revolving airfoil. Another observation is that the pressure center is qualitatively behind the torsional axis. This general feature of bird wings leads to a nose-down pitching torque during translation and is thus beneficial for aeroelastic stability of the wings (Förscching and Hennings, 2012).

Mass distribution of the hummingbird wing is needed to calculate the inertial matrix in Eq. (5.7). The one-dimensional distribution of mass along the wingspan was determined experimentally for a hummingbird of the same species by slicing each wing into 11 chordwise strips and measuring the mass of each individual strip. The averaged mass distribution is then scaled to match the wing length of the hummingbird used in the filming experiment. The two-dimensional wing surface consists of feathers and a musculoskeletal structure of bones and muscles that have more mass than the feathers. To incorporate such an anatomical feature, we assume that each strip at the distal section, which mainly consists of feathers, has a uniform surface density along its chord; for the strips at the proximal part, we assume that the feathered surface has the same density as that of the first distal strip adjacent to the proximal section but the additional mass

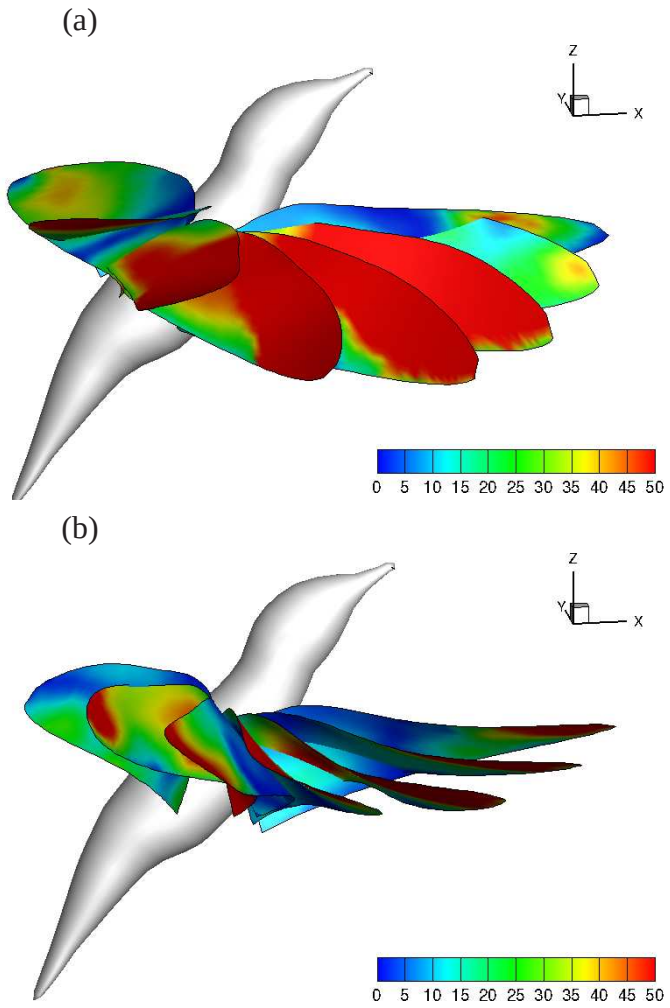

Figure 5.3: Pressure differential (unit: Pa) over the wing surface obtained from a previous CFD study (Song et al., 2014) for (a) downstroke and (b) upstroke.

of these strips is assigned to the bony structure that also corresponds to the torsional axis. This mass distribution is shown in Fig. 5.4. The elements of the inertial matrix are calculated using the local surface density. The torsional axis is assumed to be located at 1/8 of the average wing chord from the leading edge. As a result, the center of mass is behind the torsional axis, which, similar to insect wings (Norberg, 1972; Bergou et al., 2007), allows the wing inertia to facilitate pitch reversal.

(a)

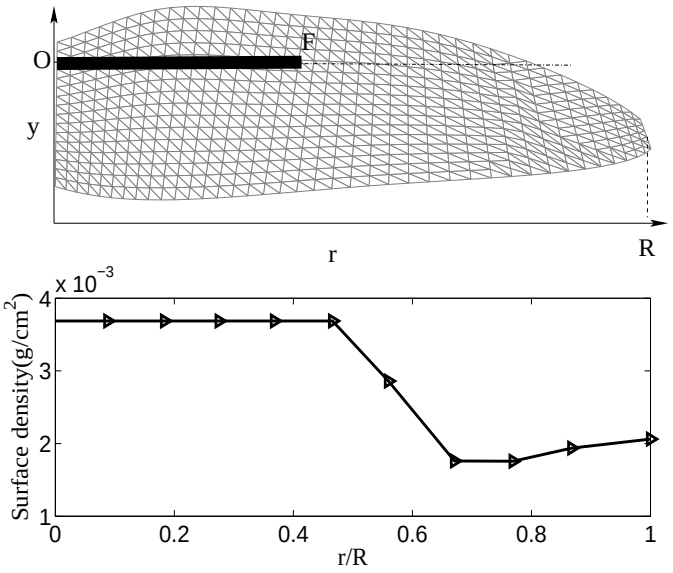

Figure 5.4: Surface density of the hummingbird wing. The dashed line indicates the torsional axis, and the thick bar represents the bony structure of the wing, which has additional mass.

5.3 Results

5.3.1 Dynamics of the distal section

The distal section is composed of feathers, which are themselves passive structures but embedded in bony and connective tissue that might permit some muscle-based active pitching rotation. An analysis of the torque and power flow between the distal and proximal sections will provide some insight into actuation of pitching for the distal wing.

Figure 5.5(a) shows the time derivative of the three Euler angles, ϕ, θ, and ψ, phase-averaged for the distal section. The angular velocities in the wing-fixed coordinate system are plotted in Fig. 5.5(b). It can be seen that these angular velocities are sub-

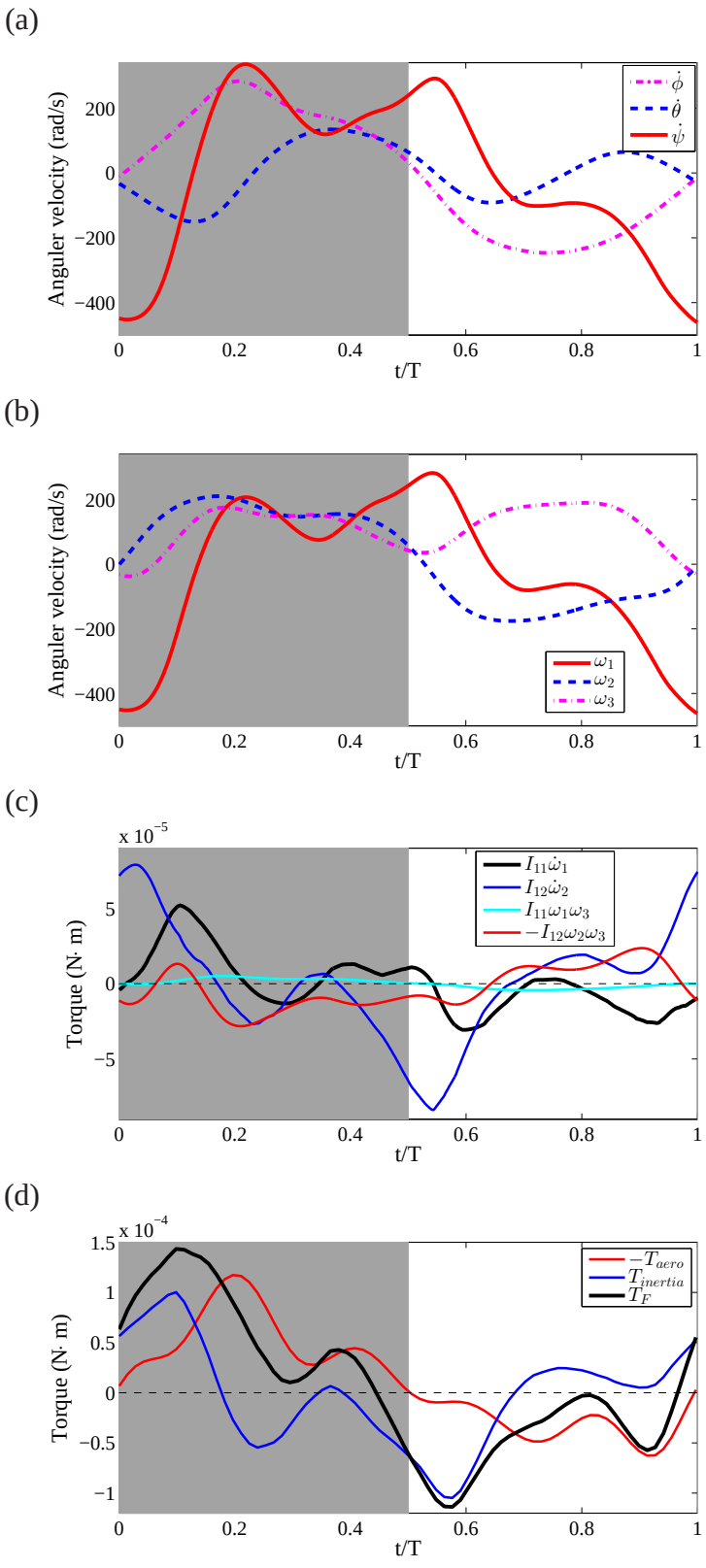

Figure 5.5: Pitching dynamics of the distal section. (a) The phase-averaged angular velocities in terms of the Euler angles. (b) The corresponding angular velocities in the wing-fixed coordinate system. (c) The inertial torque terms. (d) The sum of all inertial torques, $T_{inertia}$, the twist torque, T_F, the negative of the aerodynamic torque, T_{aero}, and the actuation torque at the root, T_O.

stantially different from sinusoidal waveform, which justifies the current analysis based on a more accurate description of the wing kinematics. The second observation is that the magnitude of the pitching velocity, $\dot{\psi}$, can reach 450 rad/s during pronation and is thus significantly greater than that of the stroke velocity, $\dot{\phi}$, whose peaks are less than 280 rad/s. Furthermore, the wing has a significant nose-up pitching motion during mid-stroke, especially during mid-downstroke, which is a lift-enhancing rotation as discussed in our previous study (Song et al., 2014). Similar characteristics can be seen from the plot of $\dot{\omega}_1$.

Figure 5.5(c) shows the torque components of the inertial effects, $I_{11}\dot{\omega}_1$, $I_{12}\dot{\omega}_2$, $I_{11}\omega_2\omega_3$, and $-I_{12}\omega_1\omega_3$. Among these components, $I_{11}\dot{\omega}_1$ is due to pitching acceleration or deceleration, $I_{12}\dot{\omega}_2$ is due to acceleration/deceleration of the wing translation, and the rest two terms are products of the angular velocities. Except for $I_{11}\omega_2\omega_3$, which is small throughout the cycle, the other three terms are all significant. The term $I_{12}\dot{\omega}_2$ is greatest during both pronation and supination reversals, which is consistent with the fact the wing comes to stop before accelerating for the next half stroke. The other two terms, $I_{11}\dot{\omega}_1$ and $-I_{12}\omega_1\omega_3$, peak during wing translation, and their magnitudes are significantly lower than that of $I_{12}\dot{\omega}_2$. These results suggest that the inertial effect due to wing translation may be sufficient to drive pitch reversal, but we will defer the conclusion until we also examine the external torques on the wing. From Fig. 5.5(c), the inertial acceleration of pitching as represented by $I_{11}\dot{\omega}_1$ reaches its maximum magnitude around $0.1T$ after the beginning of downstroke. The term $-I_{12}\omega_1\omega_3$ becomes great during mid-stroke, and as shown next, this term would help counteract the torque

exerted by the aerodynamic force.

The total inertial torque, $T_{inertia}$, i.e., summation of all four inertial terms in Fig. 5.5(c), is shown in Fig. 5.5(d) along with the negative of the aerodynamic torque, $-T_{aero}$, and the twist torque, T_F. They are related to each other by $T_F = T_{inertia} - T_{aero}$. The aerodynamic torque is much greater during downstroke and than during upstroke. This result is due to the force asymmetry between the two half strokes, which was discussed in detail in Song et al. (2014). In contrast, the total inertial torque is more symmetric between downstroke and upstroke. T_F peaks near $t/T = 0.1$ during downstroke and near $t/T = 0.55$ during upstroke. Additional peaks can be observed prior to supination and prior to pronation. Comparing the three torques in the figure, we see that during early wing translation T_{aero} is low and $T_{inertia}$ is mainly balanced by T_F. In the middle of translation, T_{aero} is great and needs to be balanced by T_F as well. At $t/T = 0.4$ and 0.9, i.e., near the end of each half stroke, $T_{inertia}$ is around zero and T_{aero} is mainly balanced by T_F. Around $t/T = 0.25$ and 0.8 we notice that $T_{inertia}$ and T_{aero} nearly cancel each other and T_F is thus minimal.

The graphs in Fig. 5.5(c,d) tell us the magnitude and phase of all the pitching torques. However, it is not straightforward to see the individual contribution of each torque to the pitching motion. Thus, we further examine the power balance of the distal section by multiplying Eq. (5.8) by ω_1 and obtaining the following expression:

$$\frac{1}{2} I_{11} \frac{\mathrm{d}\omega_1^2}{\mathrm{d}t} = \underbrace{-I_{12}\dot{\omega}_2\omega_1 + I_{12}\omega_1^2\omega_3 - I_{11}\omega_1\omega_2\omega_3}_{P_{inertia}} + T_F\omega_1 + T_{aero}\omega_1 \qquad (5.11)$$

where the term on the left-hand side represents the rate of increase of the kinetic energy of pitching, $E_{pitch} = \frac{1}{2} I_{11} \omega_1^2$, and all the terms on the right-hand side represent the power input of a certain torque. The three inertial terms on the right-hand side can be grouped as the total inertial power, $P_{inertia}$. We also define the torsional power $P_F = T_F \omega_1$, and the aerodynamic power $P_{aero} = T_{aero} \omega_1$. Eq. (5.11) then becomes

$$\dot{E}_{pitch} = P_{inertia} + P_F + P_{aero} \tag{5.12}$$

Figure 5.6 shows the comparison of these power terms phase-averaged for a cycle. Starting from $t/T = 0.9$, i.e., toward the end of upstroke when the wing performs pronation, we see that P_F is initially positive, indicating energy input from the proximal wing, and it is the torsional power that first drives the pitching motion of the distal section by counteracting the negative aerodynamic power that is relatively high because of a great pitching rate at the moment (between -300 and -450 rad/s). Then the inertial effect kicks in and takes over to drive pitching. Later at $t/T = 1$ and before $t/T = 0.1$, the inertial power is high, and meanwhile the torsional power has to become negative and large in magnitude so that the wing can finish pronation without exceeding rotation.

During mid-downstroke around $t/T = 0.25$, the torsional power is positive, and thus energy is being input from the proximal section to perform the nose-up pitching. Later around $t/T = 0.4$, a small amount of torsional power is needed to initiate the supination reversal. However, the inertial power soon becomes large enough to overcome the aerodynamic resistance and drives the reversal. Like pronation, the inertial power becomes

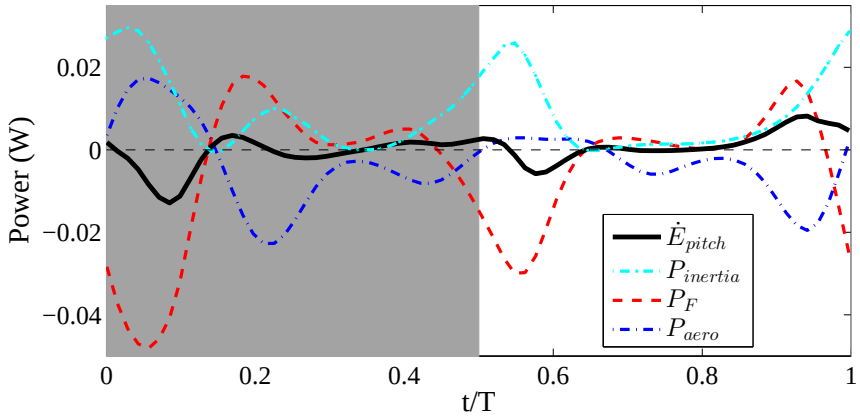

Figure 5.6: Rate of change in the pitching energy of the distal section, the power contribution of the inertia, $P_{inertia}$, aerodynamic power, P_{aera}, and torsional input, P_F.

so high that the torsional power has to be negative between $t/T = 0.45$ and 0.65 to prevent the wing from over-pitching. Note that during supination around $t/T = 0.5$, $\dot{E}_{pitch}$ is small, indicating the the distal section is mostly maintaining its pitching momentum gained earlier. During mid-upstroke when $t/T = 0.75$, only a small amount of torsional power is needed to overcome the negative aerodynamic effect.

5.3.2 Dynamics of the proximal section

The analysis of the proximal section is similar to that of the distal section. We first calculate the aerodynamic torque and all the inertial terms using reconstructed angular velocities. The twist torque T_F is known from analysis of the distal section. Thus, the pitching actuation torque at the root, T_O, is determined from Eq. (5.9).

Figure 5.7(a) shows the pitching velocity of the proximal section, $\dot{\psi}$, along with that of the distal section. Note that the two sections have the same $\dot{\phi}$ and $\dot{\theta}$. It can be seen that the two parts have significantly different pitching velocity. During early downstroke, the

negative peak of $\dot{\psi}$ reaches about -540 rad/s for the proximal section, which is greater than that of the distal section. The positive peaks of the proximal section during mid-downstroke and during early upstroke are lower than those of the distal section. Overall, the proximal section has a phase delay in pitching as compared with the distal section. Figure 5.7(b) shows the angular velocities of the proximal section in the wing-fixed coordinate system, where ω_1 has similar characteristics as $\dot{\psi}$ of the section.

The inertial torques of the proximal section are shown in Fig. 5.7(c). We see that the pitching acceleration term and translational acceleration terms, i.e., $I_{11}\dot{\omega}_1$ and $I_{12}\dot{\omega}_2$, respectively, are much greater than the other two inertial terms. These two major torques have a similar phase shift as compared with their counterparts plotted in Fig. 5.5(c) for the distal section. Compared with the distal section, the proximal section has greater $I_{11}\dot{\omega}_1$ but lower $I_{12}\dot{\omega}_2$. The sum of all inertial torques, the negative of the aerodynamic torque, and the actuation torque at the root are plotted for the proximal section in Fig. 5.7(d) along with the twist torque exerted by the distal section. Different from the distal section, the aerodynamic torque of the proximal section is much lower than the inertial torque in terms of peak magnitude. Both the aerodynamic torque and the inertial torque are much smaller than T_F and T_O. This result means that for the proximal section, the torque at the root is mainly balanced by the torque exerted by the distal section, or the proximal section transmits most of its torque at the root to the distal section.

Following the power analysis for the distal section, we multiply Eq. (5.9) by ω_1 of

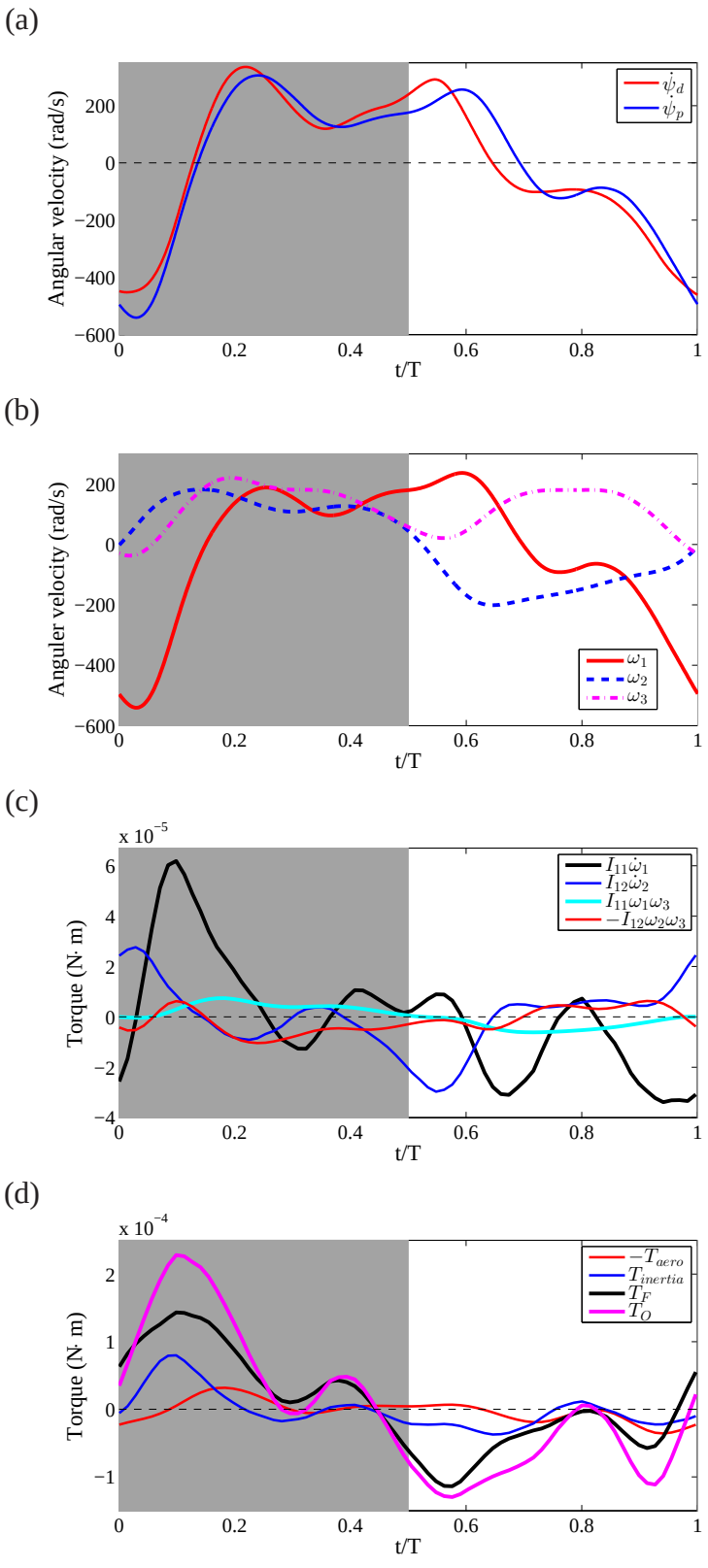

Figure 5.7: Pitching dynamics of the proximal section. (a) Comparison of the phase-averaged angular velocity, in terms of $\dot{\psi}$, between the proximal section and distal section. (b) The corresponding angular velocities in the wing-fixed coordinate system for the proximal section. (c) The inertial torque terms for the proximal section. (d) The sum of all inertial torques, $T_{inertia}$, the twist torque, T_F, and the negative of the aerodynamic torque, T_{aero}, for the proximal section.

the proximal section and obtain a similar formula for this section,

$$\frac{1}{2}I_{11}\frac{\mathrm{d}\omega_1^2}{\mathrm{d}t} = \underbrace{-I_{12}\dot{\omega}_2\omega_1 + I_{12}\omega_1^2\omega_3 - I_{11}\omega_1\omega_2\omega_3}_{P_{inertia}} + T_O\omega_1 - T_F\omega_1 + T_{aero}\omega_1. \quad (5.13)$$

Using the same notations for the power terms, we have

$$\dot{E}_{pitch} = P_{inertia} + P_O - P_F + P_{aero}, \quad (5.14)$$

where $P_O = T_O\omega_1$ is the power input from the root.

Figure 5.8(a) shows the actuation power at the root, P_O and the torsional power to the distal section, P_F. Similar to the comparison of T_O and T_F, P_O and P_F have close magnitude and phase. There difference, $P_O - P_F$, is plotted in Fig. 5.8(b) along with $\dot{E}_{pitch}$, $P_{inertia}$, and P_{aero} of the proximal section. Comparing Fig. 5.8(b) and Fig. 5.6, we see there are a few similarities between the proximal section and the distal section. First, $\dot{E}_{pitch}$, $P_{inertia}$, and P_{aero} of the proximal section all exhibit a similar trend to their counterpart of the distal section although their magnitudes are different. P_{aero} of the proximal section also has a phase delay as compared with that of the distal section, which is consistent with the pitching delay of the proximal section. Second, positive actuation power is needed to initiate the pronation reversal of the proximal section between $t/T = 0.9$ and 1, and also to nose-up pitch the section during mid-downstroke between $t/T = 0.2$ and 0.3. During early downstroke (t/T between 0 and 0.2) and early upstroke (t/T between 0.5 and 0.75) , the actuation power is negative to prevent over-pitching.

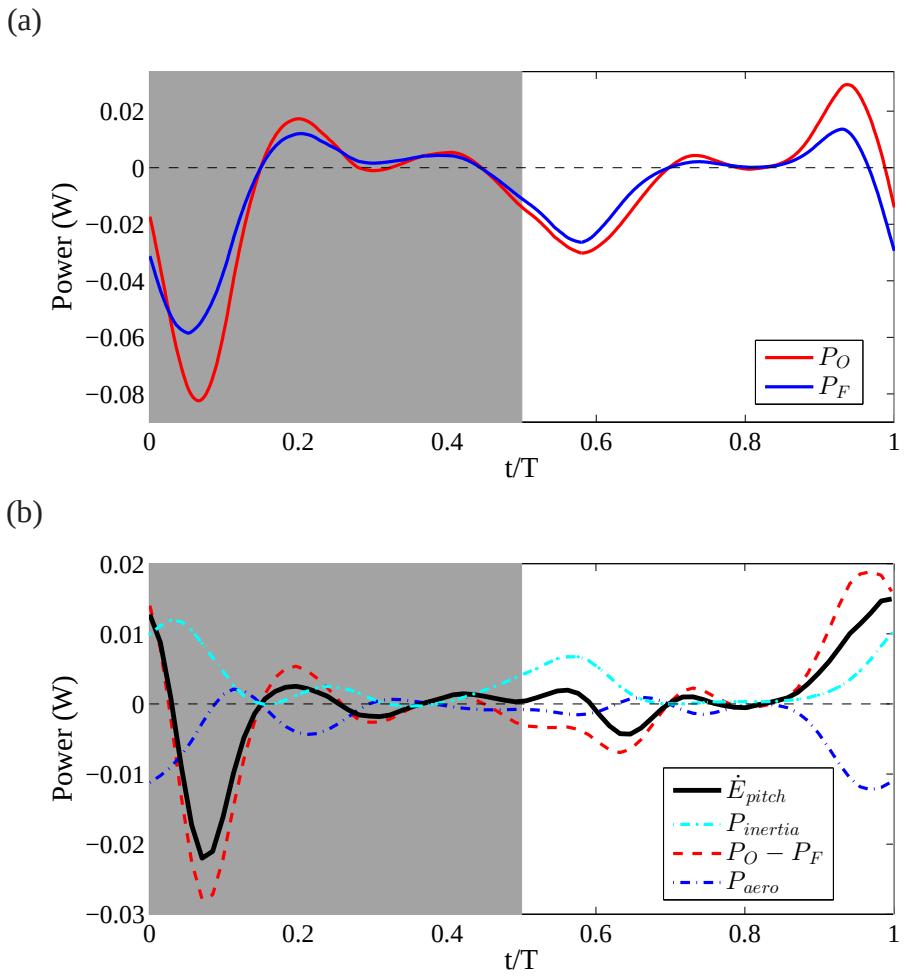

Figure 5.8: (a) Comparison of the power at the root, P_O and the torsional power to the distal section, P_F. (b) Rate of change in the pitching energy of the proximal section and the power contributions.

5.3.3 Dynamics of flapping motion

Using the current model, it is straightforward to analyze flapping motion of the hummingbird wing. We first write the other two components of Eq. (5.6) for the proximal section as

$$\begin{aligned} T_{2,O} &= I_{22}\dot{\omega}_2 + I_{21}\dot{\omega}_1 + I_{12}\omega_2\omega_3 + (I_{11} - I_{33})\omega_1\omega_3 - T_{2,aero} + T_{2,F}, \\ T_{3,O} &= I_{33}\dot{\omega}_3 + I_{12}(\omega_1^2 - \omega_2^2) + (I_{22} - I_{11})\omega_1\omega_2 - T_{3,aero} + T_{3,F}, \end{aligned} \tag{5.15}$$

where the subscripts O and F indicate the location of the torque. Eq. (5.5) can be expanded in the same manner. The torque to drive flapping motion of the wing at the root, $T_{O,flap}$, can be defined as the torque along the y'-axis in Fig. 5.2. Thus, the wing-root torque is

$$T_{O,flap} = \mathbf{T}_O \cdot \vec{\boldsymbol{e}}_{y'} = T_{2,O} \cos\psi - T_{3,O} \sin\psi. \tag{5.16}$$

The rotational velocity along the y'-axis is

$$\omega_{y'} = \boldsymbol{\omega} \cdot \vec{\boldsymbol{e}}_{y'} = \omega_2 \cos\psi - \omega_3 \sin\psi. \tag{5.17}$$

The power due to flapping motion is calculated as

$$P_{O,flap} = T_{O,flap}\, \omega_{y'}. \tag{5.18}$$

The inertial power and aerodynamic power can also be calculated by taking the dot product of the inertial torque or the aerodynamic torque with $\omega_{y'} \vec{\boldsymbol{e}}_{y'}$.

Figure 5.9(a) shows the inertial torque, wing-root torque, and aerodynamic torque of the whole wing due to flapping motion. Note that during downstroke, the wing-root torque is first balanced by the inertial torque and then by the aerodynamic torque of similar magnitude. During upstroke, the aerodynamic torque is relatively low, and the actuation torque is mainly balanced by the inertial torque. These torques are at one order of magnitude higher than the pitching torques shown in Fig. 5.7(d). The corresponding power sources are shown in Fig. 5.9(b). As expected, the inertial power

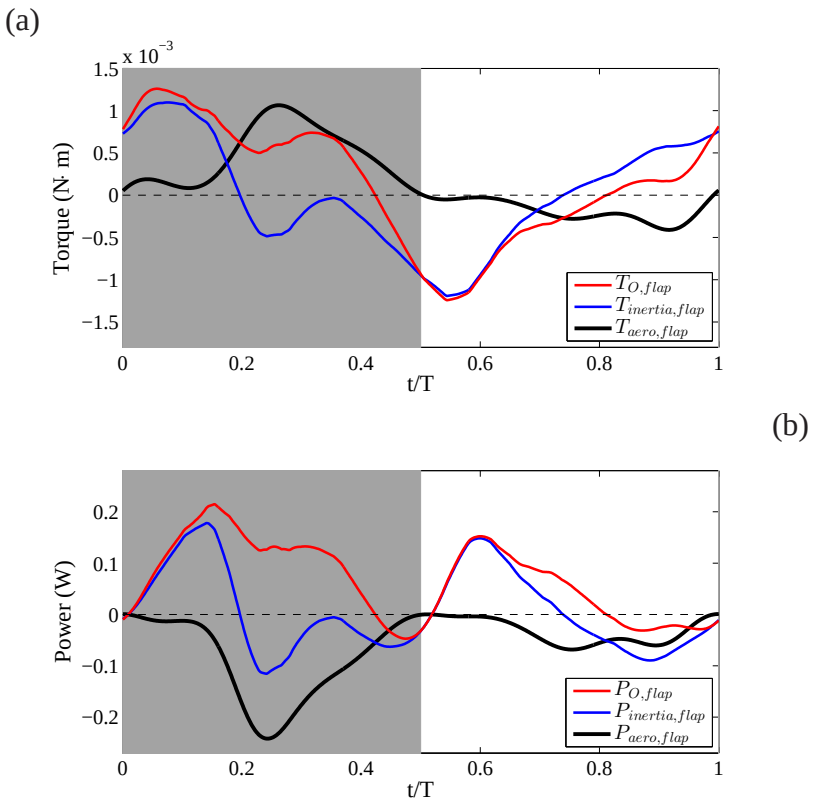

Figure 5.9: (a) The phase-averaged actuation torque at the root, inertial torque, and aerodynamic torque for flapping motion of the entire wing. (b) The corresponding power for flapping motion of the entire wing.

is negative during wing deceleration, and the aerodynamic power is always negative. An interesting observation is that, through meeting the demands of the inertial power and aerodynamic power, the wing-root power is mostly positive and no substantial negative power could be recycled at the root.

5.4 Discussion

From the analysis of the distal section, we see that the inertial effect due to wing translation, $I_{12}\dot{\omega}_2$, is large enough to drive pitching during pronation and supination. Exceptions are during early pronation when an additional torque is needed to initiate

wing rotation and also during mid-downstroke when the additional torque needs to perform nose-up pitching when the wing has maximum resistance from the aerodynamic torque (see the graph of T_F in Fig. 5.5(d)).

During most of pitch reversal, a reaction torque from the proximal section is necessary to prevent the distal section from rotating excessively. As a result, the pitching power flows from the distal section to the proximal section and assists with simultaneous pitch reversal of the proximal section. Such a reaction torque between the two sections can be provided by the connective tissue of the wing and also the obliquely aligned feathers because of their structural elasticity. From Fig. 3.3, we can see that the direction of wing twist during both pronation and supination indeed corresponds to the direction of twist torque, T_F, which indicates that the twist torque may come from the structural deformation and the wing elasticity may thus provide a passive mechanism to modulate pitch reversal. The positive power input from the proximal section to the distal section during mid-downstroke and the beginning of the pronation (i.e., P_F in Fig. 5.6) does not necessarily require muscle actuation either. Instead, it could be transmitted from the wing root by the proximal section, or it could be released from the twisted wing structure that stores energy in the form of elastic potential.

We should point out that we cannot exclude an assisting role for the muscles on the wing skeleton. These muscles may potentially increase the torsional stiffness through activation to provide the reaction torque during pitch reversal, or they might even participate pitching activation during mid-downstroke and early pronation to provide the positive power needed at those moments.

The current results imply that the pitching mechanism of the hummingbird wing may be similar to that of insects. Insects do not have muscles on their wings, and the inertial effect is sufficient to drive pitch reversal (Bergou et al., 2007). Their elastic wing structure allows the distal section to achieve greater pitch angle than the proximal section (Wootton, 1981). Furthermore, any positive power input, if needed for pitching, can also be achieved by insects at the wing base joint.

At the wing root, the torque and power characteristics are similar to those at the proximal-distal junction. This result is because the proximal section has generally the same pitching behavior as the distal section even though the two sections have a phase difference and also different magnitudes of inertial effect. The torque and power needs of both sections add up to the required input at the wing root. Therefore, the inertial effect due to wing translation drives most of pitch reversal, and a reaction torque is needed to prevent excessive pitching. In addition, positive power input is needed during mid-downstroke and early pronation to facilitate pitching. This positive power can only be provided by muscle activity, and it is indeed achievable by the shoulder muscles of the hummingbird (Hedrick et al., 2012).

To confirm that the current two-section model is sufficient to analyze the pitching dynamics of the hummingbird wing, we also created a three-section model by further splitting the proximal section into two parts connected at the wrist. This alternative model takes into account of wing twist at the wrist joint (Hedrick et al., 2012). The same procedure is used to calculate the inertial torque components, the aerodynamic torque, and the torques at wing junctions. The results show that the torque and power

inputs at the root are close to those obtained from the two-section model. In addition, the torque and power at the wrist joint are between those at the root and those at the finger junction. Therefore, we do not further discuss these results.

5.5 Conclusion

A computational model has been developed to analyze the pitching dynamics of the ruby-throated hummingbird and to identify the mechanism of wing pitching in hovering flight. Realistic wing kinematics reconstructed from high-speed videos are incorporated into the model, and the aerodynamic effect from a previous three-dimensional simulation is included. It is shown that pitch reversal of the hummingbird is mostly driven by the inertial effect of wing translational acceleration/deceleration. However, actuation power from the wing root is needed in the beginning of pronation to start the fast reversal and also during mid-downstroke to pitch the wing. The intrinsic muscles of the hummingbird wing are not required to power pitching motion of the distal section. These findings provide a unified view into the pitching actuation in insects and hummingbirds and thus may be useful for the design of engineering flyers that attempt to mimic these animals.

CHAPTER VI

THREE-DIMENSIONAL SIMULATION FOR FAST FORWARD FLIGHT OF A *CALLIOPE* HUMMINGBIRD

6.1 Introduction

Comparing with hovering flight, the forward flight of hummingbirds and its fluid dynamics have been much less studied. Tobalske et al. (2007) performed comprehensive measurement of the flight kinematics of the rufous hummingbirds in the wind tunnel at speed from zero (hovering) to 12 m/s. The data they obtained include the body orientation angle, wingbeat frequency, wingbeat amplitude, stroke plane angle, wingtip trajectory, and time-dependent variables such as the wing chord angle and wing area, at different flight speeds. In general, as the flight speed increases, the birds aligned their bodies more parallel to the flow to reduce drag, and the stroke plane becomes more vertical, which is beneficial for thrust production. Based on their data, the advance ratio, J, defined as the ratio between the flight speed, U, and the average wingtip speed, U_{tip}, is between $J = 0$ for hovering and $J = 1.5$ for the maximum speed at 12 m/s. In comparison, insects typically have an advance ratio of $J < 1$ (Vogel, 1966; Dudley, 2002). For example, fruit flies and bumble bees have the advance ratio at 0.25 and 0.6, respectively (Dudley and Ellington, 1990a; Dudley, 2002). So their wing speed is much faster than the flight speed. Such a difference in the flight dynamics implies that there should exist a significantly different force production mechanism in the hummingbird

wings than that of those insect wings.

Among the animal flyers, there are several types of thrust production mechanism for the forward flight mode. One common type is the so-called 'backward flick' (Hedenström and Johansson, 2015), which is used by many insects, e.g., bumble bees (Dudley and Ellington, 1990a,b; Dudley, 2002) and also by bats during slow flight with $J < 1$ (Norberg, 1976). In this type, the stroke plane tilts forward and the backward speed of the wing during upstroke is faster than the flight speed. Thus, the aerodynamic lift generated by the wings is directed forward during upstroke and functions as thrust. Another type is the paddling mode discovered in a recent study of fruit flies at speed of 0.43 m/s (Ristroph et al., 2011) (the advance ratio of fruit flies is near $J = 0.25$ (Dudley, 2002)). In this case, the stroke plane of the insects remains nearly horizontal, and the angle of attack of the wings at upstroke is much greater than that at downstroke. Thus, large drag is produced in the forward direction as a drag-based thrust mechanism. For large birds at cruising flight, the advance ratio is usually above one (Pennycuick, 1990), and thrust is typically generated during downstroke when the leading edge tilts downward to redirect the aerodynamic lift forward for simultaneous weight support and thrust production (Alexander, 2004). During upstroke, the birds feather their wings by tilting the leading edge upward into the effective wing direction so that a minimum amount of forces is produced (Alexander, 2004; Tobalske et al., 2003a; Spedding et al., 2003; Henningsson et al., 2008). Since the advance ratio of hummingbirds varies from zero to above one, it is possible that they use disparate force production mechanisms at different flight speeds. From Tobalske et al. (2007), the tip trajectory of the hummingbirds at

slow flight speeds is highly skewed, when viewed from a global coordinate system, and resembles that of insects. Thus, the backward flick mode is likely employed for thrust production. However, at fast speeds, it is not clear whether the hummingbirds become more like other birds, or they adopt a different flight strategy. To answer this question, it is necessary to examine the detailed wing motion at those speeds. In addition to the kinematic analysis, accurate calculation of the forces is needed, as the flow under consideration is highly three-dimensional and involves unsteady effects beyond limitation of quasi-steady models.

In the current study, we aim to understand the lift and thrust production of hummingbirds during fast forward flight. The flow field and behavior of vortices will be investigated along the aerodynamic forces. In addition, we will compare the force generation mechanisms between hummingbirds and other animals such as insects and large birds. Following the approach in a previous study of hovering flight of the hummingbird (Song et al., 2014), we develop a high-fidelity computational model that incorporates the realistic kinematics of the bird wings and adopt three-dimensional numerical simulations to resolve the unsteady flow.

6.2 Model configuration and simulation approach

6.2.1 Reconstruction of the wing kinematics

A calliope hummingbird (*Selasphorus calliope*) was used as the subject in this study, whose basic morphological data are provided in Tab. 6.1). The experimental study was

conducted to obtain the wing kinematics at a sustained flight speed of U_∞ = 8.3 m/s, at which the wingbeat frequency is 45.5 Hz while the stroke plane angle between the stroke plane and the horizontal is 67.9° (see Tab. 6.1). In the experiment, the bird was placed in the wind tunnel with a feeder at the middle of the wind tunnel, and it was trained to adapt to the wind while feeding. Three synchronized high-speed cameras were deployed around the tunnel section to film the bird flight (see Fig. 6.1).

We recorded flight kinematics of the hummingbird using three high-speed cameras distributed outside the working section of a wind tunnel: one Photron SA-3 (Photron USA Inc., San Diego, CA, USA) and two two Photron 1024 PCI, electronically synchronized to shutter as driven using Photron Fastcam Viewer software and synchronized to frame using a transistor-transistor logic (TTL)-pulse. Two cameras were placed dorsally to the bird, and one was placed laterally. Video recordings were made at 1000 Hz with a shutter speed of 1/10,000 s. The bird flew in an open-circuit, variable-speed wind tunnel, the properties of which have been described previously (Tobalske et al., 2005). The working section of the tunnel is 85 cm in length, square in cross section, 60×60 cm at the inlet and increasing to 61.5×61.5 cm at the outlet to accommodate boundary-layer thickening. Maximum deviations in velocity within a cross section are less than 10% of the mean. The boundary layer is less than 1 cm thick and turbulence is 1.2%.

After the videos were taken, a custom MATLAB program (Hedrick, 2008) was used to track the markers frame by frame and to extract their three-dimensional coordinates. These markers were pre-labeled on the wings using non-toxic paint, and they included

Parameter	Value
Mass	M = 2.8 g
Stroke plane angle	β = 67.9°
Stroke amplitude	Φ = 102.5°
Wingbeat frequency	f = 45.5 Hz
Wing length	R = 4.51 cm
Single wing area	S = 5.18 cm^2

Table 6.1: Morphological data of the hummingbird used in the study.

five points on the leading edge, on at the wingtip and three on the trailing edge, as seen in Fig. 6.2.

Details of the wing geometry reconstruction process is similar to those in the previous hovering hummingbird study (Song et al., 2014). That is, the wing profile was constructed using spline interpolation through the marker points, and the wing surface was then built using triangular elements within the profile. The bird body was reconstructed nominally based on the camera views of the hummingbird. In the current reconstruction, a single wing consists of 1335 elements and 718 nodes, while the body surface consists of 3560 elements and 1782 nodes. A total of 13 cycles of wingbeats during steady flight were captured, and each cycle contains approximated 22 frames. To increase the time resolution of the wing position, the trajectories of the wing mesh nodes are also refined by spline interpolation in time. Seven cycles of wingbeats were reconstructed from the imaging data and used for the simulation. Figure 6.3(a,b) shows a sequence of wing positions within a cycle.

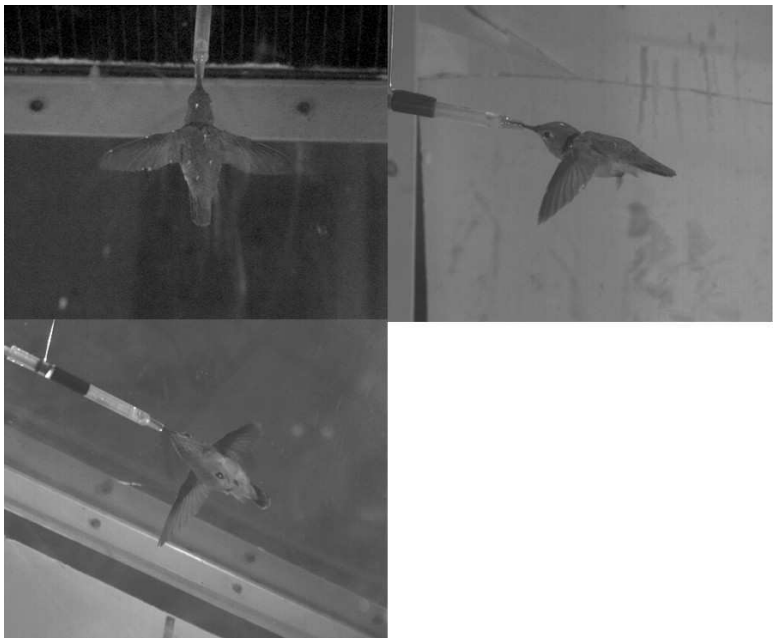

Figure 6.1: Camera views of the hummingbird in the wind tunnel.

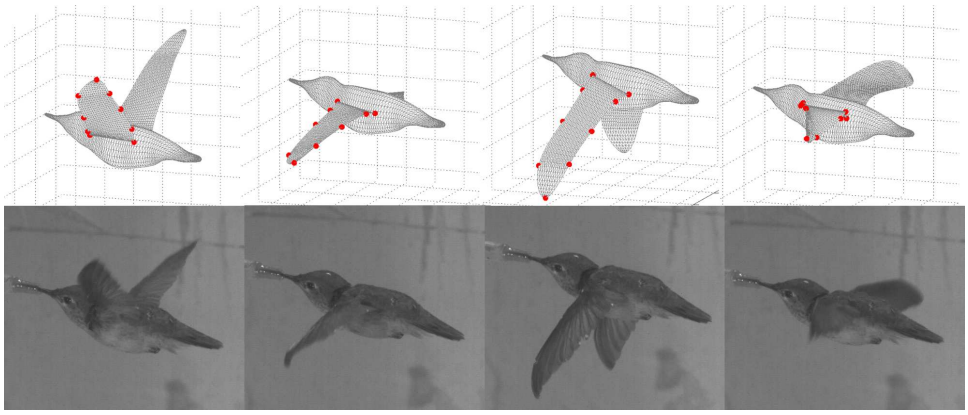

Figure 6.2: Reconstructed bird model and corresponding snapshots from the camera view.

6.2.2 Wing kinematics

Figure 6.4 shows both the instantaneous and phase-averaged wingtip velocity of the hummingbird. It can be seen that upstroke has slightly higher velocity than downstroke. The peak value is at 11.22 m/s for downstroke and 12.18 m/s for upstroke. The wingtip

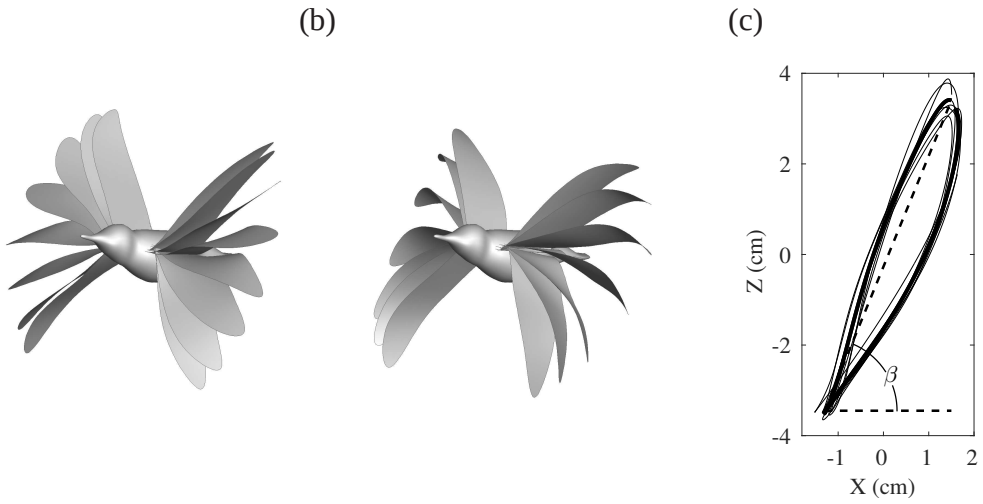

Figure 6.3: Reconstructed wing position of the hummingbird within one beat cycle: (a) downstroke, (b) upstroke, and (c) the wingtip trajectory as viewed in a body-fixed coordinate system, where the thick line is the cycle-averaged trajectory and thin is the instantaneous trajectory.

velocity averaged throughout the cycles is 8.14 m/s, which gives the advance ratio $J = 1.02$. The wing area can be calculated from the reconstructed kinematics and it varies between 5.34 cm^2 during downstroke and 5.03 cm^2 during upstroke. The average area is $S = 5.18$ cm^2.

From Fig. 6.3(a,b), wing twist along the axis and spanwise bending in a cycle are evident. To characterize the position of a cross section of the wings, we define the chord angle ψ as the instantaneous angle between the chord and the flight direction. The angle of attack, α, is defined as the angle between the chord and the relative flow direction that combines both the freestream velocity and the translational velocity of the chord at the leading edge. These two angles are plotted in Fig. 6.5 for two chords and five cycles, one proximal chord at dimensionless location $\hat{r} = r/R = 0.15$ and one distal chord at $\hat{r} = 0.9$, which are denoted by subscripts p and d, respectively.

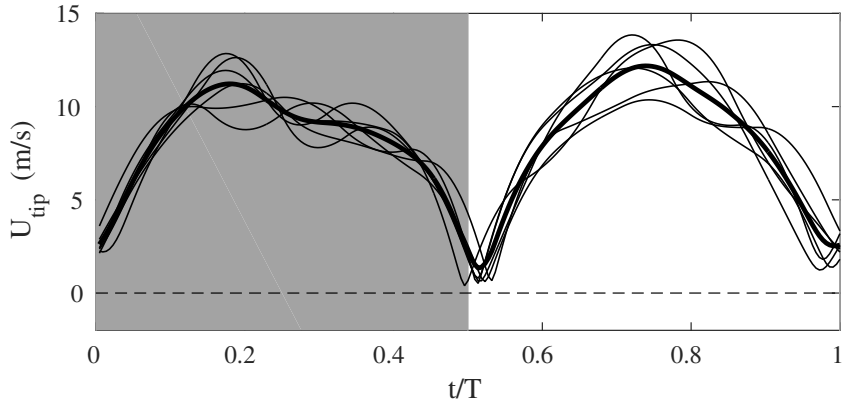

Figure 6.4: Instantaneous wingtip velocity.

From these plots, we can see large differences between the proximal chord and distal chord. For the proximal chord, the chord angle ψ_p and angle of attack α_p are both positive during the entire cycle. For the distal chord, these angles change the sign and vary significantly. During the downstroke, ψ_d is negative, i.e., the leading edge tilting downward, but α_d is positive due to fast translation of the chord. During upstroke, ψ_d is positive, i.e., the leading edge tilting upward, but the α_d is negative, indicating that the pressure surface and the suction surface are swapped at that moment. The wing twist can be described by the difference between the two chord angles, $\psi_d - \psi_p$, which is plotted in Fig. 6.6. It is shown that the twist angle reaches its extreme value during mid-downstroke and mid-upstroke; however, it is more pronounced during upstroke (near 40°) than during downstroke (near 25°). These differences between the proximal section and the distal section lead to highly nonuniform pressure distribution on the wing surface as shown later.

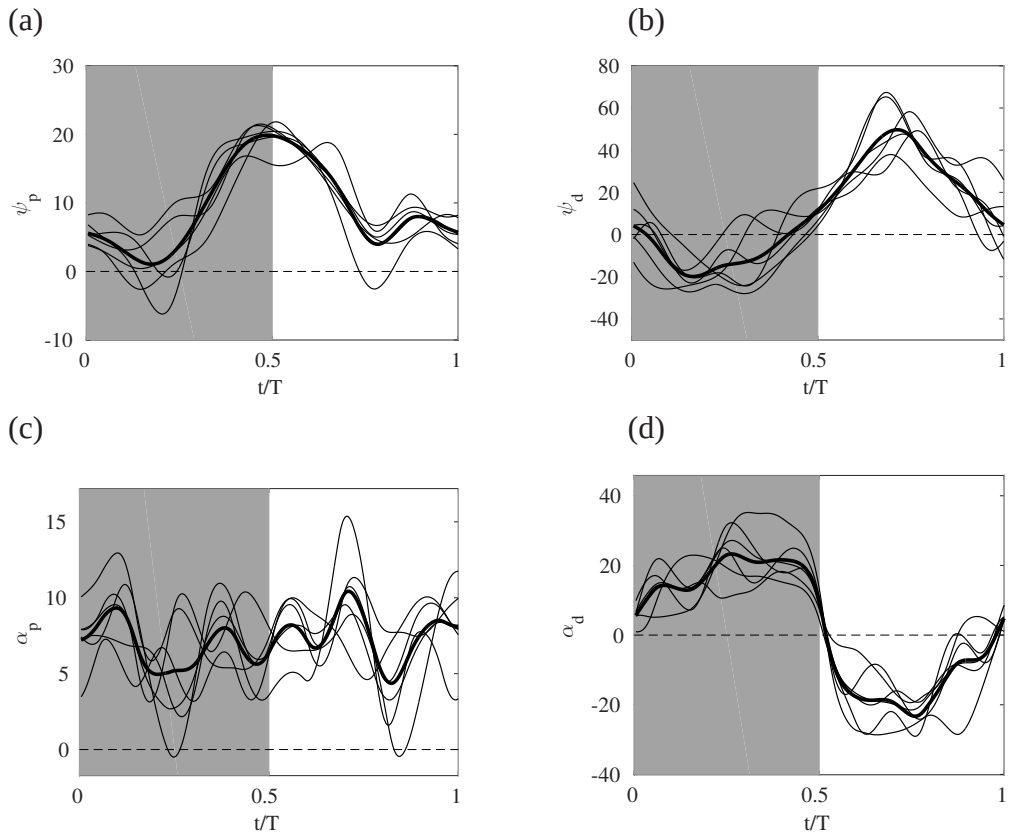

Figure 6.5: The chord angle ψ (a,b) and effective angle of attack α (c,d) for a proximal chord at $\hat{r} = 0.15$ (a,c) and a distal chord at $\hat{r} = 0.90$ (b,d).

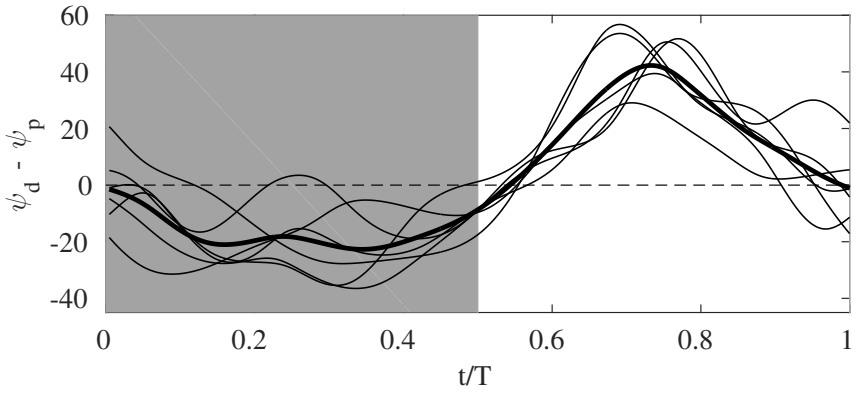

Figure 6.6: Wing twist as measured using the difference between two chord angles.

6.2.3 Simulation setup and verification

In the model, the Reynolds number, defined as $U_\infty \bar{c}/\nu$, is set to be $Re = 3000$. The flow is assumed to be governed by the viscous incompressible Navier-Stokes equation,

which is solved by an in-house code that adopts a second-order immersed-boundary finite-difference method. The code is able to handle large displacement of the moving boundaries (Luo et al., 2012). A fixed, nonuniform, single-block Cartesian grid is employed to discretize the domain (see Fig. 6.7(a)). The rectangular domain is $25\times20\times16$ cm^3. For the simulation,704×842×560 (333 million) points are used for the baseline simulation. A finer mesh is also used in the simulation to verify grid convergence. Both of these meshes have maximum resolution around the wing, which is $1/60$ cm in all three directions for the baseline case and $1/70$ cm for the refined case. The simulation was run in parallel using domain decomposition and Message Passing Interface (MPI). The time step is $\Delta t = 5\,\mu s$, which leads to approximately 4400 steps per wingbeat cycle. A multigrid method was employed to accelerate convergence of the Poisson solver. A total of 96 processor cores were used for the baseline case, and 128 cores for the refined case.

The simulation results for two wingbeat cycles from both meshes are shown in Fig. 6.7 and Tab. 6.2 for comparison. In Fig. 6.7 and also other figures from herein, the shaded area indicates downstroke, while the white area indicates upstroke. These results include the time-averaged lift and thrust of one wing and also lift and drag of the bird body. From the table, we see that the maximum difference of all the forces is less than 5%. Thus the baseline resolution is deemed satisfactory for the current study.

(a)

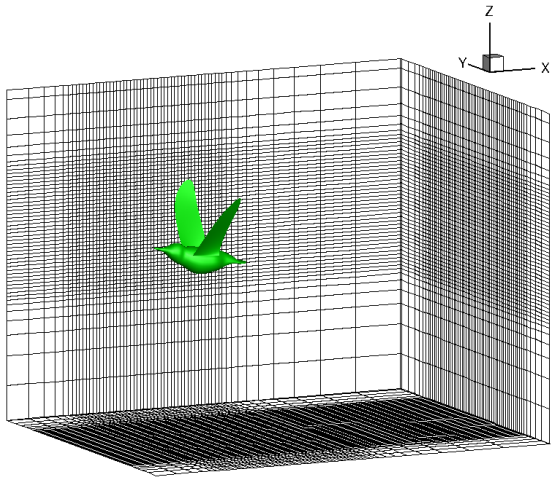

(b)

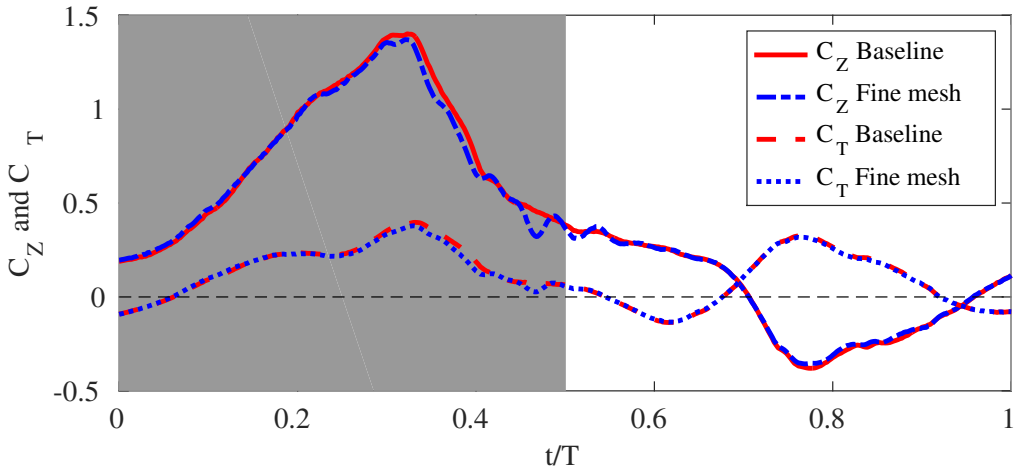

Figure 6.7: (a) The baseline mesh around the bird (only one out of every 10 points in each direction is shown). (b) The force comparison between the baseline simulation and fine mesh simulation.

6.3 Results

6.3.1 Aerodynamic forces

The vertical force F_Z and thrust $F_T = -F_X$ generated by one wing are normalized by the fluid density, ρ, the flight speed, U_∞ and the surface area of the wing according

	C_Z	C_T	$C_{Z,b}$	$C_{D,b}$
Baseline (333 million)	0.374	0.112	0.239	0.151
Fine mesh	0.381	0.117	0.238	0.150
Difference	1.84%	4.27%	0.42%	0.67%

Table 6.2: The comparison of the forces on both wing and body (unit: mN) from the two different meshes.

to

$$C_Z = \frac{F_Z}{(1/2)\rho U_\infty^2 S}, \qquad C_T = \frac{F_T}{(1/2)\rho U_\infty^2 S}. \tag{6.1}$$

The lift and drag on the bird body, F_{Z_b} and F_{D_b}, are normalized in the same manner. The aerodynamic power coefficient of one wing is defined as

$$C_P = \frac{\int \mathbf{f} \cdot \mathbf{u} \, \mathrm{d}A}{(1/2)\rho U_\infty^3 S}. \tag{6.2}$$

where $\mathbf{f}$ is the stress on the wing surface, and $\mathbf{u}$ is the velocity of a point on the wing in the body-fixed coordinate system.

These force and power coefficients are shown in Fig. 6.8, which include both instantaneous and phase-averaged data. The cycle averaged data are listed in Tab. 6.3 for both an entire cycle and downstroke/upstroke separately. A few observations are made from these data. First, Fig.6.8(a) shows that the weight support is mostly generated during downstroke where C_Z is positive. The mid-downstroke corresponds to the maximum lift production, as expected. During supination and early upstroke, the wings are still able to generate some lift. Around mid-upstroke, vertical lift becomes negative even though its amplitude is not particularly high. On the other hand, it is interesting to note that from Fig. 6.8(b), thrust is mostly positive during both downstroke and upstroke. Fur-

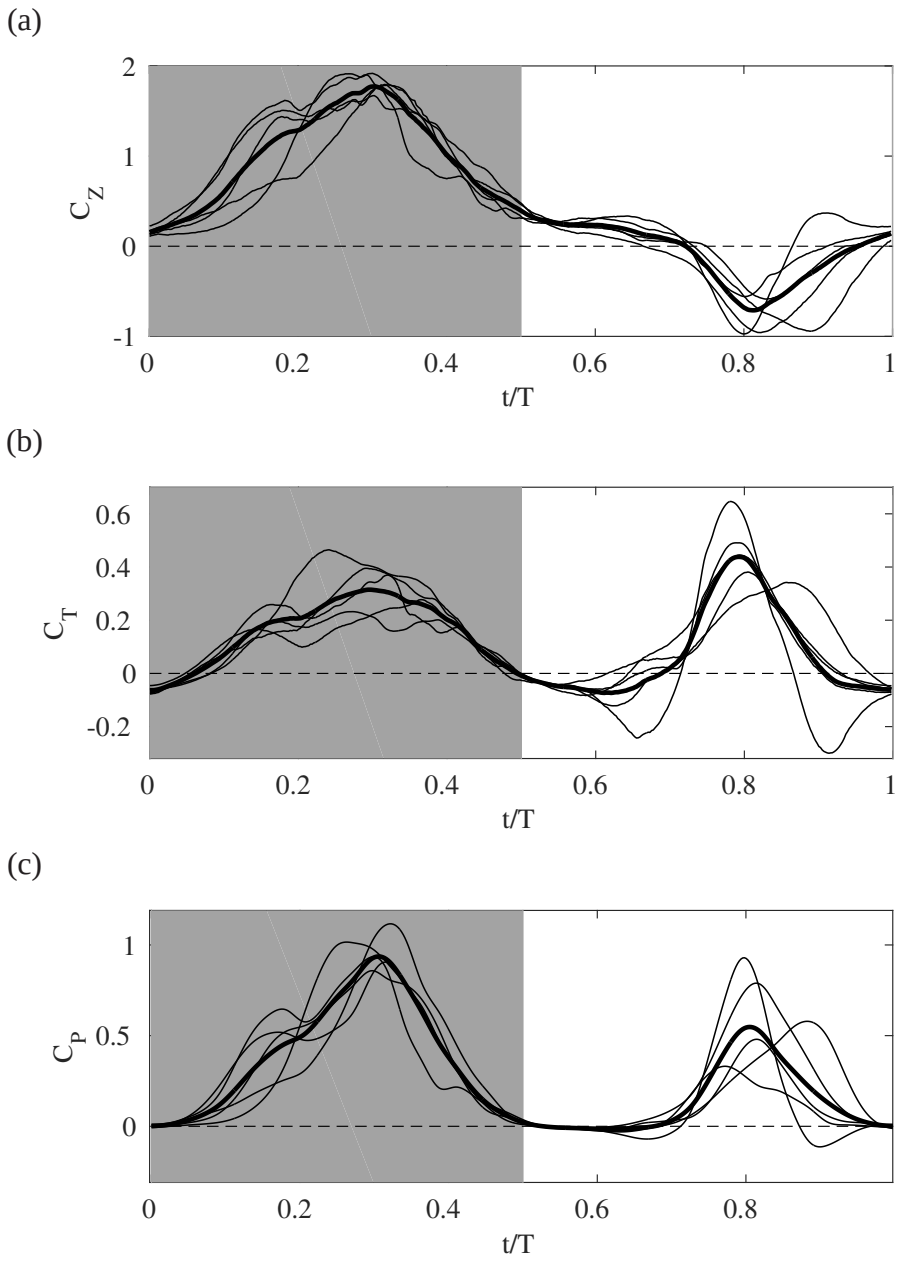

Figure 6.8: The force production and aerodynamic power consumption of each hummingbird wing: (a) vertical force coefficient, (b) thrust coefficient, and (c) power coefficient. In each case, the thin lines are the instantaneous data, and the thick line is the phase-averaged data.

thermore, thrust has a greater peak during upstroke than during downstroke. However, the data in Tab. 6.3 shows downstroke on average produces more thrust.

Fig. 6.8(c) shows that the power consumption during both half wingbeats are signif-

icant. However, the power requirement is greater for downstroke and is about twice as high as upstroke. This feature is similar to the hovering situation, where the downstroke power is nearly 2.8 times of the upstroke power according to Song et al. (2014), who studied the ruby-throated hummingbird.

Using dimensional variables, we found that the overall power consumption is 29 W/kg (per body mass), which is lower than that of the hovering ruby-throated hummingbird at 55 W/kg (Song et al., 2014).This is consistent with a U-shaped curve describing variation in mechanical power output according to flight speed (Pennycuick, 1968; Sun and Wu, 2003; Tobalske et al., 2003b). The current data for hummingbird is within the range reported for larger bird species. Cockatiel power output ranges from 17 W/kg (5 m/s) to 47 W/kg (14 m/s), and the dove power output ranges from 31 W/kg (7 m/s) to 54 W/kg (17 m/s) (Tobalske et al., 2003b).

In addition, using the present force coefficients, we obtain the total vertical lift produced by the bird, which, including the forces from both the wings and body, is around 96% of the bird weight. The bird body itself generates about 22.2% of body weight. This result will be discussed later. The thrust generated on the two wings together is 152% of the body drag. This imbalance of the horizontal forces may have been caused by the beak-feeder interaction as the bird was attempting to feed on the feeder.

	C_Z	C_T	C_P	$C_{Z,b}$	$C_{D,b}$
Whole cycle	0.466	0.115	0.266	0.266	0.151
Downstroke	1.006	0.157	0.394	0.342	0.157
Upstroke	-0.074	0.073	0.137	0.189	0.146
Ratio	-	2.15	2.88	1.81	1.08

Table 6.3: Averaged vertical force coefficient, C_Z, thrust coefficient, C_T, and power coefficient, C_P of the wings, and averaged lift and drag coefficients of the body, $C_{Z,b}$ and $C_{D,b}$.

6.3.2 Force production mechanism

Overall force production of the hummingbird can be explained from the wing kinematics as viewed from the global coordinate system, i.e., the coordinate system fixed with the ambient air. Fig. 6.13 shows the proximal and distal chord moving in the global coordinate system with their trajectories traced out. During downstroke, the angle of attack is positive for both the proximal chord and the distal chord. Therefore, both wing sections generate vertical lift. Since the leading edge of the distal section tilts downward, the aerodynamic lift has a forward component that leads to thrust generation during downstroke.

During upstroke, both wing sections move forward in air, even though the stroke plane angle is less than 90° and the wings move backward with respect to the body. Nevertheless, positive thrust is generated during this half cycle by the distal section. As shown in Fig. 6.13(b), the angle of attack is negative, and the overall force on the section points downward and forward.

Fig. 6.10 shows the pressure distribution within four selected vertical slices at mid-downstroke and mid-upstroke. It can be seen that the roles of the distal section and

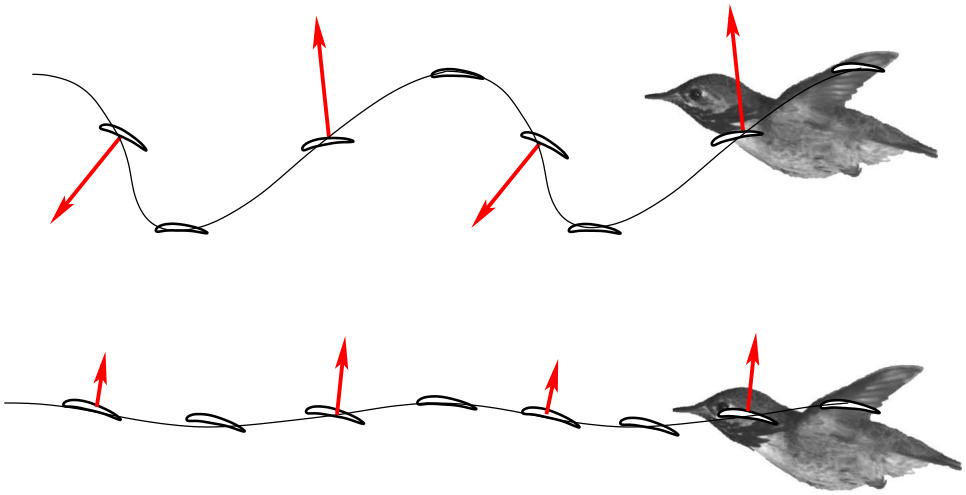

Figure 6.9: Time-dependent position of the distal chord (upper panel) and distal chord (lower panel) in the global coordinate system with qualitative force production at mid-downstroke and mid-upstroke.

proximal section are different. For both downstroke and upstroke, the proximal wing has pressure surface on the ventral side and suction surface on the dorsal side. Thus, its main role is for vertical lift generation. However, the distal wing flips its angle of attack between the two half cycles. Thus, positive (negative) pressure is distributed on the ventral (dorsal) side during downstroke, and the opposite is true during upstroke. This pressure differential leads to vertical lift production during downstroke only, but thrust production during both downstroke and upstroke.

6.3.3 Vortex structures

Vortex structures, which are induced by the wing motion and dominate the wake, have been a focal point in the study of force production of flapping wings and fish fins. They can also be used to evaluate whether a bird adopts slow gait or fast gait (Alexander, 2004). As has been pointed out by previous researchers, at slow gait the trailing-edge

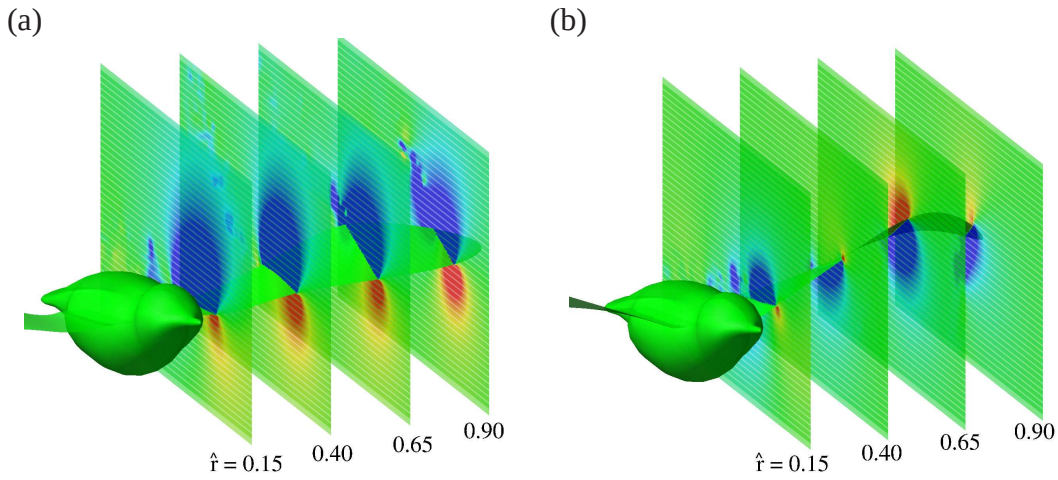

Figure 6.10: Pressure distribution in the flow in the vertical planes at (a) mid-downstroke and (b) mid-upstroke.

vortices (TEVs) form rings after each downstroke, and the sequence would look like a series of smoke rings (Spedding et al., 1984; Spedding, 1986); while at fast gait, the tip vortices (TVs) form undulating vortex tubes from the tip, and the TEVs form cylinders from the trailing edges, both being convected downstream (Spedding, 1987; Spedding et al., 2003; Henningsson et al., 2008).

In the current study of hummingbird flight, we used the iso-surface to show the vortex structures. The scalar quantity is defined as the maximum value of the imaginary part of the eigenvalue of the velocity gradient tensor, $\nabla\mathbf{u}$, and it describes the strength of the local rotation of fluid (Mittal and Balachandar, 1995b). It is found that the TVs are continuously shed from the wingtip, and the TEVs shed with the shape of separate cylinders. Such characteristics of the vortex structures confirm the speculation in a previous study of hummingbirds (Pennycuick, 1988), which argues that the hummingbird wings would generate a ladder-like vortex wake. Several snapshots of the flow field are shown in Fig. 6.11. These snapshots show roughly the shape of the TVs that follow

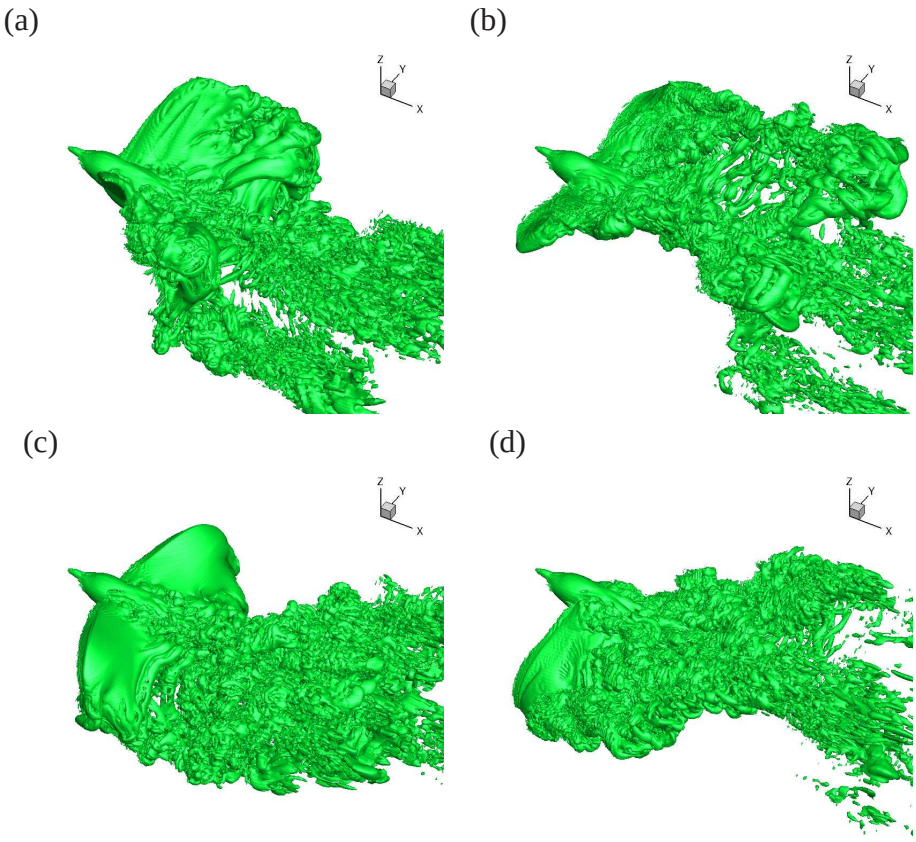

Figure 6.11: Vortex structures in the flow: (a) pronation, (b) mid-downstroke, (c) supination, and (d) mid-upstroke.

the trajectory of the wingtips. In addition, vortex shedding from the trailing edge are evident. Formation of the LEVs during both downstroke and upstroke is visible, and the LEVs are stable for both downstroke and upstroke. From Fig. 6.5(d), the angle of attack of the distal section keeps a maximum value around 25° for a significant period of time, which may have caused LEV shedding and stall, if the wings simply translated without changing its pitch. However, since the wings are also performing rapid pitching around their axes, as seen from variation of the chord angle plotted in Fig. 6.5(b). That is, the chord angle magnitude decreases during downstroke after $t/T > 0.2$, and quickly increases during upstroke before mid-upstroke. Such rotational motion has been known to maintain stability of LEVs and to enhance lift production of the wings.

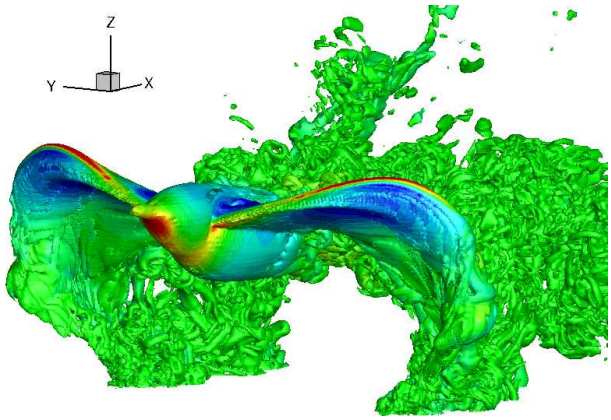

Figure 6.12: Vortex structures at mid-upstroke, where the color indicate the pressure level.

6.4 Discussion

6.4.1 Forces on the bird body

Lift and drag on the bird body are affected by the orientation of the bird during flight. In general, the inclination angle of the body decreases with the increase of flight speed (Tobalske and Dial, 1996; Tobalske et al., 1999, 2007, 2003a; Hedrick et al., 2004). In the current study, the body angle of the hummingbird is $\chi_b = 12^\circ$, which is close to the angle of the rufous hummingbird at speed of 8 m/s where $\chi_b = 11^\circ$ (Tobalske et al., 2007). Fig. 6.13 shows both the instantaneous and phase-averaged data of the forces on the body. Downstroke-, upstroke-, and cycle-averaged data are listed in Tab. 6.3. These results show that the lift on the body provides 22.2% of the weight support. In addition, lift during downstroke is 1.81 times of lift during upstroke. In Fig. 6.13(a), lift on the body oscillates significantly during a wingbeat cycle. On the other hand, drag on the body does not vary very much in a cycle and is nearly equal on average between downstroke and upstroke, which are reflected in Fig. 6.13(b) and

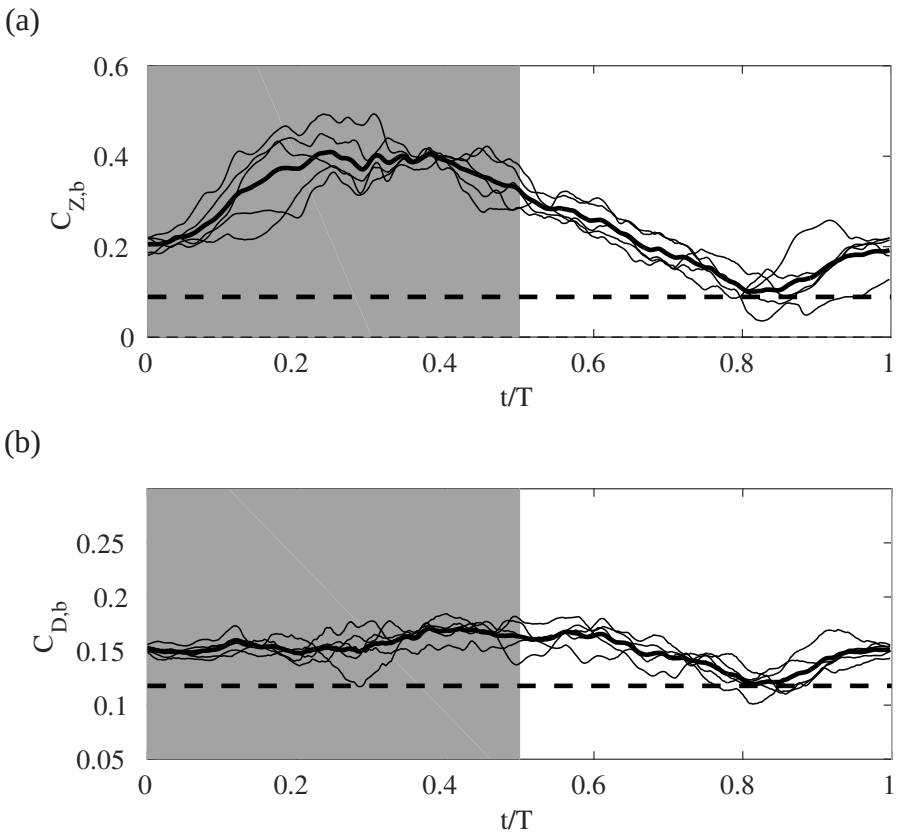

Figure 6.13: The instantaneous (thin lines) and phase-averaged (thick line) lift (a) and drag (b) on the bird body. The dashed lines denote the value from the isolated body simulation.

Tab. 6.3.

The high percentage of lift produced by the body and the oscillations of the body lift in a cycle may be attributed to aerodynamic interaction between the wings and the body that is assumed to be stationary in the current study. To verify this possibility, we also simulated separately the same flow around the isolated body without the wings attached. The shape and orientation of the body remain the same.

Fig. 6.14(a) shows the pressure distribution on the bird body from the isolated body simulation, which can be compared with the result from the full body simulation shown

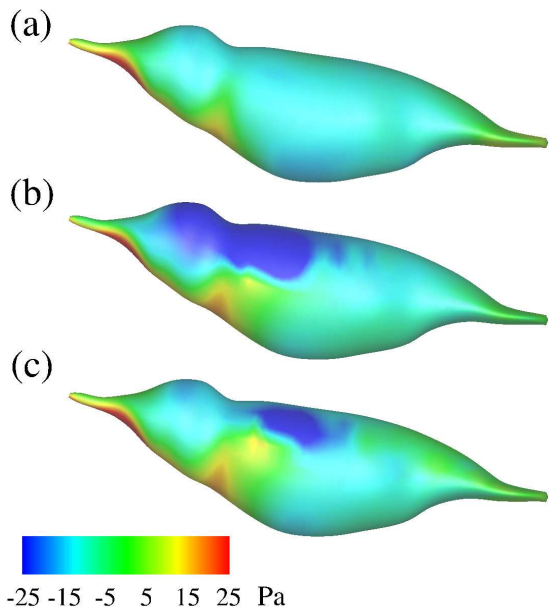

Figure 6.14: The pressure distribution on the bird body: (a) isolated body simulation, (b) full body simulation at mid-downstroke, (c) full-body simulation at mid-upstroke.

in Fig. 6.14(b,c) for mid-downstroke and mid-upstroke. For the isolated body, even though a high pressure zone is established below the body, the flow passes around the body in the absence of the wings and merges behind and above the body, where the pressure is partially recovered. As a result, the overall lift by the body is small. When the wings are present, the flow from below is prevented to pass around the body by the wings. Furthermore, the wing-wing interaction mechanism, as proposed by Lehmann et al. (2005), apparently has played a role here. That is, when the two wings are separating from one another from pronation to mid-downstroke, they create a low pressure zone above the bird body, as shown in Fig. 6.14(b), thus leading to a net upward force. This mechanism also explains why during upstroke, the low pressure zone above the body, as plotted in Fig. 6.14(c), is significantly smaller as compared with downstroke.

The present result shows that the bird body has significant contribution to the overall

Taxa	Speed (m/s)	Body angle χ	Lift(% of weight)
Hummingbird in flight	8.3	12°	22.2%
Hummingbird(body only)	8.3	12°	8.4%
Cockchafer beetle (Nachtigall, 1964)	2-2.5	40°	3%
Dipteran (Wood, 1970)	2	10°	4%
Noctuid moth (Chance, 1975)	4	26°	10%
Bumblebee (Dudley and Ellington, 1990a)	5	15°	8%
Zebra finch (Csicsáky, 1977)	4-5	25°	15%
Zebra finch (Tobalske et al., 2010)	6-10	15°	20±5%

Table 6.4: Lift contribution from the body toe weight support for different species. The measurement of the insects was done on isolated bodies and the data for zebra finch was done using live birds with intact but folded wings and tails.

weight support. In comparison, previous experimental studies of insects and other birds indicated that the body lift is only a small portion of the animal weight, as shown in Tab. 6.4. However, we point out that in those previous studies, the force was measured for the isolated animal body only, while in the current study, the wings are present and are in constant motion. For the isolated hummingbird body, we also observed low lift production. As shown in Tab. 6.4, the lift of the isolated hummingbird body is only 8% of the weight and is comparable with previous data for insects and also birds (e.g., zibra finch).

Drag coefficients of insect bodies range from 0.12 to 0.95, depends on flow conditions and taxonomic identity of the body (Dudley and Ellington, 1990b). In the current study, the average drag coefficient of the bird body from the full body simulation would be 0.43 if scaled by the frontal area and is thus on the lower end as compared with insects.

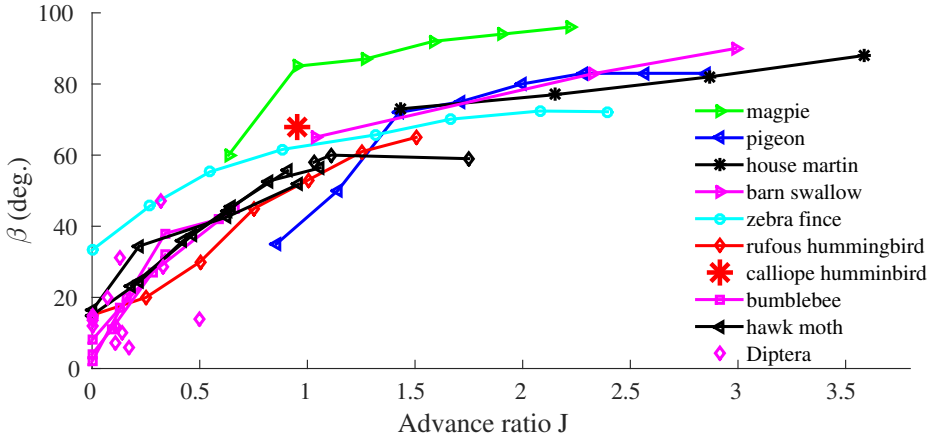

Figure 6.15: (a) Stroke plane angle vs. advance ratio. Data are collected from literature (*Diptera*, Ennos (1989b); Bumblebee, Dudley and Ellington (1990a,b); *rufous* hummingbird, Tobalske et al. (2007); Magpie, Tobalske and Dial (1996); Pigeon, Pennycuick (1968); Hawk moth, Willmott and Ellington (1997); Zebra finch, Park et al. (2001)).

6.4.2 Comparison of hummingbirds, insects and other birds

The advance ratio J and stroke plane angle β are two primary factors that affect the force production of flapping wings during forward flight. These two variables differ largely among animal species. Fig. 6.15 shows a few species on the $\beta - J$ map with the data directly collected or derived from various sources. It can be seen that hummingbirds largely fall within the range of the insects but also extend into the range of other birds. For all species, the stroke plane angle increases with the advance ratio, which is expected since at fast flight speed, the animals not only reduce the body angle, which would naturally cause the stroke plane angle to increase, for drag reduction but also tilt the stroke plane more to enhance thrust generation.

For the small insects like the bumblebee and fruitfly, the advance ratio is usually less than one (Dudley, 2002). For such slow flight, lift production is predominant over

thrust production. Since the back-sweeping velocity of the distal wing exceeds the forward flight speed at upstroke (Dudley and Ellington, 1990a; Ristroph et al., 2011; Sun and Wu, 2003), the wingtip trajectory traced out in the global coordinate system is highly backward skewed at upstroke, which is shown in Fig. 6.16 for a bumblebee at $J = 0.6$. In this case, downstroke is mainly for lift production, while upstroke is mainly for thrust production. If the flight speed is further reduced, with a more skewed trajectory, upstroke may even produce lift as well. Overall, this strategy of using upstroke is also known as 'backward-flick' (Norberg, 1976; Tobalske et al., 2003a,b). The force production mechanism is further illustrated in Fig.6.17(a). An exception is the fruitfly which is shown by a recent study that its upstroke uses a paddling mode to produce drag-based thrust (Ristroph et al., 2011).

For most of birds, the advance ratio is significantly greater than one, and the stroke plane angle is close to 90°. Thus, the wingtip trajectory in the global coordinate system become more sinusoidal, as seen in Fig. 6.16. In this case, upstroke is not suitable for thrust generation. Instead, the wings are either feathered or swept during upstroke with little force produced (Tobalske et al., 2010; Henningsson et al., 2008; Spedding et al., 2003), and a powerful downstroke is used to produce both lift and thrust. The velocity combination and force production of this case are shown in Fig.6.17(c).

For the hummingbird in the current study, the advance ratio is between that of insects and other birds. The wingtip trajectory is moderately skewed as seen in Fig. 6.16. Therefore, with proper angle of attack, the wings can still produce thrust during upstroke. However, since the overall force points downward, some lift has to be sacrificed.

The force production in this case is further shown in Fig. 6.17(b). From this figure it can be seen that thrust can be produced when the wing speed is comparable to or possibly even lower than the flight speed. This thrust mechanism is analogous to a sail that moves against wind and thus is termed a 'sail mode' in the present work. On the other hand, downstroke of the hummingbird is similar to that of big birds, as seen in Fig. 6.16, where both lift and thrust are generated.

It should be pointed out that at slow flight speeds, force production of the hummingbird is still very likely close to that of insects. As shown by Tobalske et al. (2007), when J is below 0.7, the stroke plane angle of the hummingbird is small and the wingtip trajectory is also highly skewed like that of insects. Similarly, some of insects can perform fast flight at $J > 1$, e.g., the hawkmoth, as seen from Fig. 6.15. It would be interesting to see whether their force production mechanism is similar to that described here for the hummingbird.

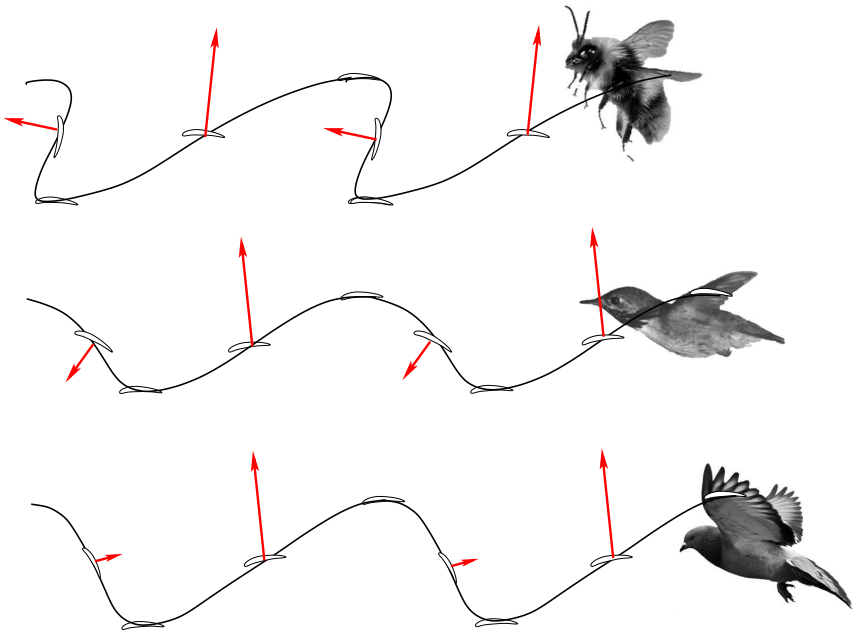

Figure 6.16: Wingtip trajectory and force production of the bumblebee, hummingbird, and big birds.

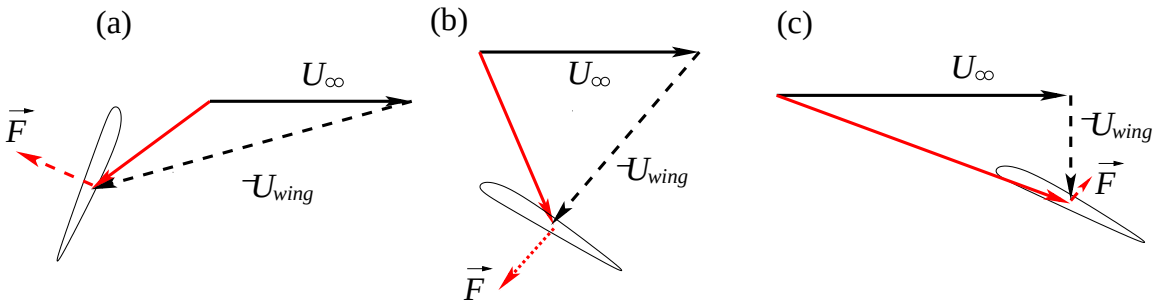

Figure 6.17: Force production of upstroke during forward flight. (a) Backward-flick by bumblebee, (b) sail mode by hummingbirds, (c) feathering mode by big birds.

CHAPTER VII

SUMMARY AND FUTURE WORK

7.1 Summary

In this thesis, we focus on the computational modeling of the aerodynamics of hummingbird flight to study the unsteady fluid dynamics and force production mechanisms of the bird. To capture details of the aerodynamics, we reconstructed the kinematic model with high-fidelity based on the high-speed videos provided by our collaborators. Using a direct simulation approach, we accurately obtained vortex-dominated flow field and the force histories. In conclusion, four specific aspects have been studied in this thesis:

First, a three-dimensional computational fluid dynamics simulation has been performed for a ruby-throated hummingbird (*Archilochus colubris*) in hovering flight. Realistic wing kinematics were adopted in the numerical model by reconstructing the wing motion from high-speed imaging data of the bird. Lift history and the three-dimensional flow pattern around the wing in full stroke cycles are captured in the simulation. Significant asymmetry is observed for lift production within a stroke cycle. In particular, downstroke generates about 2.5 times as much vertical force as upstroke, a result that confirms the estimate based on the measurement of the circulation in a previous experimental study. Associated with lift production is the similar power imbalance between

the two half strokes. Further analysis shows that in addition to the angle of attack, wing velocity and surface area, drag-based force and wing-wake interaction also contribute significantly to the lift asymmetry. Though the wing-wake interaction could be beneficial for lift enhancement, the isolated stroke simulation shows that this benefit is buried by other opposing effects, e.g., presence of down wash. The leading-edge vortex is stable during the downstroke but may shed during the upstroke. Finally, the full-body simulation result shows that the effects of wing-wing interaction and wing-body interaction are small.

Then, a quasi-steady model describing aerodynamics of hovering ruby-throated hummingbirds was developed to study extent of the low-order model in representing the complex flow physics and also to separately quantify the forces from the translational, rotational and acceleration effects. Realistic wing kinematics were adopted and the model was calibrated against CFD simulations of a corresponding revolving wing model. The results show that the quasi-steady model is able to predict overall lift production reasonably well but fails to capture detailed force oscillations. The downstroke-upstroke asymmetry is consistent with that in the previous CFD study. Further analysis shows that significant rotational force is produced during mid-stroke rather than wing reversal.

Third, a computational analysis of the pitching dynamics was performed by incorporating the realistic wing kinematics to determine the inertial effects. The aerodynamic effect was also included using the pressure data from a previous three-dimensional computational fluid dynamics simulation of a hovering hummingbird. The results show

that similar with many insects, pitch reversal of the hummingbird is, to a large degree, caused by the wing inertia. However, actuation power input at the root is needed in the beginning of pronation to initiate a fast pitch reversal and also in mid-downstroke to enable a nose-up pitching motion for lift enhancement. The muscles on the wing may not necessarily be activated for pitching of the distal section. Finally, power analysis of flapping motion shows that there is no requirement for substantial elastic energy storage or energy absorption at the shoulder joint.

Fourth, we have developed a high-fidelity computational fluid dynamics model to analyze the fast forward flight of a hummingbird, whose three-dimensional wing kinematics were incorporated into the model by extracting the wing position from high-speed videos. The advance ratio, or the ratio between the flight speed and the wing tip velocity, is around one, and we are particularly interested in how thrust is generated at this fast speed. Our simulation result has shown that both downstroke and upstroke produce significant amount of thrust for the bird to overcome drag. This feature likely sets the hummingbird apart from many of other flying animals such as insects and large birds.

7.2 Future study

Several future directions of study can be derived based on the current study. In particular, we have initiated a study on the aerodynamics of yaw turn of the hummingbird, using a similar methodology. The details and other directions are described as follows.

7.2.1 Unsteady maneuvers of hummingbirds

Other than hovering and forward flight, hummingbirds can obviously perform various fast maneuvers such as pitch, yaw, roll, and more complex maneuvers that are combinations of these. Different from engineering aircraft, whose maneuvers are usually slow and thus whose flight dynamics can be separated from the wing aerodynamics in a flight analysis, maneuvers of animals can be done very quickly, e.g., within one or two wingbeats (Hedrick et al., 2009). Therefore, during such maneuvers, the flight dynamics of the animal body is necessarily coupled with the aerodynamics of the flapping wings. In the current work, we use hummingbirds as an example to study the coupled flight dynamics and aerodynamics. As a first step, we are focusing on yaw turn only, and both the blade-element model and the complete CFD model will be used to analyze the forces generated by the wings.

The ruby-throated hummingbird, which has a body mass of 3.40 gram, was used as the subject in the experiment that was carried out at the University of North Carolina at Chapel Hill. Six high-speed cameras were used in the filming of the bird flight, two of which recording the X-ray images while the remaining four recording the regular images (See Fig. 7.1). The X-ray images were used to study the muscular and joint activities of the bird. For each wing, nine points were marked on the wing edges. The reconstruction process is the same as that of the hovering and cruising flight, which were described by previous chapters. In the current study, marker labels were also placed on the hummingbird body to trace the body orientation. To simplify the analysis, the bird body is assumed to be a rigid body, and extra motions of other parts such as the head and

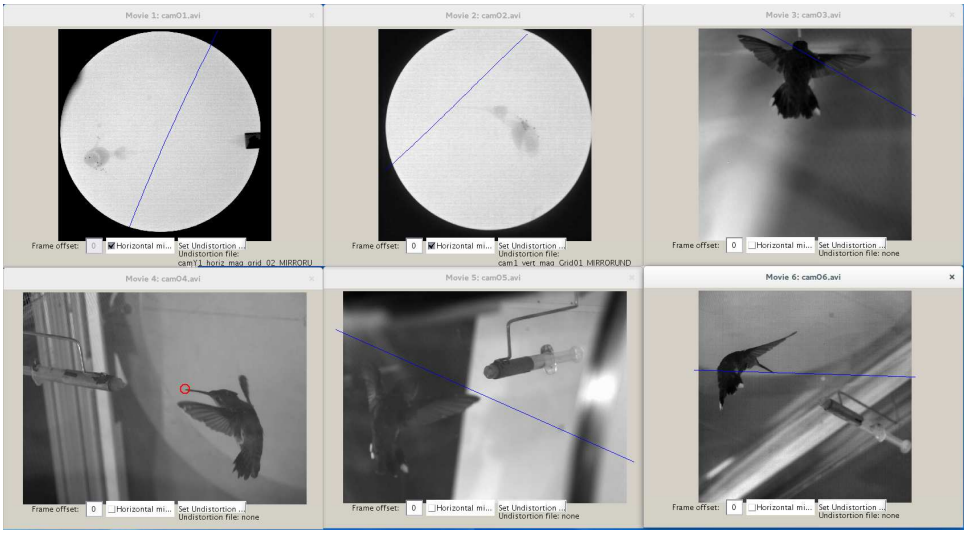

Figure 7.1: Camera view of the hummingbird performing a yaw turn. Two X-ray views are included.

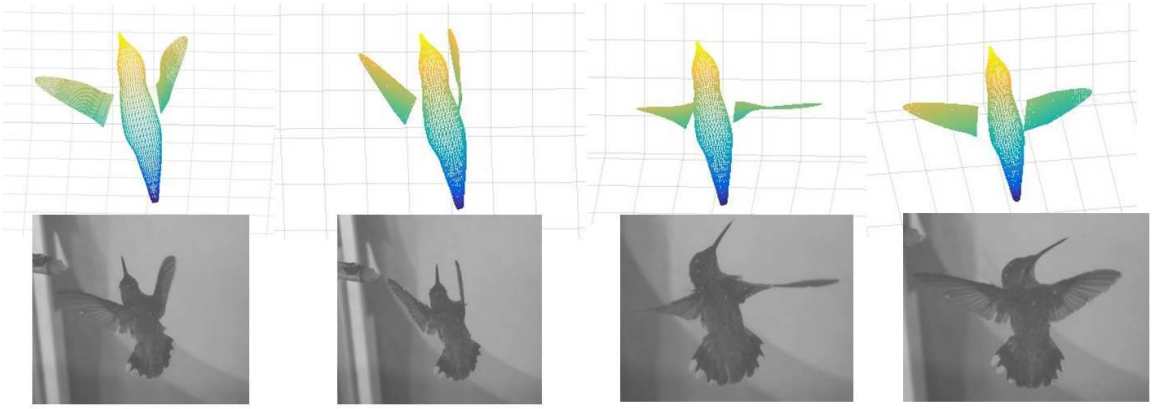

Figure 7.2: Comparison of four typical wing and body positions in one cycle between the reconsctructed model and original video images.

tail were not considered. Fig. 7.2 shows a comparison of four typical wing and body positions in one cycle between the reconstructed model and original video images. This figure shows that the reconstruction captures not only the instantaneous wing positions and deformations, but also the time-varying body orientation during the yaw turn.

Fig. 7.3 shows the tip trajectory of two wings in the top view. We can see that the

bird is initially hovering with the wings moving back and forth and the wingtips tracing the trajectory of nearly a circular arc. the circular arc. Later, the bird turns to the right. Fig. 7.4(a) shows the body yaw turning and pitching angle. From the yaw angle, we can get an more precise description of the bird motion: the bird was hovering in the first four wingbeat cycles and even turned slightly to the left; then it quickly turns to the right by 70° in next five cycles.

In Fig. 7.5(a), we show the comparison of the instantaneous tip velocity of two wings. The shaded region indicates the downstroke, while the white region indicates the upstroke. From the figure, we can see the left wing velocity is slightly larger than that on the right wing at both downstroke and upstroke. Fig. 7.5(b) shows the tip velocity difference between the left wing and right wing. We can see that the difference oscillates around zero at first 4 cycles. In the later cycles, the velocity of the left wing is significantly larger than that of the right wing at upstroke. To what extent this velocity difference makes in the yaw turning is not yet clear and will be studied in the future.

To see other differences in the wing kinematics, we plot the angle of attack for each wing at middle downstroke and upstroke in nine cycles, which is shown in Fig. 7.6(a). For each point, the value is obtained by the average of the 20% of the time period around middle downstroke and middle upstroke. Fig. 7.6(b) shows the angle of attack difference between downstroke and upstroke for both wings. This figure helps to estimate the average horizontal force production of each wing. From this figure, we found that the $\alpha_{down} - \alpha_{up}$ of the right wing is larger than that of the left wing, which implies that the right wing generates larger net torque for the right turning than the opposite torque

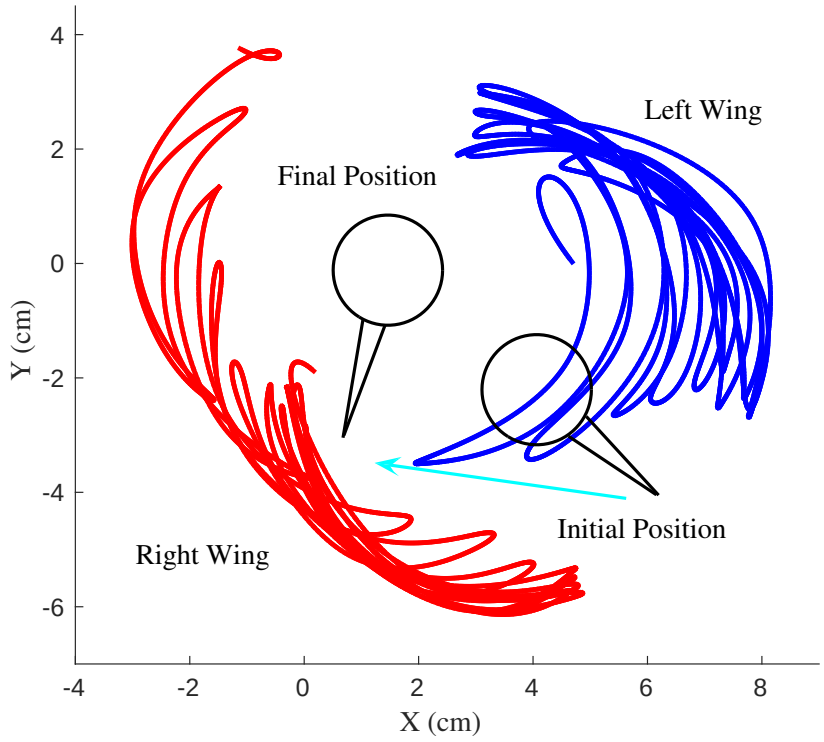

Figure 7.3: Top view of the wingtip trajectory and bird orientation during the yaw turn. The bird is turning clockwisely, or turning to its right.

generated by the left wing. The effect of this asymmetry in the angle of attack on the yaw turn will also be studied in the future.

7.2.2 Further comparison of hummingbirds and other flying animals

Nature is full of diversity. The physiology, biomechanics, and aerodynamics of hummingbird wings are quite different from those of insects, other birds, and bats. It is yet not clear which ones are optimal when it comes to engineering innovation of biomimetic MAVs with given design constraints. At certain point, a multi-disciplinary

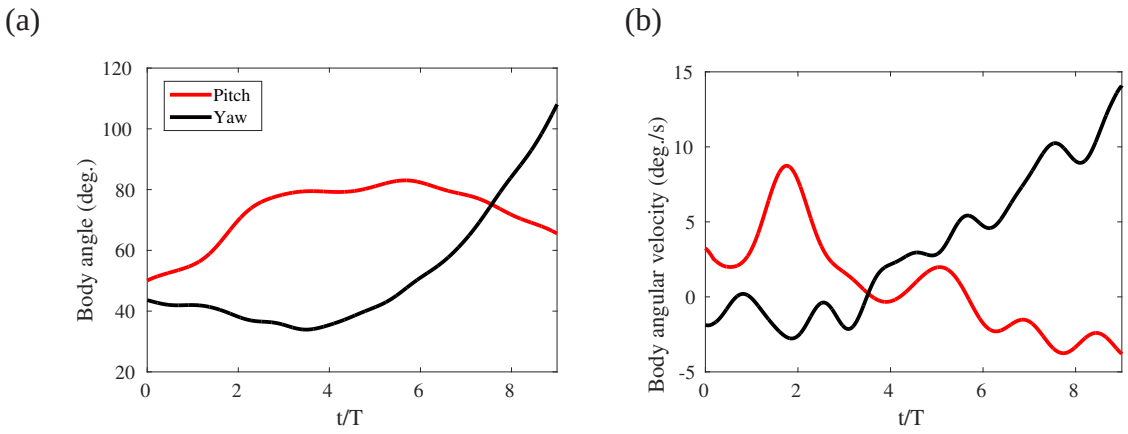

Figure 7.4: (a) Body pitch and yaw angles in nine wingbeats. (b) Corresponding angular velocities of pitch and yaw.

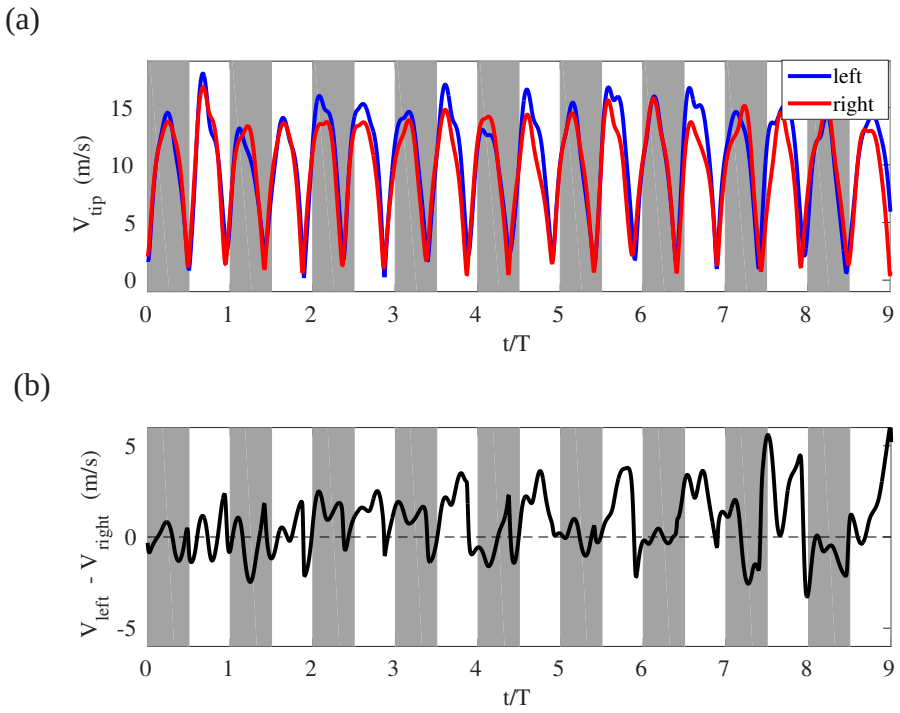

Figure 7.5: Tip velocity of two wings in nine cycle (a) and their difference (b).

optimization study would be required to optimize the wing structure and kinematics for such MAVs. Before such a study, however, it would be very helpful to perform a further investigation of hummingbird wings in comparison with other wings in terms of various morphological and kinematic parameters. Questions that may be addressed

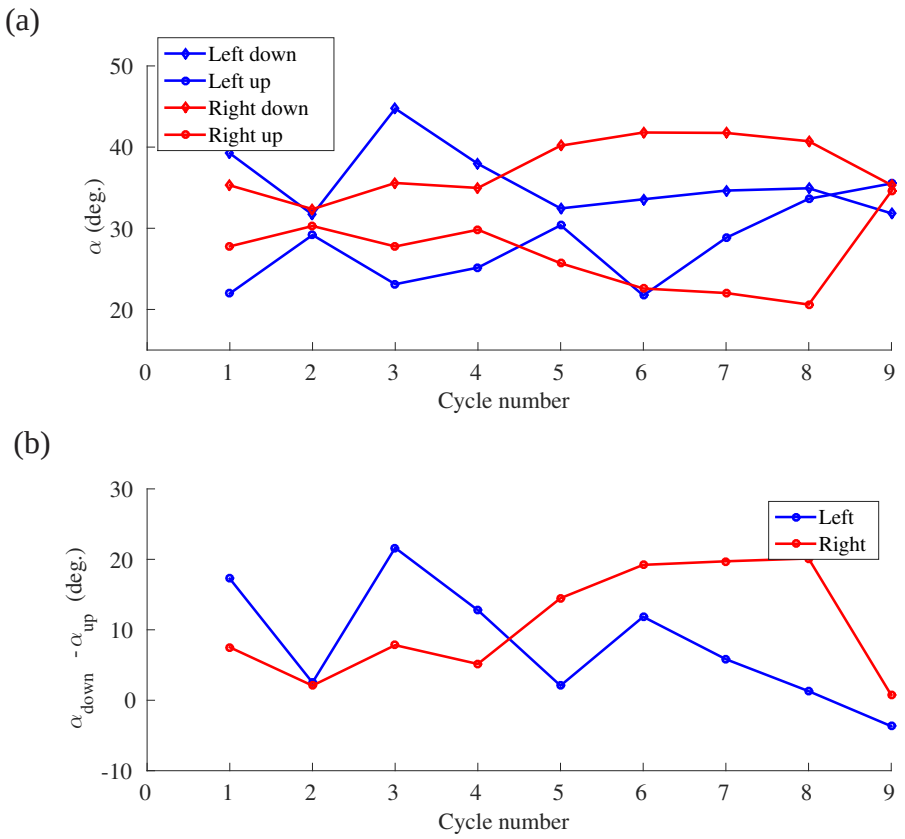

Figure 7.6: (a) Average angle of attack at middle downstroke and middle upstroke of the two wings (sampled from 20% of the period duration). (b) The angle of attack difference between downstroke and upstroke of the two wings.

include: Do these different wings have similar efficiency to provide necessary forces for the same flight regime? If yes, how is it achieved by the different wing designs? Or if not, which one is more efficient and why? We envision that the CFD approach utilized in the present work can be directly applied in such a study and will lead to insightful results.

7.2.3 Fluid-structure interaction of the elastic flapping wings

Due to the complicated elastic properties of the bird wings and challenges in coupling a fluid solver and a solid solver, few CFD studies have incorporated the fluid-

structure interaction (FSI). In the future, an FSI study can be pursued, and it will lead to insights into the important effect of the passive flexibility of the animal wings on their aerodynamic performance and will provide useful guidance on design of flexible structures of the biomimetic MAV wings.

List of publications and presentations

The following list of the publications and presentations have been directly generated based on the work described in this thesis:

Papers in Peer-reviewed Journals

1. Tian, F.-B., Luo, H., **Song, J.**, Lu, X.-Y. Force production and asymmetric deformation of a flexible flapping wing in forward flight. *Journal of Fluids and Structures*, vol. 36, 149-161, 2013.

2. **Song, J.**, Luo, H., Hedrick, T.L. Three-dimensional flow and lift characteristics of a hovering hummingbird. *Journal of the Royal Society Interface*, vol. 11 no. 98, 2014.

3. **Song, J.**, Luo, H., Hedrick, T.L. Wing-pitching mechanism of hovering Ruby-throated Hummingbirds. *Bioinspiration & Biomimetics*, vol. 10, 016007, 2015. (a featured article)

4. **Song, J.**, Luo, H., Hedrick, T.L. Performance of a quasi-steady model for hovering hummingbirds. *Theoretical & Applied Mechanics Letters*, vol.5, 2015.

5. **Song, J.**, Luo, H., Tobalske, B.W. Hedrick, T.L. Computational modeling of aerodynamics in the fast forward flight of *calliope* hummingbird. *In preparation*

Papers in Peer-reviewed Conference Proceedings

1. Luo, H., Dai, H., Adam Das S.S.M., **Song, J.**, Doyle J.F., Toward high-fidelity modeling of the fluid- structure interaction for insect wings, Proceedings of 50th AIAA Aerospace Sciences Conference, Nashville, TN, Jan. 09-12, 2011.

2. **Song, J.**, Luo, H., Hedrick, T.L. Flow characteristics of a hovering hummingbird, Proceedings of 43rd AIAA Fluid Dynamics Conference, San Diego, CA, Jun. 24-27, 2013.

3. **Song, J.**, Luo, H., Hedrick, T.L. Aerodynamic Performance of Rufous Hummingbird During Hovering Flight, Proceedings of ASME District F Early Career Technical Conference, Birmingham, AL, Nov. 2-3, 2013.

4. **Song, J.**, Luo, H., Hedrick, T.L. Comparison of CFD and quasi-steady analysis of hovering aerodynamics for a Ruby-throated hummingbird, Proceedings of 44th AIAA Fluid Dynamics Conference, Atlanta, GA, Jun. 16-20, 2014.

5. **Song, J.**, Luo, H., Tobalske, B.W., Hedrick, T.L. Analysis of cruise flight of the calliope hummingbird hummingbird, Proceedings of 45th AIAA Fluid Dynamics Conference, Dallas, TX, Jun. 22-26, 2015.

Presentations and Posters

1. **Song, J.**, Luo, H., Hedrick, T.L. Aerodynamics of Hummingbird hovering flight. American Physical Society 65th Annual DFD Meeting, San Diego, CA, Nov. 18-20, 2012.

2. **Song, J.** Unsteady aerodynamics of hummingbird at hovering flight, Vanderbilt University Department of Mechanical Engineering seminar, Apr. 20th, 2013.

3. **Song, J.**, Luo, H., Hedrick, T.L. Aerodynamic Performance of Rufous Hummingbird During Hovering Flight, ASME District F Early Career Technical Conference paper, Birmingham, AL, Nov. 2-3, 2013.

4. **Song, J.**, Luo, H., Hedrick, T.L. Comparison of CFD and quasi-steady analysis of hovering aerodynamics for a Ruby-throated hummingbird, 44th AIAA Fluid Dynamics Conference paper, Atlanta, GA, Jun. 16-20, 2014.

5. **Song, J.**, Luo, H., Tobalske, B.W., Hedrick, T.L. Computationial modeling of aerodynamics in humminbird flight, Multiscale modelling and simulation center (MuMS) seminar, Jun. 18, 2015.

6. **Song, J.**, Luo, H., Tobalske, B.W., Hedrick, T.L. Analysis of cruise flight of the calliope hummingbird, 45th AIAA Fluid Dynamics Conference, Dallas, TX, Jun. 22-26, 2015.

7. **Song, J.**, Luo, H., Tobalske, B.W., Hedrick, T.L. Computational modeling of *calliope* hummingbird flying at $8m/s$ forward speed, APS Canadian-American-Mexican Graduate Student Physics Conference , Oaxaca, Mexico, Sep. 09-12, 2015 (Supported by an APS Competitive Travel Award).

8. **Song, J.**, Luo, H., Tobalske, B.W., Hedrick, T.L. Computational modeling of aerodynamics in the fast forward flight of hummingbird, The 68th Annual Meeting of APS/DFD, Boston, MA, Nov. 22-24, 2015.

REFERENCES

D.E. Alexander. *Nature's flyers: birds, insects, and the biomechanics of flight*. JHU Press, 2004.

D.L. Altshuler, R. Dudley, and C.P. Ellington. Aerodynamic forces of revolving hummingbird wings and wing models. *J. Zool., Lond.*, 264:327–332, 2004a.

D.L. Altshuler, R. Dudley, and J.A. McGuire. Resolution of a paradox: Hummingbird flight at high elevation does not come without a cost. *PNAS*, 101:17731–17736, 2004b.

D.L. Altshuler, M. Princevac, H. Pan, and J. Lozano. Wake patterns of the wings and tail of hovering hummingbirds. *Exp. Fluids*, 46:835–846, 2009.

H. Aono, F. Liang, and H. Liu. Near- and far-field aerodynamics in insect hovering flight: an intergrated computational study. *Journal of Experimental Biology*, 211: 239–257, 2008. doi:10.1242/jeb.008649.

A.J. Bergou, S. Xu, and Z.J. Wang. Passive wing pitch reversal in insect flight. *Journal of Fluid Mechanics*, 591:321–337, 2007.

J.M. Birch and M.H Dickinson. Spanwise flow and the attachment of leading-edge vortex on insect wings. *Nature*, 412:729–733, 2001.

P. Chai and R. Dudley. Limits to flight energetics of hummingbirds hovering in hypodense and hypoxic gas mixtures. *Journal of Experimental Biology*, 199(10):2285–2295, 1996.

P. Chai and R. Dudley. Maximum flight performance of hummingbirds: Capacities, constraints, and trade-offs. *The American Naturalist*, 153(4):398–411, 1999.

M.A.C. Chance. Air flow and the flight of a noctuid moth. In *Swimming and flying in nature*, pages 829–843. Springer, 1975.

A. J. Chorin. Numerical solution of the navier–stokes equations. *Mathematics of Computation*, 22(104):745, 1968.

M.J. Csicsáky. Body-gliding in zebra finch. *Fortschritte der Zoologie*, 24(2-3):275–286, 1977.

H. Dai, H. Luo, and J. F. Doyle. Dynamic pitching of an elastic rectangular wing in hovering motion. *Journal of Fluid Mechanics*, 693:473–499, 2012a.

H. Dai, H. Luo, and J. F. Doyle. Dynamic pitching of an elastic rectangular wing in hovering motion. *Journal of Fluid Mechanics*, 693:473–499, 2012b.

M.H. Dickinson, F. Lehmann, and S.P. Sane. Wing rotation and the aerodynamic basis of insect flight. *Science*, 284:1954–1960, 1999.

R. Dudley. *The biomechanics of insect flight: form, function, evolution*. Princeton University Press, 2002.

R. Dudley and C.P. Ellington. Mechanics of forward flight in bumblebee: I. kinematics and morphology. *Journal of Experimental Biology*, 148(1):19–52, 1990a.

R. Dudley and C.P. Ellington. Mechanics of forward flight in bumblebees: Ii. quasi-steady lift and power requirements. *Journal of Experimental Biology*, 148(1):53–88, 1990b.

Y. Elimelech and C.P. Ellington. Analysis of the transitional flow field over a fixed hummingbird wing. *Journal of Experimental Biology*, 216(2):303–318, 2013.

C.P. Ellington. The aerodynamics of hovering insect flight. i. the quasi-steady analysis. *Philosophical Transactions of the Royal Society of London. B, Biological Sciences*, 305(1122):1–15, 1984.

C.P. Ellington. Power and efficiency of insect flight muscle. *Journal of Experimental Biology*, 115(1):293–304, 1985.

C.P. Ellington, C. van den Berg, A.P. Willmott, and A.L.R. Thomas. Leading-edge vortices in insect flight. *Nature*, 384:626–630, 1996.

A.R. Ennos. The inertial cause of wing rotation in diptera. *Journal of Experimental Biology*, 140:161–169, 1988a.

A.R. Ennos. The inertial cause of wing rotation in diptera. *Journal of Experimental Biology*, 140(1):161–169, 1988b.

A.R. Ennos. Inertial and aerodynamic torques on the wings of diptera in flight. *Journal of Experimental Biology*, 142(1):87–95, 1989a.

A.R. Ennos. The kinematics an daerodynamics of the free flight of some diptera. *Journal of Experimental Biology*, 142(1):49–85, 1989b.

H. Försching and H. Hennings. Aeroelastic mysteries in avian flight. *CEAS Aeronautical Journal*, 3(2-4):135–143, 2012.

S.N. Fry, R. Sayaman, and M.H. Dickinson. The aerodynamics of free-flight maneuvers in drosophila. *Science*, 300(5618):495–498, 2003.

R.R. Harbig, J. Seridan, and M.C. Thompson. Reynolds number and aspect ratio effects on the leading-edge vortex for rotating insect wing planforms. *Journal of Fluid Mechanics*, 717:166–192, 2013.

A. Hedenström and L.C. Johansson. Bat flight: aerodynamics, kinematics and flight morphology. *Journal of Experimental Biology*, 218(5):653–663, 2015.

T.L. Hedrick. Software techniques for two-and three-dimensional kinematic measurements of biological and biomimetic systems. *Bioinspiration & Biomimetics*, 3(3): 034001, 2008.

T.L. Hedrick, J.R. Usherwood, and A.A. Biewener. Wing inertia and whole-body acceleration: an analysis of instantaneous aerodynamic force production in cockatiels (nymphicus hollandicus) flying across a range of speeds. *Journal of Experimental Biology*, 207(10):1689–1702, 2004.

T.L. Hedrick, B. Cheng, and X. Deng. Wingbeat time and the scaling of passive rotational damping in flapping flight. *Science*, 324(5924):252–255, 2009.

T.L. Hedrick, B.W. Tobalske, I.G. Ros, D.R. Warrick, and A.A. Biewener. Morphological and kinematic basis of the hummingbird flight stroke: scaling of flight muscle transmission ratio. *Proc. R. Soc. B*, 279:1986–1992, 2012.

P. Henningsson, G.R. Spedding, and A. Hedenström. Vortex wake and flight kinematics of a swift in cruising flight in a wind tunnel. *Journal of Experimental Biology*, 211 (5):717–730, 2008.

T. Jardin, A. Farcy, and L David. Three-dimensional effect in hoving flapping flight. *Journal of Fluid Mechanics*, 702:102–125, 2012. doi:10.1017/jfm.2012.163.

A.A. Karhu. A new genus and species of the family Jungornithidae (Apodiformes) from the Late Eocene of the Northern Caucasus, with comments on the ancestry of hummingbirds. *Smithsonian Contributions to Paleobiology*, (89), 1999.

M.T. Keennon, K.R. Klingebiel, A. Andryukov, D. Hibbs, and J.P. Zwaan. Air vehicle flight mechanism and control method, December 9 2010. URL `https://www.google.com/patents/CA2776485A1?cl=en`. CA Patent App. CA 2,776,485.

E.J. Kim, M. Wolf, V.M. Ortega-Jimenez, S.H. Cheng, and R. Dudley. Hovering performance of anna's hummingbirds (calypte anna) in ground effect. *Journal of The Royal Society Interface*, 11(98):20140505, 2014.

J.W. Kruyt, E.M. Quicazán-Rubio, G.F. van Heijst, D.L. Altshuler, and D. Lentink. Hummingbird wing efficacy depends on aspect ratio and compares with helicopter rotors. *Journal of The Royal Society Interface*, 11(99):20140585, 2014.

F. Lehmann, S.P. Sane, and M. Dickinson. The aerodynamic effects of wing–wing interaction in flapping insect wings. *Journal of Experimental Biology*, 208(16):3075–3092, 2005.

D. Lentink and M.H. Dickinson. Rotational accelerations stabilize leading edge vortices on revolving fly wings. *Journal of Experimental Biology*, 212:2705–2719, 2009. doi:10.1242/jeb.022269.

H. Liu and K. Kawachi. A numerical study of insect flight. *J. Comput. Phys.*, 146(1): 124–156, 1998.

H. Luo, H. Dai, P. Ferreira de Sousa, and B. Yin. On numerical oscillation of the direct-forcing immersed-boundary method for moving boundaries. *Comput. & Fluids*, 56: 61–76, 2012.

R. Mittal and S. Balachandar. Generation of streamwise vortical structures in bluff body wakes. *Physical review letters*, 75:1300–1303, 1995a.

R. Mittal and S. Balachandar. Generation of streamwise vortical structures in bluff body wakes. *Physical review letters*, 75(7):1300, 1995b.

R. Mittal, H. Dong, M. Bozkurttas, F. M. Najjar, A. Vargas, and A. vonLoebbeck. A versatile sharp interface immersed boundary method for incompressible flows with complex boundaries. *J. Comput. Phys.*, 227(10), 2008. 4825-4852.

W. Nachtigall. Zur aerodynamik des coleopteren-fluges: wirken die elytren als tragflächen. *Verhandlungen der Deutschen Zoologischen Gesellschaft*, 27:319–326, 1964.

R. Norberg. The pterostigma of insect wings an inertial regulator of wing pitch. *J. Comp. Physiol.*, 81(1):9–22, 1972.

U.M. Norberg. Aerodynamics, kinematics, and energetics of horizontal flapping flight in the long-eared bat plecotus auritus. *Journal of Experimental Biology*, 65(1):179–212, 1976.

M.F.M. Osborne. Aerodynamics of flapping flight with application to insects. *Journal of Experimental Biology*, 28:221–245, 1951.

K.J. Park, M. Rosén, and A. Hedenström. Flight kinematics of the barn swallow (hirundo rustica) over a wide range of speeds in a wind tunnel. *Journal of Experimental Biology*, 204(15):2741–2750, 2001.

C.J. Pennycuick. Power requirements for horizontal flight in the pigeon columba livia. *Journal of Experimental Biology*, 49(3):527–555, 1968.

C.J. Pennycuick. On the reconstruction of pterosaurs and their manner of flight, with notes on vortex wakes. *Biological Reviews*, 63(2):299–331, 1988.

C.J. Pennycuick. Predicting wingbeat frequency and wavelength of birds. *Journal of Experimental Biology*, 150(1):171–185, 1990.

L. Ristroph, A.J. Bergou, J. Guckenheimer, Z. J. Wang, and I. Cohen. Paddling mode of forward flight in insects. *Physical review letters*, 106(17):178103, 2011.

M. Rosén, G.R. Spedding, and A. Hedenström. Wake structure and wingbeat kinematics of a house-martin delichon urbica. *Journal of The Royal Society Interface*, 4(15): 659–668, 2007.

M.H. Sane, S.P. Dickinson. The control of flight force by a flapping wing:lift and drag production. *Journal of Experimental Biology*, 204:2607–2626, 2001.

S.P. Sane. The aerodynamics of insect flight. *Journal of Experimental Biology*, 206: 4191–4208, 2003.

S.P. Sane and M.H. Dickinson. The aerodynamic effects of wing rotation and a revised quasi-steady model of flapping flight. *Journal of Experimental Biology*, 205 (8):1087–1096, 2002.

W. Shyy, H. Aono, S.K. Chimakurthi, P. Trizila, C.K. Kang, C.E.S. Cesnik, and H. Liu. Recent progress in flapping wing aerodynamics and aeroelasticity. *Progress in Aerospace Sciences*, 46:284–327, 2010.

J. Song, H. Luo, and T.L. Hedrick. Three-dimensional flow and lift characteristics of a hovering ruby-throated hummingbird. *Journal of The Royal Society Interface*, 11 (98):20140541, 2014.

G.R. Spedding. The wake of a jackdaw (corvus monedula) in slow flight. *Journal of Experimental Biology*, 125(1):287–307, 1986.

G.R. Spedding. The wake of a kestrel (falco tinnunculus) in flapping flight. *Journal of Experimental Biology*, 127(1):59–78, 1987.

G.R. Spedding and T. Maxworthy. The generation of circulation and lift in a rigid two-dimensional fling. *Journal of Fluid Mechanics*, 165:247–272, 1986.

G.R. Spedding, J.M.V. Rayner, and C.J. Pennycuick. Momentum and energy in the wake of a pigeon (columba livia) in slow flight. *Journal of Experimental Biology*, 111(1):81–102, 1984.

G.R. Spedding, M. Rosén, and A. Hedenström. A family of vortex wakes generated by a thrush nightingale in free flight in a wind tunnel over its entire natural range of flight speeds. *Journal of Experimental Biology*, 206(14):2313–2344, 2003.

M. Stolpe and K. Zimmer. Der Schwirrflug des Kolibri im Zeitlupenfilm. *Journal of Ornithology*, 87(1):136–155, 1939.

M. Sun and H. Tang. Unsteady aerodynamic force generation by a model fruit fly wing in flapping motion. *Journal of Experimental Biology*, 205:55–70, 2002a.

M. Sun and J. Tang. Unsteady aerodynamic force generation by a model fruit fly wing in flapping motion. *Journal of Experimental Biology*, 205(1):55–70, 2002b.

M. Sun and J.H. Wu. Aerodynamic force generation and power requirements in forward flight in a fruit fly with modeled wing motion. *Journal of Experimental Biology*, 206 (17):3065–3083, 2003.

B.W. Tobalske and K.P. Dial. Flight kinematics of black-billed magpies and pigeons over a wide range of speeds. *Journal of Experimental Biology*, 199(2):263–280, 1996.

B.W. Tobalske, W.L. Peacock, and K.P. Dial. Kinematics of flap-bounding flight in the zebra finch over a wide range of speeds. *Journal of Experimental Biology*, 202(13): 1725–1739, 1999.

B.W. Tobalske, T.L. Hedrick, and A.A. Biewener. Wing kinematics of avian flight across speeds. *Journal of Avian Biology*, 34(2):177–184, 2003a.

B.W. Tobalske, T.L. Hedrick, K.P. Dial, and A.A. Biewener. Comparative power curves in bird flight. *Nature*, 421(6921):363–366, 2003b.

B.W. Tobalske, L.A. Puccinelli, and D.C. Sheridan. Contractile activity of the pectoralis in the zebra finch according to mode and velocity of flap-bounding flight. *Journal of Experimental Biology*, 208(15):2895–2901, 2005.

B.W. Tobalske, D.R. Warrick, C.J. Clark, D.R. Powers, T.L. Hedrick, G.A. Hyder, and A.A. Biewener. Three-dimensional kinematics of hummingbird flight. *Journal of Experimental Biology*, 210:2368–2382, 2007.

B.W. Tobalske, J.W. Hearn, and D.R. Warrick. Aerodynamics of intermittent bounds in flying birds. In *Animal Locomotion*, pages 401–411. Springer, 2010.

S. Vogel. Flight in drosophila i. flight performance of tethered flies. *Journal of Experimental Biology*, 44(3):567–578, 1966.

Z.J. Wang, J.M. Birch, and M.H. Dickinson. Unsteady forces and flows in low reynolds number hovering flight:two-demensional computations vs robotic wing experiments. *Journal of Experimental Biology*, 207:449–460, 2004a. doi:10.1242/jeb.00739.

Z.J. Wang, J.M. Birch, and M.H. Dickinson. Unsteady forces and flows in low reynolds number hovering flight: two-dimensional computations vs robotic wing experiments. *Journal of Experimental Biology*, 207(3):449–460, 2004b.

D.R. Warrick, B.W. Tobalske, and D.R. Powers. Aerodynamics of the hovering hummingbird. *Nature*, 435:1094–1097, 2005.

D.R. Warrick, B.W. Tobalske, and D.R. Powers. Lift production in the hovering hummingbird. *Proc. R. Soc. B*, 276:3747–3752, 2009.

T. Weis-Fogh. Quick estimates of flight fitness in hovering animals, including novel mechanisms for lift production. *Journal of Experimental Biology*, 59:169–230, 1973.

T. Weis-Fogh. Energetics of hovering flight in hummingbirds and in drosophila. *Journal of Experimental Biology*, 56(1):79–104, 1972.

T. Weis-Fogh and M. Jensen. Biology and physics of locust flight. I. basic principles in insect flight. a critical review. *Phil. Trans. R. Soc. Lond. B*, 239:415–458, 1956.

A.P. Willmott and C.P. Ellington. The mechanics of flight in the hawkmoth manduca sexta. i. kinematics of hovering and forward flight. *The Journal of Experimental Biology*, 200(21):2705–2722, 1997.

M. Wolf, V.M. Ortega-Jimenez, and R. Dudley. Structure of the vortex wake in hovering anna's hummingbirds (calypte anna). *Proc. Roy. Soc. B*, 280(1773):20132391, 2013a.

M. Wolf, V.M. Ortega-Jimenez, and R. Dudley. Structure of the vortex wake in hovering anna's hummingbirds (calypte anna). *Proc. Roy. Soc. B*, 280(1773):20132391, 2013b.

J. Wood. A study of the instantaneous air velocities in a plane behind the wings of certain diptera flying in a wind tunnel. *Journal of Experimental Biology*, 52(1):17–25, 1970.

R.J. Wootton. Support and deformability in insect wings. *Journal of Zoology*, 193(4): 447–468, 1981.

B. Yin and H. Luo. Effect of wing inertia on hovering performance of flexible flapping wings. *Physics of Fluids*, 22:111902, 2010.

J. Young, S.M. Walker, R.J. Bomphrey, G.K. Taylor, and A.L.R. Thomas. Details of insect wing design and deformation enhance aerodynamic function and flight efficiency. *Science*, 325(5947):1549–1552, 2009.

L. Zheng, T.L. Hedrick, and R. Mittal. A multi-fidelity modeling approach for evaluation and optimization of wing stroke aerodynamics in flapping flight. *Journal of Fluid Mechanics*, 721:118–154, 2013a.

L. Zheng, T.L. Hedrick, and R. Mittal. A comparative study of the hovering efficiency of flapping and revolving wings. *Bioinspiration & Biomimetics*, 8(3):036001, 2013b.